

Chair of Metal Forming

Department Product Engineering
University of Leoben, Austria



Master Thesis

MODELING AND SIMULATION OF THE ROTARY
PIERCING PROCESS

Hassan Zamani

Metallurgy

Supervisors:

Priv.-Doz. Dr. Christof Sommitsch

Dipl.-Ing. Roman Pschera

December 2008

Declaration

I declare in lieu of oath, that I wrote this thesis and performed the associated research myself, using only literature cited in this volume.

Hassan ZAMANI

Acknowledgements

It is with great pleasure that I acknowledge Priv.-Doz. Dr. Christof Sommitsch. My sincerest appreciation goes to my supervisor, Dipl.-Ing. Roman Pschera for his supervision, feedback and ideas. Particular thanks to Dipl.-Ing. Jürgen Klarner for technical support. The financial support of this study by Voestalpine Tubulars GmbH & Co KG is gratefully acknowledged.

Abstract

Finite element modeling is utilized successfully to optimize complex metal forming processes including the rotary piercing process. The rotary piercing is the first forming process for the production of seamless tubes from round billets using two rotating barrel type rolls, which are inclined to the roll axis, a plug and Diescher Discs. In this work, a three-dimensional finite element model of the piercing process in the skew rolling mill using the implicit commercial code Forge2007 was developed to predict the geometry and deformation behavior during the piercing process. Different friction models are employed to obtain correct friction conditions between the rolls and the billet. Experiments of industrial scale are used to validate the finite element model. The results showed that the model is able to predict the average outer diameter, the average inner diameter and the wall thickness very well. Furthermore, the viscoplastic friction law was more flexible to achieve accurate friction conditions between the rolls and the billet.

Kurzfassung

Finite Elemente Modellierung wird erfolgreich angewendet, um komplizierte umformtechnische Prozesse zu optimieren, wie etwa das Schrägwalzen. Das Schrägwalzen ist der erste Umformungsprozess bei der Produktion von nahtlosen Rohren unter Verwendung zwei drehender Walzen, die zur Walzenmittellinie geneigt werden, eines Dornes und von Diescherscheiben. In dieser Arbeit wurde ein dreidimensionales numerisches Modell des Schrägwalzens unter Verwendung des impliziten kommerziellen FE-Codes Forge2007 entwickelt, um die Geometrie und das Deformationsverhalten während des Schrägwalzens vorauszusagen. Verschiedene Reibungsmodelle wurden eingesetzt, um korrekte Reibungsbedingungen zwischen den Walzen und dem Billet zu beschreiben. Experimente im industriellen Maßstab wurden verwendet, um das Modell zu validieren. Die Resultate zeigten, dass das Modell in der Lage ist, den mittleren äußeren Durchmesser, den mittleren inneren Durchmesser und die Wandstärke sehr gut vorauszusagen. Außerdem erwies sich ein viskoplastische Reibungsgesetz als flexibler, um realistische Reibungsbedingungen zwischen den Walzen und dem Billet zu erzielen.

Contents

1. Introduction	3
2. Rotary Piercing.....	4
2.1 Ovality and Eccentricity	5
2.2 Force Analysis.....	7
2.2.1 Effect of the Feed Angle.....	7
2.2.2 Effect of the Gorge Distance	8
2.2.3 Effect of the Plug Advance	8
2.2.4 Effect of the Plug Diameter.....	8
2.3 Stress Analysis.....	9
2.3.1 Mannesmann Effect	11
2.3.2 Fracture Prediction	13
2.4 Velocity Analysis	16
2.5 Deformation Analysis	20
2.5.1 Strain Distribution.....	22
2.5.2 Strain Rate Distribution	23
2.5.3 Shear Deformation	26
3. Theoretical Model Background	31
3.1 Material Modeling.....	32
3.2 Boundary Conditions	33
3.3 Finite Element Formulation.....	34
4. Modeling of the Rotary Piercing Process.....	36
4.1 Previous Modeling Work	36
4.2 Experimental Procedure.....	38
4.3 FEM Model Description	44
5. Results and Discussion	53
5.1 Effect of Feed Angle on the Geometry.....	53
5.2 Effect of Plug Advance on the Geometry.....	58
5.3 Effect of Feed Angle on the Forces	63

5.4	Effect of Plug Advance on the Forces	64
5.5	Model Validation.....	65
5.5.1	Model Validation According to the Geometry.....	65
5.5.2	Model Validation According to the Twisting and the Stretching.....	69
6.	Conclusions.....	72
7.	List of Figures.....	73
8.	List of Tables.....	76
9.	References.....	77
10.	Appendix.....	79

1. Introduction

Seamless steel tubes are important products for the oil and energy industry, since they have high strength and corrosion resistance. The production of seamless tubes at the plant of the Voestalpine Tubulars GmbH & Co KG in Kindberg is performed in three forming operation: Rotary piercing, elongation and wall thickness reduction, as shown in Figure 1.1.

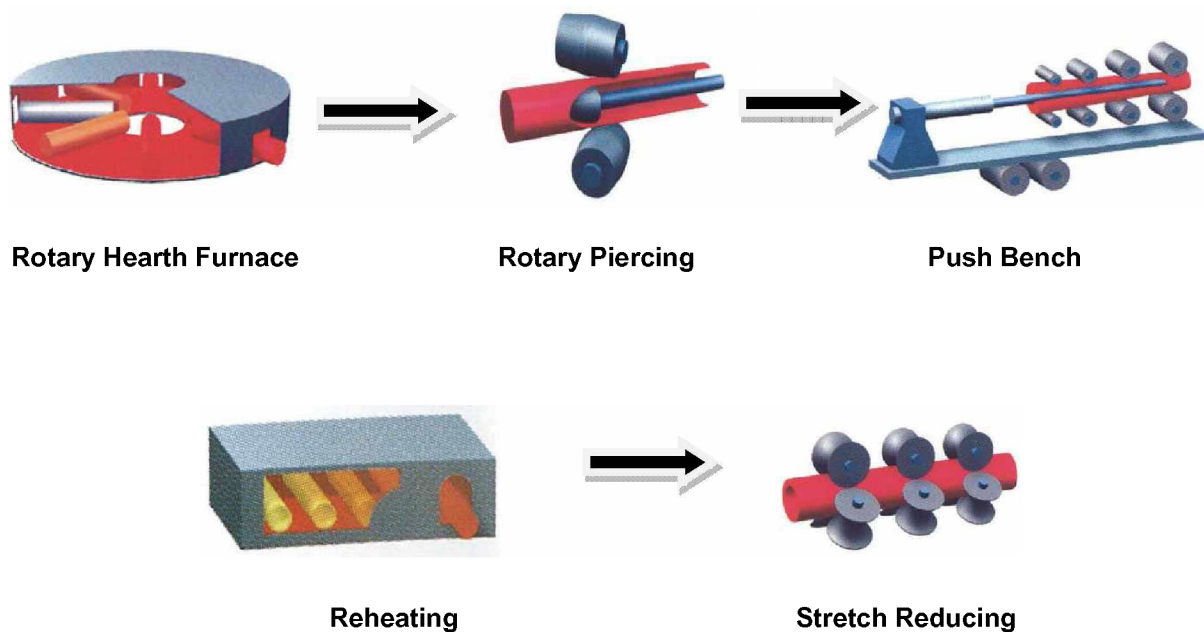


Figure 1.1: Process chain for the production of seamless tubes.

In this work, finite element simulations of the piercing process are performed to predict the geometry and deformation behavior during the rolling. The effects of different rolling conditions on the resulting geometry are studied. In order to obtain correct friction conditions between the rolls and the billet, different friction models are tested. The experimental results are compared with the FEM calculations and the validity of the model is confirmed.

2. Rotary Piercing

The rotary piercing is the first forming operation for the production of seamless tubes from round billets using rolls, a plug and Diescher discs. The heated billet is dragged by two barrel-shaped rolls that rotate in the same direction and which axes make an angle with the rolling direction, which is called feed angle. Figure 2.1 shows the Cartesian coordinate system. Due to the inclination of the axes of the rolls, the axial velocity component of the rolls is transmitted by friction to the billet, pulling the billet forward. The roll gorge is enclosed in the horizontal direction by Diescher Discs, which rotate and have a distance to each other (A). As the billet moves along the rolling direction (x-axis) it meets the plug, which is set a certain distance (LD) ahead of the gorge (the minimum distance between the rolls, E), and a central cavity may appear at the face side of the billet. Due to the cyclic stressing from tension to compression, a central cavity may be found before the billet reaches the plug (Mannesmann effect). The plug is set in front of the region to avoid the central fracture and, thus, the occurrence of inner surface defects [1, 2].

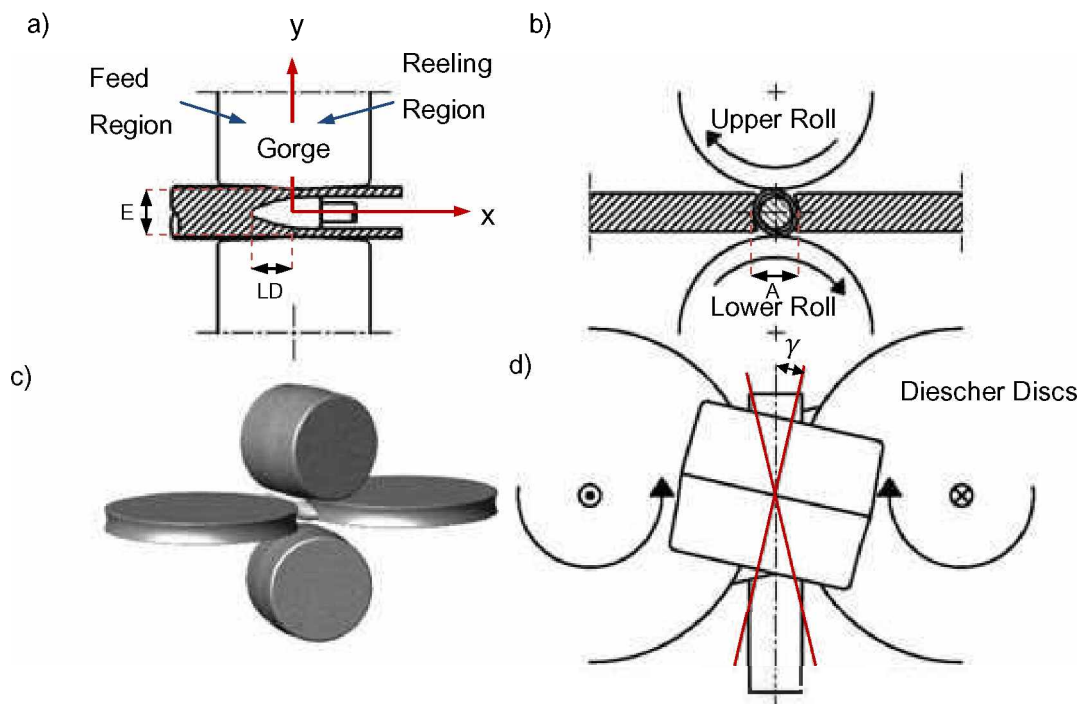


Figure 2.1: The rotary tube piercing process: (a) side view, (b) front view, (c) 3D overview, (d) plan view.

2.1 Ovality and Eccentricity

In the rotary piercing operation, the diameter of the billet is reduced and the billet's cross section is converted from a circle to an oval. The difference between the rotation velocity of the plug and the roll may be a cause of the ovality [3]. Two Diescher Discs keep the workpiece in the forming zone and influence the ovality. The ovality and the eccentricity can be defined by the following relations:

$$Eccentricity = \frac{S_{max} - S_{min}}{(S_{max} + S_{min})/2} \cdot 100 \quad (2.1)$$

$$Ovality = \frac{d_{max} - d_{min}}{(d_{max} + d_{min})/2} \cdot 100 \quad (2.2)$$

where S_{max} is the maximum wall thickness, S_{min} is the minimum wall thickness, d_{max} is the maximum outer diameter of the tube and d_{min} is the minimum outer diameter of the tube, as illustrated in Figure 2.2.

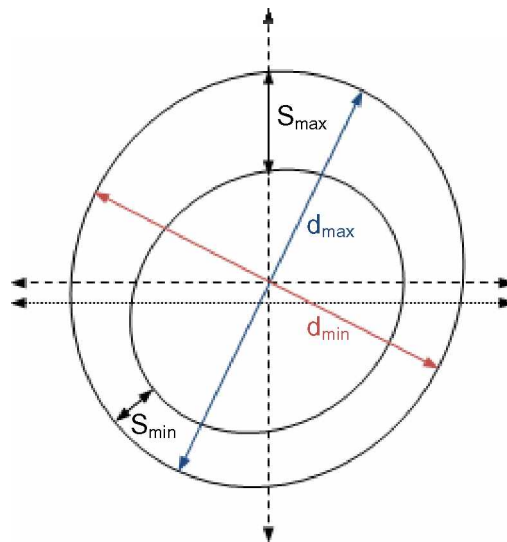


Figure 2.2: Definition of the geometry parameters associated with the ovality and eccentricity.

Circumferential wall thickness variations (eccentricity) can appear in seamless tubes by the following factors [4]:

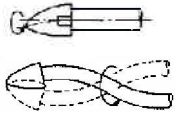
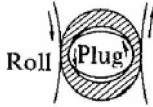
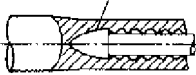
- Non-uniform heating in the billet:

The deformation resistance decreases with increasing temperature. Therefore, since the hottest point is the most likely place for the cavity localization, the temperature in the centre of the billet must be as close as possible to the hottest (weakest) point [5].

- Dimensional inaccuracy of plug and vibration of mandrel
- Shortness of reeling part of piercing plug

These causes are summarized in Table 1.

Table 1: Cause of eccentricity of tube in Mannesmann piercing [4].

No.	Causes	View
1	Non-uniform heating in a billet	
2	Deflection of piercing plug or vibration of mandrel bar	
3	Non-circularity of piercing plug	
4	Shortness of the reeling part of piercing plug	

2.2 Force Analysis

The rolls evolve compressive forces on the contact area between the rolls and the workpiece. The billet moves forward through the rolls. As a result, friction forces arise between the rolls and the billet. The friction force decomposes into a tangential component and a longitudinal component with respect to the rolling direction. The tangential component of the friction force causes the billet's rotation and the longitudinal component provides the billet progress in the rolling direction. According to Coulomb's friction law, the friction forces can be calculated by the following relation:

$$F_R = \mu P \quad (2.3)$$

where μ is the coefficient of friction and P is the compressive force acting perpendicular to the contact surface.

2.2.1 Effect of the Feed Angle

It has been observed by Dahwi and Blazynski [6] that with increasing feed angle, the roll force (F_y : force along the y -coordinate as shown in Figure 2-1a) decreases. The reason is related to the change in the position of the line of action of the radial force and an increase in the degree of the ovality. Consequently, the contact area between the plug and tube decreases.

Another study by Komori [7] showed a slight increase in the roll force in the y -direction as illustrated in Figure 2.3(a).

It is found also that as the feed angle increases, the value of the mandrel force (F_x : force along the x -coordinate system) increases too. It can be assumed that the mandrel force is identical to the x -component of the friction force between the workpiece and the tool. The x -component of the friction force increases with the feed angle as a result of the corresponding increase in the x -component of the roll velocity [6, 7].

Further, as the feed angle increases, the roll torque decreases. The reason for this is that the friction forces decrease with increasing the feed angle [6].

2.2.2 Effect of the Gorge Distance

The effect of the gorge distance on the forces is associated with the contact area between the workpiece and the roll. With increasing gorge distance, the contact area between the roll and the billet becomes smaller, as shown in Figure 2.3(b). As a result, the roll force, roll torque and plug load decrease while the mandrel force changes negligibly [6, 7].

2.2.3 Effect of the Plug Advance

The influence of the plug advance on the roll force is remarkable. The value of the roll force decreases with the plug advance (Figure 2.3(c)). As the value of the plug advance increases, the contact area between the workpiece-roll decrease, in consequence, the roll force decreases while the mandrel force becomes slightly smaller [7].

2.2.4 Effect of the Plug Diameter

The roll force and the mandrel force are affected by the plug diameter. Figure 2.3(d) shows that they both decrease at first with increasing plug diameter and then get higher values.

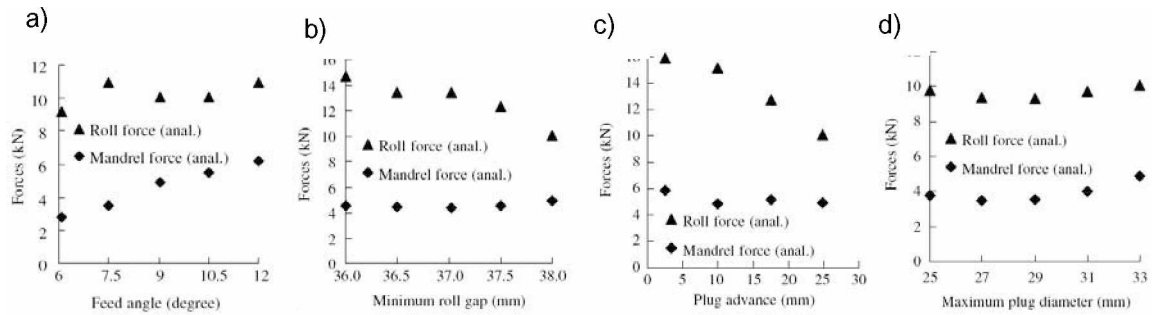


Figure 2.3: Effect of feed angle (a), minimum roll gap (b), plug advance (c) and maximum plug diameter (d) on roll force and mandrel force [7].

Effects of these variables can be summarized in the following Table 2:

Table 2: Effect of increasing feed angle, minimum roll gap, plug advance and maximum plug diameter on roll force and mandrel force.

Variable	Roll force (F_y)	Mandrel force (F_x)
Feed angle	increases slightly	increases
Minimum roll gap	decreases	negligible
Plug advance	decreases	decreases slightly
Plug diameter	increases slightly	increases slightly

2.3 Stress Analysis

The roll force causes compressive stresses in the contact point with the rolls however in the center the tensile stresses develop, which increase from zero at the surface layer to a maximum value in the centre. In addition, the tensile stresses in the centre of the billet cause slight compressive stress at the outer layer. Figure 2.4 shows the maximum principal stress. These results are based on FEM calculations, which will be explained in section 4.3.

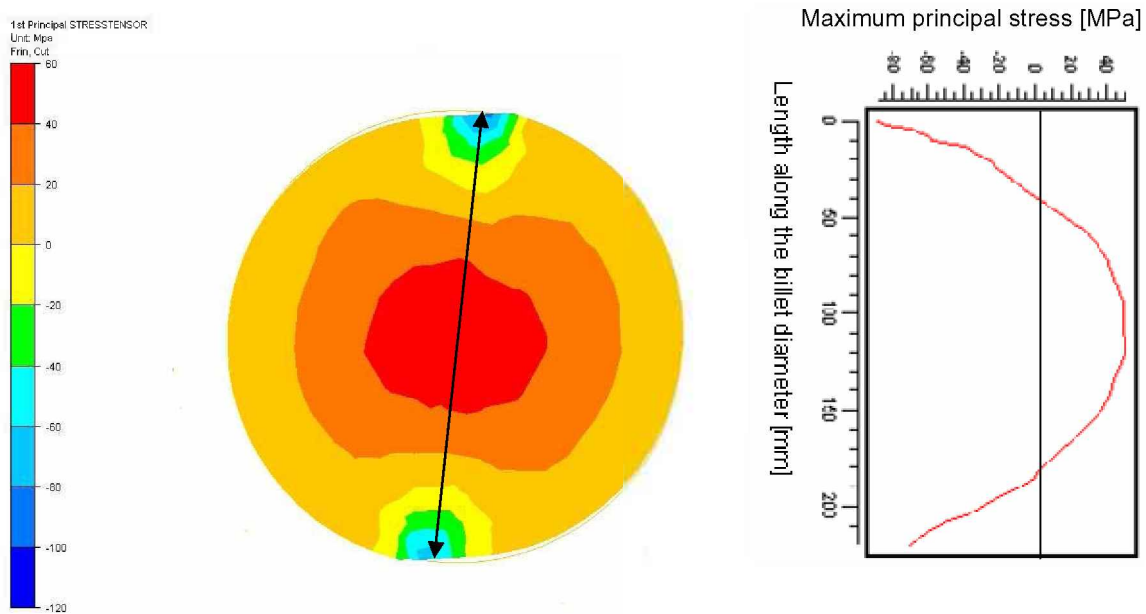


Figure 2.4: Maximum principal stress distribution in the transversal cross section of the billet at coordinate $x=-150$ mm according to the coordinate system as shown in Figure 2-1 with feed angle equal to 9° .

The maximum principal stress varies along the roll direction as illustrated in Figures 2.5a-e. It has been observed that the contact area between the rolls and the billet indicates high

compressive stresses and the magnitude of the tensile stress at the surface layer (where is not a contact) increases after a cavity formation. In the vicinity of the plug contact (in the centre of billet) a negative pressure is presented.

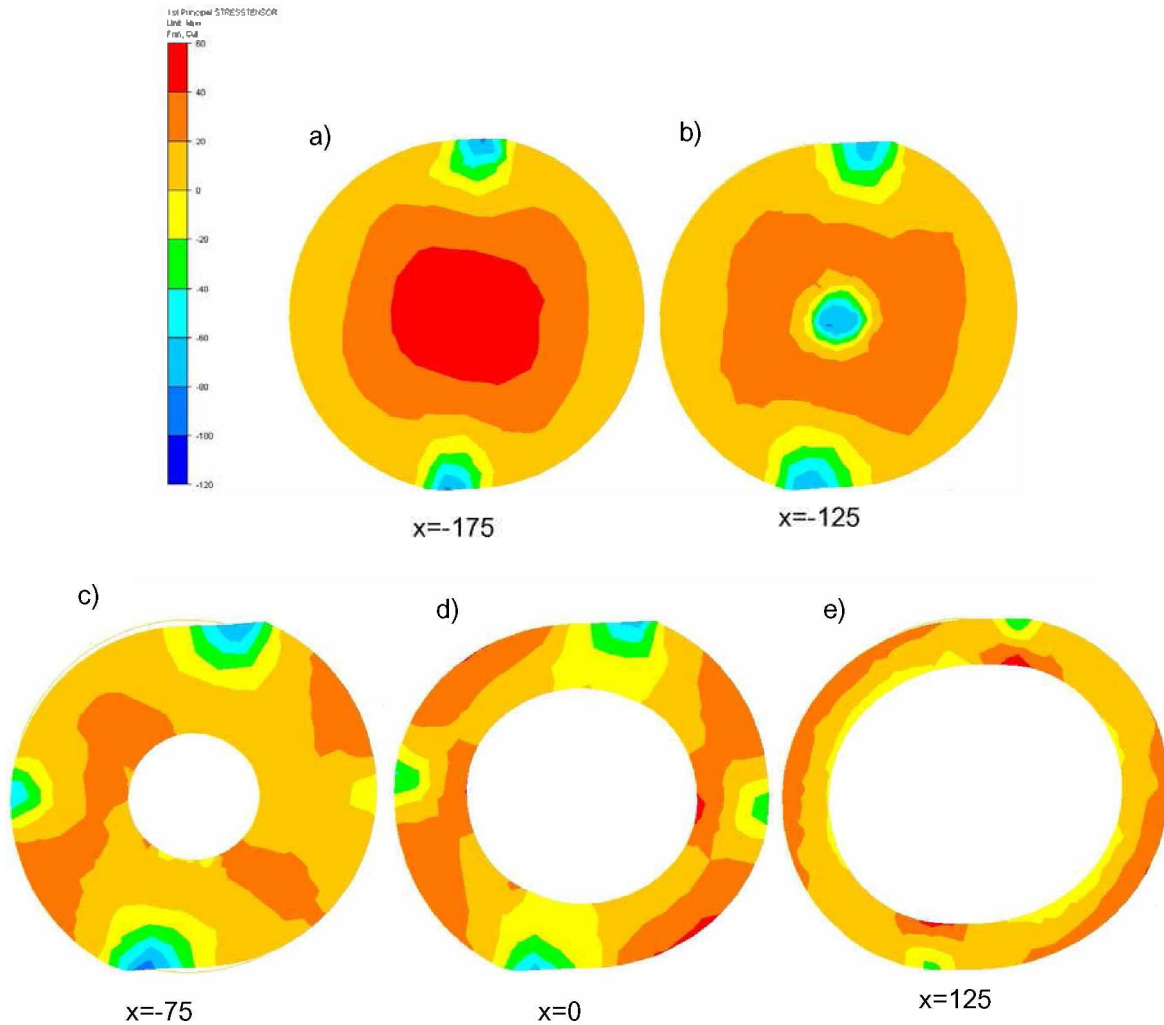


Figure 2.5: Maximum principal stress distribution in the transversal cross section of the billet according to the coordinate system as shown in Figure 2-1 with feed angle equal to 9° and plug advance equal to 125 mm.

Since the contact length between the billet and the roll decreases with increasing the feed angle, the magnitude of the compressive stresses near the outer surface becomes smaller, as shown in Figure 2.6.

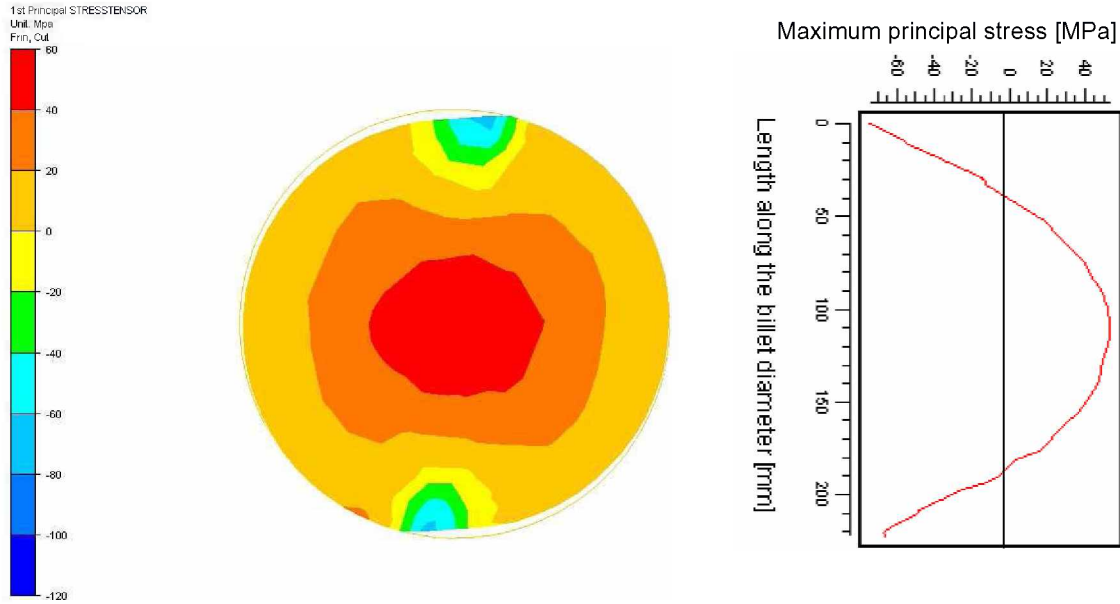


Figure 2.6: 1th principal stress distribution in the transversal cross section of the billet at coordinate $x=-150$ mm according to the coordinate system as shown in Figure 2-1 with feed angle equal to 13° .

2.3.1 Mannesmann Effect

Deformation of the surface layer of the billet occurs only below the rolls, when there is a contact between the billet and the rolls, but the central zone is always subjected to shear stresses due to rotation, which are 45° to the load connecting line, as shown in Figure 2.7. These shear stresses in combination with tensile stresses cause central fracture. This means that the fracture initiation is not created by the top of the plug but by the stresses that are induced at the centre when the billet is subjected to non-uniform radial compressive forces, which are generated by the rolls [8].

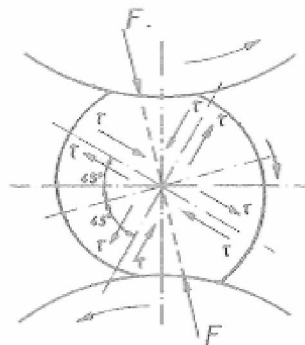


Figure 2.7: Shear stress distribution in the billet cross section [9].

Inserting the plug reduces the axial tensile stress in the centre and with increasing the degree of plug insertion stresses shift from tensile to compression range, thus, uncontrolled central cavity formation can be avoided (Figure 2.8).

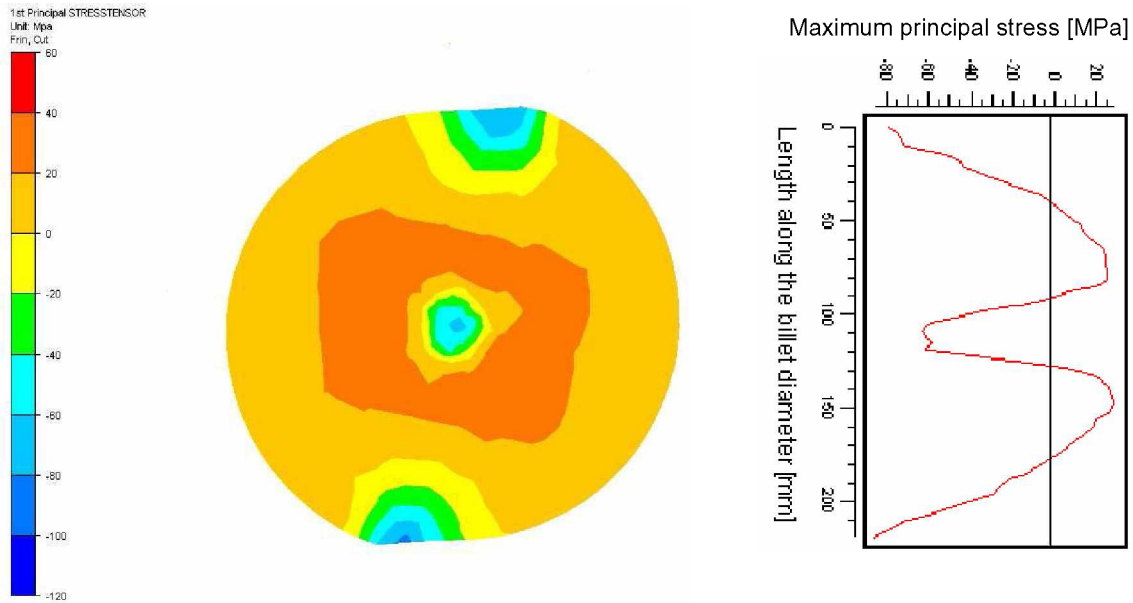


Figure 2.8: 1th principal stress distribution in the transversal cross section of the billet near to the plug position (at coordinate $x=-100$ mm according to the coordinate system as shown in Figure 2-1) with feed angle equal to 9° .

In this case the top of the plug causes fracture initiation at the centre of the billet. However, if the plug advance is too large, the plug gets destroyed due to the worse wear condition (Figure 2.9) [10].

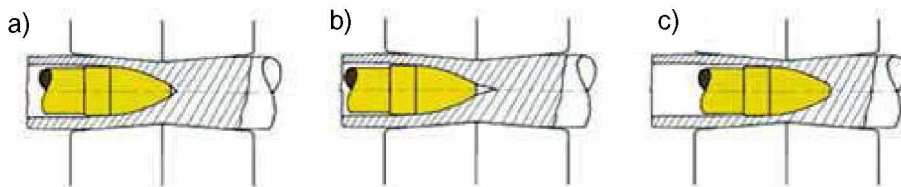


Figure 2.9: Schematic illustration of plug advance: (a) right, (b) behind, (c) ahead of the central cavity [10].

Inclusions and segregations in front of the plug are prone places for the beginning of the central cavity formation, particularly for materials with low hot workability [11].

2.3.2 Fracture Prediction

Predicting the fracture initiation can help to optimize the Mannesmann piercing process in term of plug position and other process parameters, which are mainly the forming temperature and the roll set-up. If fracture occurs earlier than the plug contact, the forces on the plug and the wear on its surface is larger and a frequent plug replacement is required. Additionally, the internal surface of the fracture tends to be more oxidized. As a result, defects arise on the interior surface of tubes [12].

In order to predict fracture initiation, several ductile crack formation criteria were proposed. These models assume that fracture occurs when weighted accumulated plastic strains reach a critical value; the larger the value of the integrate, the higher is the tendency to fracture:

$$D = \int_{\bar{\epsilon}=0}^{\bar{\epsilon}_f} f(\text{stress state}) d\bar{\epsilon} \quad (2.4)$$

where f is a weight function that depends on the local stress state in the material, $\bar{\epsilon}$ is the equivalent strain, $\bar{\epsilon}_f$ is the equivalent strain to fracture and D is the damage value [12].

D is a material constant that needs to be calibrated using experimental and numerical tests. The integral is calculated either as a post-processing step or as an uncoupled internal variable depending on the stress and strain tensors. The value D is not a universal constant of the material but is dependent on the average stress triaxiality which is the ratio of the hydrostatic stress to the von Mises equivalent stress. Table 3 shows the average stress triaxiality for upsetting test where d_0 , h_0 are the initial diameter and height of the upsetting specimen, respectively [12].

Table 3: Equivalent strain to fracture and average stress triaxiality for typical upsetting tests [12].

Specimen	Equivalent strain to fracture	Average stress triaxiality
	$(\bar{\epsilon}_f)$	$\left(\frac{\sigma_m}{\sigma}\right)$
Upsetting, $\frac{d_0}{h_0} = 0,5$	0,45	-0,273
Upsetting, $\frac{d_0}{h_0} = 1$	0,36	-0,236

The mechanism of damage can be identified by the average stress triaxiality depending on the forming process, as shown in Table 4 [12].

Table 4: Damage mechanism depending on the average stress triaxiality [12].

Average stress triaxiality	Fracture mechanism
$-1/3 < \frac{\sigma_m}{\bar{\sigma}} < 0.4$	shear fracture
$\frac{\sigma_m}{\bar{\sigma}} > 0.4$	ductile fracture due to void growth and coalescence

The Cockcroft and Latham [14] criterion assumes the maximum principal stress σ_{max} as the main factor for the fracture initiation:

$$D_c = \int_0^{\bar{\epsilon}_f} \sigma_{max} d\bar{\epsilon} \quad ; \quad \sigma_{max} > 0 \quad (2.5)$$

Oyane's criterion [14] gives a description about nucleation, growth and coalescence of cavities by the following relations:

$$D = \int_0^{\bar{\epsilon}_f} \left(1 + A \frac{\sigma_m}{\bar{\sigma}}\right) d\bar{\epsilon} \quad (2.6)$$

or,

$$D = \int_0^{\bar{\epsilon}_f} \left(A + \frac{\sigma_m}{\bar{\sigma}}\right) \dot{\epsilon} dt \geq C \quad (2.7)$$

where σ_m is the hydrostatic stress, $\bar{\sigma}$ is the von Mises equivalent stress, $\dot{\epsilon}$ is the equivalent strain rate, t is the time, $\bar{\epsilon}_f$ is the equivalent strain to fracture and C, A are material constants, where A is set equal to 3.

Li [13] presented with respect to the Oyane criterion the distribution of D -values over the cross section of the billet at the fracture initiation point. Hence, the critical value of diameter reduction is obtained. It was determined that as the feed angle increases the critical reduction gets higher [13].

In respect to the damage criterion according to Lemaitre [14], also called the principle of effective stresses, the damage value is estimated if the hydrostatic stress σ_m is positive, the equivalent stress $\bar{\sigma}$ is non-zero and the equivalent stress $\bar{\epsilon}$ is higher than a threshold value $\bar{\epsilon}_{th}$. In this criterion σ_D represents the effective stress.

$$\sigma_D = (1 - D) \sigma \quad (2.8)$$

According to the kinetic law of damage, if $(\sigma_m > 0, \bar{\sigma} \neq 0, \bar{\epsilon} > \epsilon_{th})$ then

$$\frac{\partial D}{\partial t} = \frac{D_c}{(\epsilon_f - \epsilon_{th})} R_v \bar{\epsilon} \quad (2.9)$$

with,

$$R_v = \frac{2}{3}(1 + \nu) + 3(1 - 2\nu) \frac{\sigma_m^2}{\bar{\sigma}^2} \quad (2.10)$$

Otherwise

$$\frac{\partial D}{\partial t} = 0 \quad (2.11)$$

in which D is the damage value, D_c is the damage critical value, R_v is the triaxiality function, $\bar{\epsilon}$ is the equivalent strain rate, ν is the Poisson's coefficient and ϵ_f is the strain value to fracture.

Figure 2.10 shows that a certain amount of plastic strain ε_{th} is essential to initiate damage and then damage accumulates linearly until the plastic strain of fracture ε_f is reached [15].

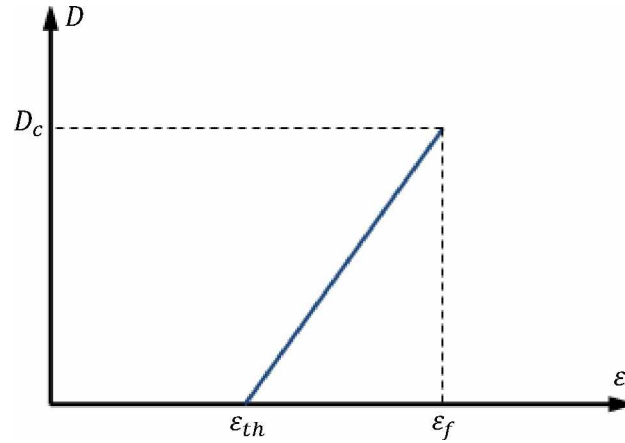


Figure 2.10: Damage evolution according to Le Maitre [15].

Concerning Lemaitre's criterion, Fanini [14] expressed that the position of the fracture initiation could be exactly predicted. However, damage obtained from the simulation is smaller than the critical value, so that Lemaitre is not able to predict the moment of cavity formation.

2.4 Velocity Analysis

The distributions of the velocity components of the billet and rolls were displayed in a cylindrical coordinate system as depicted in Figure 2.11. According to Doremus [1], the dragging velocity field is mainly rotational, the ratio between θ -velocity and the z -velocity at the billet surface being in the range of 6 to 10. The mean dragging velocity at the contact surface between the roll and the billet is expressed by the following relation:

$$v = \omega \left\{ r_m - \frac{1}{2} \left[|z| \left(\cos\alpha + \frac{1}{\cos\alpha} \right) \right] \tan\beta \right\} \quad (2.12)$$

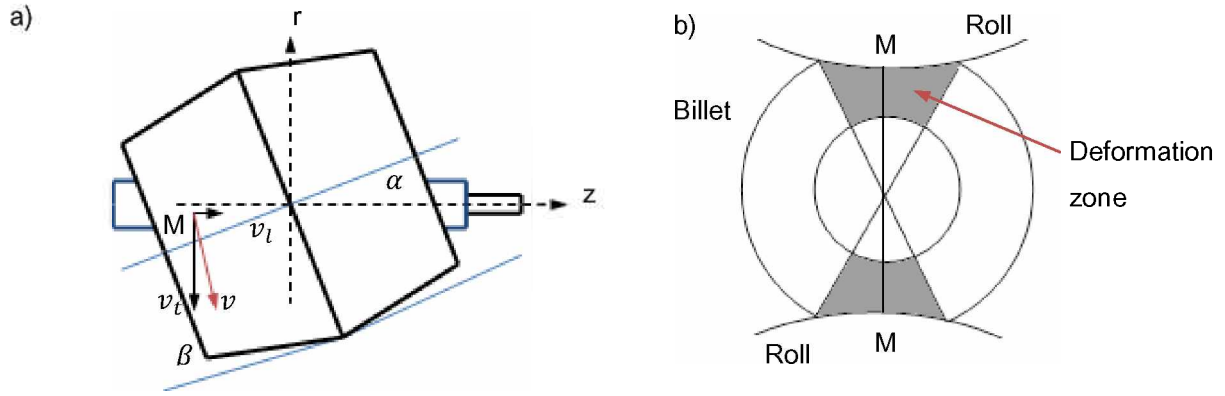


Figure 2.11: (a) Dragging velocity components at the interface between the roll and material, (b) Definition of the contact line in the transversal cross section [16].

where ω is the rotation velocity of the roll, r_m is the maximum roll radius, β the roll face angle and α the feed angle, and its axial component is given by:

$$v_l = v \sin \alpha \quad (2.13)$$

The mean axial velocity of the billet is calculated as follows:

$$v_z = v_{in} \frac{R_i^2}{r_{ou.m}^2 - r_{in}^2} \quad (2.14)$$

where v_{in} is the input velocity of the billet, R_i is the initial billet radius and $r_{ou.m}$, r_{in} are the mean outer and the inner radius of the billet/tube, respectively.

The circumferential velocity of the billet is 6 to 10 times higher than the axial velocity. The axial component of the input velocity has the following form:

$$v_{in} = \xi v \sin \alpha \frac{r_{ou.m}^2 - r_{in}^2}{R_i^2} \quad (2.15)$$

where ξ is the velocity efficiency coefficient [1].

In the piercing operation, the billet is elongated. It means that the longitudinal velocity of billet along the rolling direction is larger than the input velocity and the billet is pulled by the axial component of the roll's rotational velocity. In the barrel type rolls, the roll's rotational velocity is constant from input to output. During slow piercing, the billet is rotated more until it reaches the top of the plug and hardly moves forward. As a result, Mannesmann effect and redundant shear deformations increase and the inner defects get more [1, 11].

In the cone type rolls as shown in Figure 2.12, the rotational velocity of the roll is developed from the input to the output and rolls supply a positive pull effect, which prevents stopping the movement of the billet. It has been found that the number of billet rotations decreases by increasing the feed as well as cross angle in the cone type rolls. Hayashi [11] has defined the piercing ratio as the ratio of the tube length to the round billet length. It is confirmed that the number of billet rotations decreases more considerable with decreasing the piercing ratio.

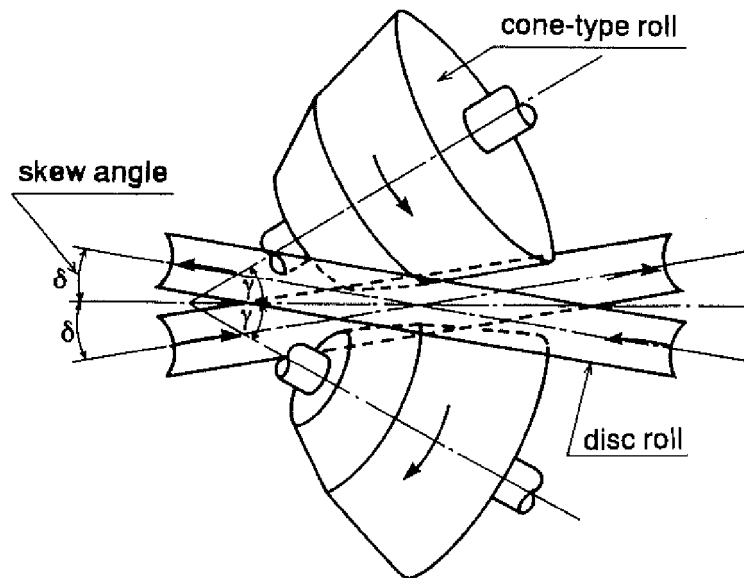


Figure 2.12: The cone-type piercing mill [17].

Figure 2.13 illustrates the effect of feed, cross angle and piercing ratio on the number of billet rotations.

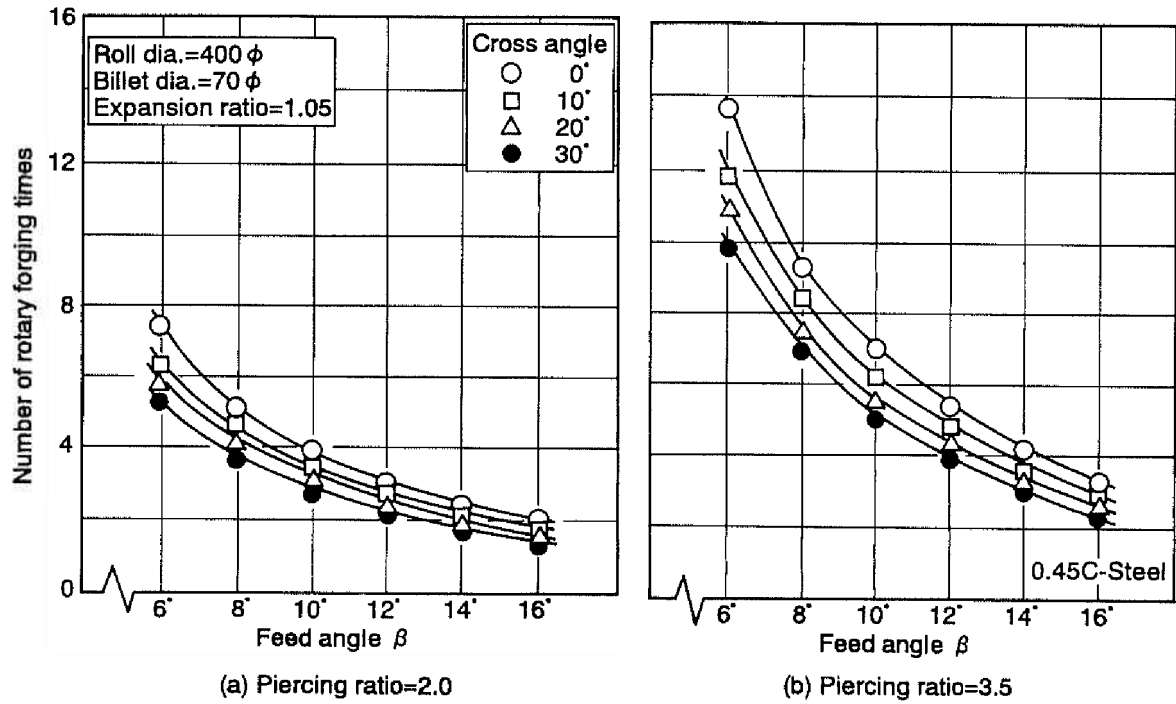


Figure 2.13: Effect of feed and cross angle and piercing ratio on the number of billet rotations [11].

The sliding velocity indicates the relationship between the components of the rotational velocity of the rolls and the pierced material. The axial sliding velocity can be expressed by the difference:

$$v_s = v_l - v_z \quad (2.16)$$

It has been observed that the sliding velocity decreases from entrance to exit, without any changes in direction.

Relation 2.17 expresses the output velocity of the seamless tube by:

$$v_o = \eta \frac{\pi r_m n_m}{60} \sin \alpha \quad (2.17)$$

where n_m is the roll speed (rpm) and η is the feed efficiency [9].

In industry, one of the most important relationships in rotary piercing is the feed efficiency which is the ratio between the tube delivery v_z (as shown in Figure 2.11a) and the axial component of the rotational velocity of the rolls v_l in each cross section of the billet. The feed efficiency can be expressed in the following way:

$$\eta = \frac{v_z}{v_l} \quad (2.18)$$

A higher feed efficiency means a higher production rate and a lower feed efficiency indicates that the billet moves less forward per billet rotation until it reaches the top of the plug.

The feed efficiency is a function of billet rotation (revolution), roll gorge, plug advance and temperature and it decreases with increasing these parameters [2].

2.5 Deformation Analysis

The main strain components during rotary piercing can be determined from the billet and tube dimensions as follows [9]:

$$\varepsilon_t = \ln \frac{2 \cdot (D_1 - S_1)}{D_0} \quad \text{or} \quad \varepsilon_t = \ln \frac{(D_1 - S_1)}{(D_0 - S_0)} \quad (2.19)$$

$$\varepsilon_r = \ln \frac{2 \cdot S_1}{D_0} \quad \text{or} \quad \varepsilon_r = \ln \frac{S_1}{S_0} \quad (2.20)$$

$$\varepsilon_l = \ln \frac{l_1}{l_0} \quad (2.21)$$

where D is the material diameter, S the wall thickness and l the length of material. Indexes indicate steps of the forming process.

Hence, the equivalent strain or homogeneous strain is expressed by:

$$\varepsilon_{eq1} = \sqrt{\frac{2}{3}(\varepsilon_t^2 + \varepsilon_r^2 + \varepsilon_l^2)} \quad (2.22)$$

In order to estimate the strain rate, Yue [18] used the simplified method by:

$$\dot{\varepsilon} = \frac{\varepsilon_{eq}}{t_c} \quad (2.23)$$

where

$$t_c = \frac{l_c}{\omega} \quad (2.24)$$

in which t_c is the contact time and l_c is the contact length along the roll direction.

To estimate the contact length, it is assumed that the face angle at the input and output is equal ($\beta_1 \approx \beta_2$), as illustrated in Figure 2.14. Therefore, the contact length along the roll direction can be calculated by the subsequent relation:

$$l_c \approx \left[\frac{R_i + R_f - G}{\tan \beta_1} \right] \cos \alpha \quad (2.25)$$

where R_i and R_f are the initial and final billet radius, respectively, G is the gorge distance, α is the feed angle and β_1 is the entry face angle.

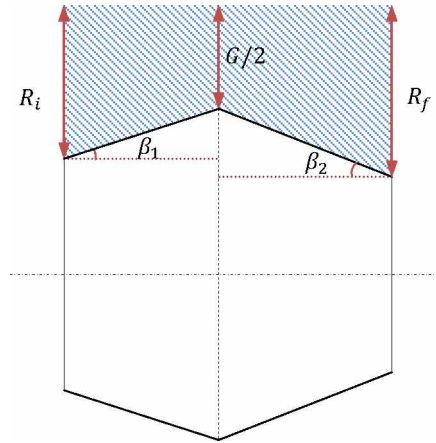


Figure 2.14: Schematic illustration of the deformation zone, which is hatched by the thin line [18].

With the aid of the above equations, the strain rate per pass is predicted by:

$$\dot{\epsilon} = \frac{\pi r_m \omega \sin \alpha}{30 l_c} \quad (2.26)$$

2.5.1 Strain Distribution

When the billet contacts the plug and the piercing operation begins, the distribution of the effective strain shows a gradient from the exterior layer to the interior side of the tube, whereas the strain at the outer surface is far larger than inside and distributes axially symmetric at the exit cross section. In addition, there is an area between these deformation zones with significantly lower strain [8]. It was found that as the feed angle increases, the equivalent strain at the cross section becomes smaller while the contact length between the billet and the roll in the rolling direction decreases. An increase in the maximum plug diameter results in extended necking in the gorge [7].

Figure 2.15 illustrates the effect of feed angle and the maximum plug diameter on the equivalent strain:

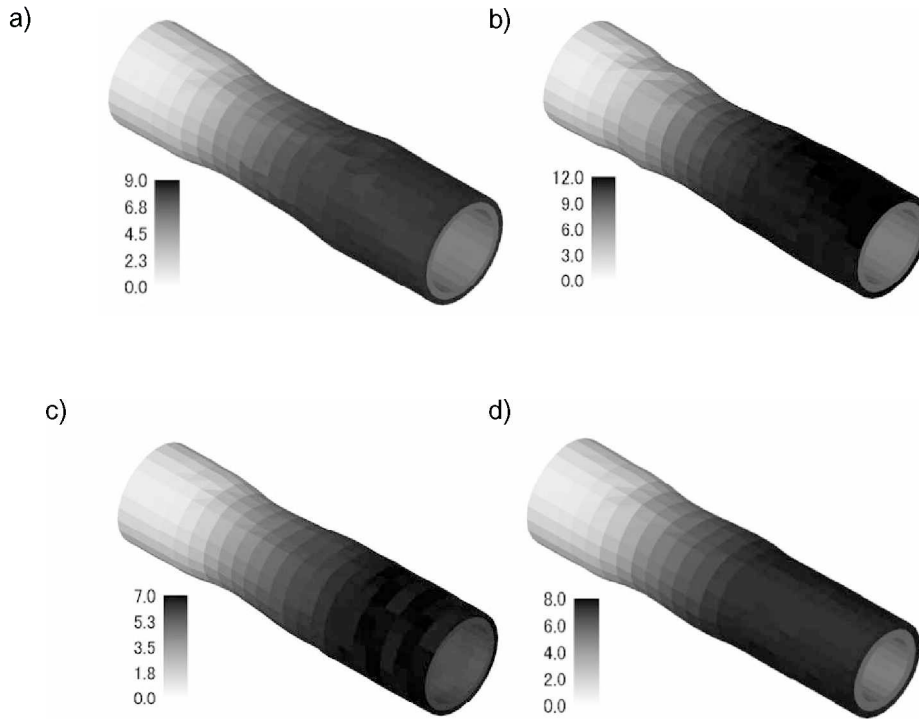


Figure 2.15: Effect of feed angle and maximum plug diameter on the equivalent strain distribution: (a) 9°, 33 mm, (b) 6°, 33 mm (c) 12°, 33 mm (d) 9°, 25 mm [7].

2.5.2 Strain Rate Distribution

Close to the central cavity, the effective strain rate indicates large values. It should be noted that the effective strain rate is high near the plug tip and then decreases slowly [1].

Another study by Komori [7] using plasticine showed that the equivalent strain rate is high in the vicinity of the roll surface and is also high at the beginning of the contact between the roll and the billet. It has been observed as well that increasing the guide shoe diameter influences the strain rate distribution slightly [7]. The contact areas between the workpiece and the tools (rolls and guide shoe) present the higher values of the strain rate [19].

Figure 2.16 shows the strain rate distribution on the exterior tube surface. It has been observed that the largest strain rates are in the contact areas between tools and billet:

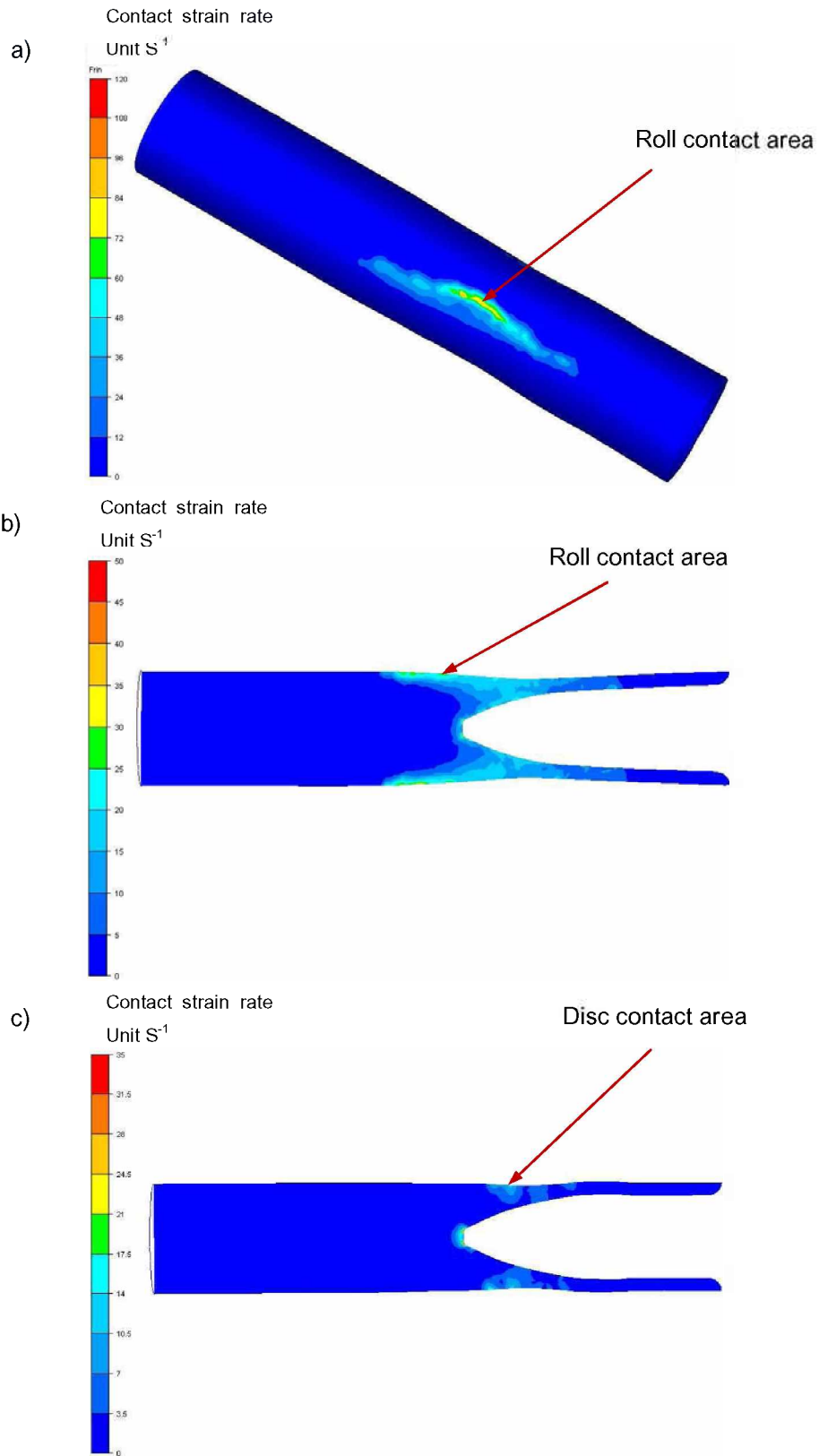


Figure 2.16: Strain rate distribution in the rotary piercing process with feed angle equal to 9° ; (a) on the exterior tube surface, (b) cut plan with normal vector $\{010\}$, (c) cut plan with normal vector $\{001\}$.

It has been found that as the feed angle increases, the strain rate near the contact areas increases. Figure 2.17 shows the strain rate distribution when the feed angle is 13° .

Nevertheless, as far as the simulation is concerned, the friction law and its coefficients have a significant influence on the equivalent strain rate in the contact area.

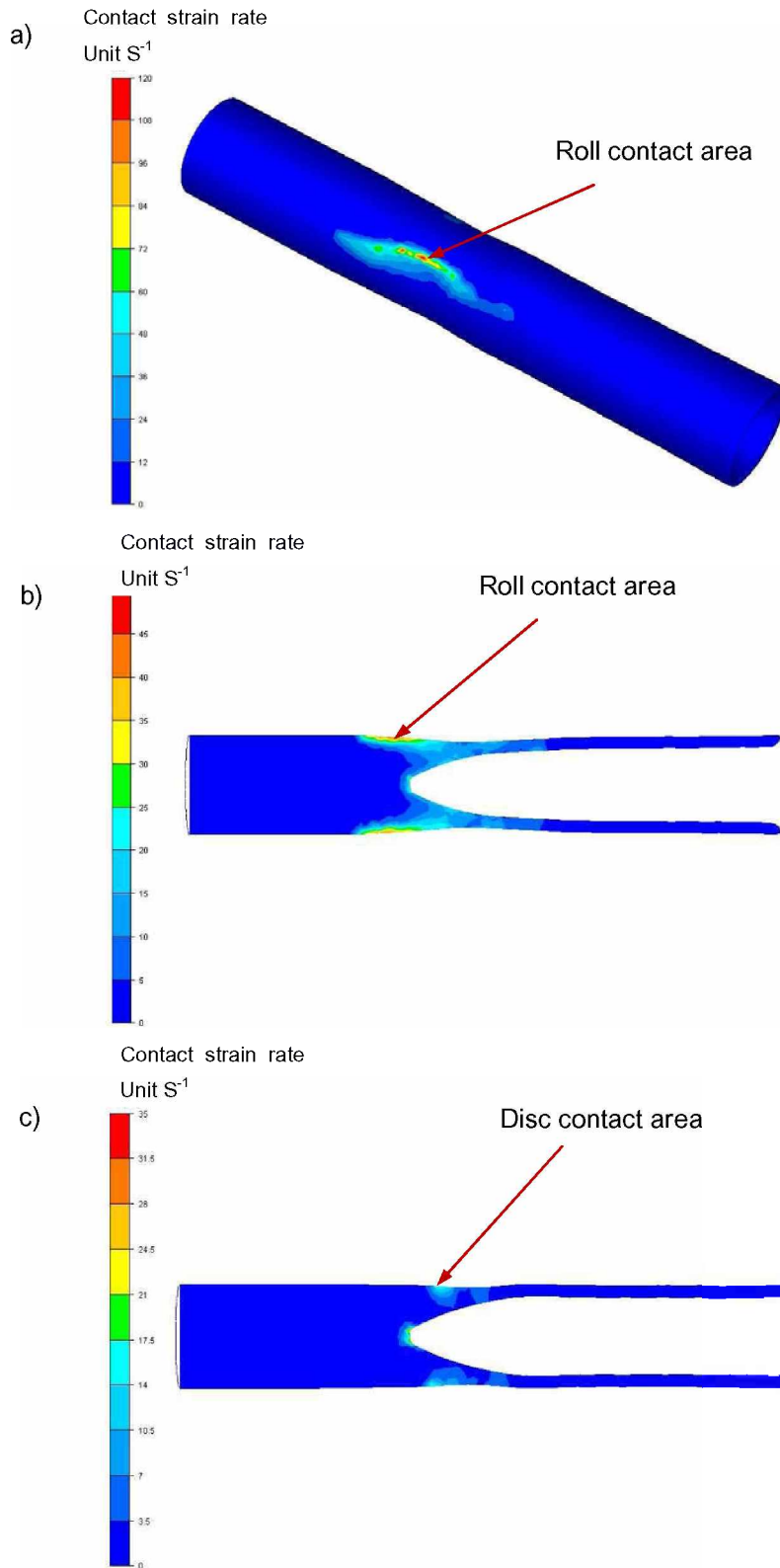


Figure 2.17: Strain rate distribution in the rotary piercing process with feed angle equal to 13°; (a) on the exterior tube surface, (b) cut plan with normal vector $\{010\}$, (c) cut plan with normal vector $\{001\}$.

2.5.3 Shear Deformation

In addition to the principal strains, it is necessary to take into account the shear deformations. These shear deformations may be a cause of the low efficiency of deformation which is in the range of approximately 10% to 16%. Shear deformations can be divided into the three following components [9]:

Circumferential shear strain $\gamma_{r\theta}$

Shear strain due to surface twist $\gamma_{\theta l}$

Longitudinal shear strain γ_{lr}

These deformations are illustrated in Figure 2.18:

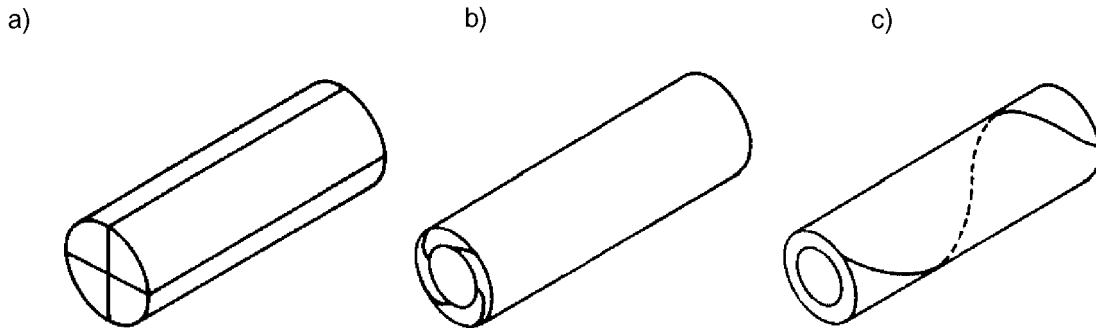


Figure 2.18: Schematic illustration of shear deformation: (a) round billet with marker, (b) circumferential shear deformation, (c) shear deformation due to surface twist [11].

The equivalent strain with respect to the shear deformation can be defined by the following relation [9]:

$$\epsilon_{eq2} = \sqrt{\frac{2}{3} \left[\epsilon_t^2 + \epsilon_r^2 + \epsilon_l^2 + 2 \left(\frac{\gamma_{r\theta}}{2} \right)^2 + 2 \left(\frac{\gamma_{\theta l}}{2} \right)^2 + 2 \left(\frac{\gamma_{lr}}{2} \right)^2 \right]} \quad (2.27)$$

The inhomogeneity of the deformation is given by:

$$\psi = \frac{\varepsilon_{eq2}}{\varepsilon_{eq1}} \quad (2.28)$$

where Ψ is called the redundancy factor. ε_{eq1} is defined in eq. (2.21).

It has been observed that roll force, plug load and roll torque become larger by increasing the total homogeneous strain as well as the redundancy factor [6].

2.5.3.1 Circumferential Shear Deformation

The circumferential shear deformation can be calculated by the following relation [11]:

$$\gamma_{r\theta} = \frac{r \cdot \theta}{t} \quad (2.29)$$

where r is the tube radius, t is the tube thickness and θ is the transport angle with respect to the circumferential shear deformation. The transport angle is shown in Figure 2.19:

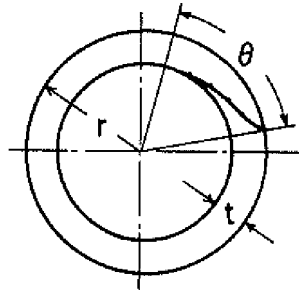


Figure 2.19: Definition of transport angle related to the circumferential shear deformation [11].

Circumferential shear deformations arise in the vicinity of the roll surface before and after the central cavity is formed. These deformations become higher when the wall thickness becomes small. Due to the fact that the rotational velocity of the plug is smaller than that of the rolls, the velocity of the interior surface is smaller than the exterior surface velocity. The difference between these velocities may be a cause of the circumferential shear deformation [3].

The influence of the rotational velocity of the plug on the circumferential shear deformation was studied by Yoshimura and Mihara [3]. The larger the plug velocity is, the smaller is the circumferential shear deformation in the vicinity of the interior surface of the tube. The direction of the circumferential shear deformation will be reversed, if the plug velocity is too large [3].

In the case of cone type rolls, Hayashi and Yamakawa [11] have investigated the influence of the feed and cross angle (as denoted with γ in Figure 2.12) on the redundant shear deformations; it was found that if the feed and cross angle increase, the circumferential shear deformation decreases significantly. When both feed and cross angle are large enough, the circumferential shear deformation can be eliminated. A decrease in the roll radius and an increase in the billet radius also decrease the circumferential shear deformation. It has been observed as well that the reduction of the circumferential shear deformation is more considerable with decreasing the piercing ratio, which is defined as the ratio of tube length to billet length.

Figure 2.20 presents the effect of the feed angle, the cross angle and the piercing ratio on the circumferential shear deformation:

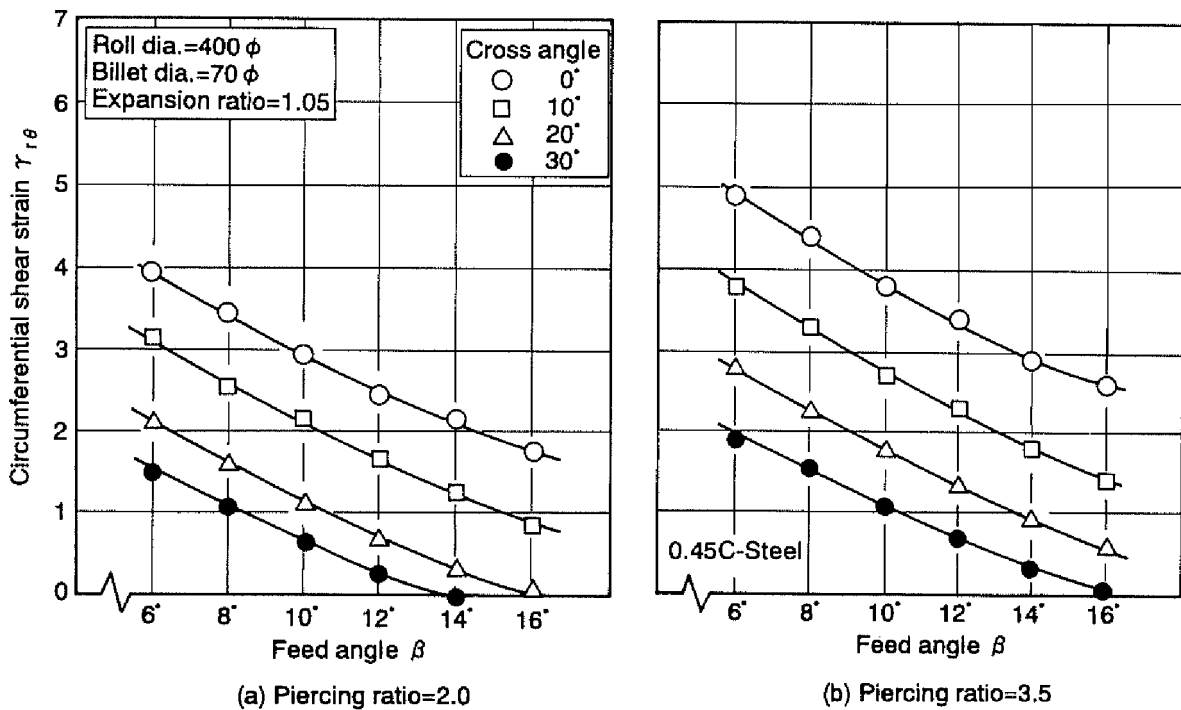


Figure 2.20: Effect of feed, cross angle and piercing ratio on the circumferential shear deformation [11].

2.5.3.2 Shear Deformation due to Surface Twist

The shear deformation due to surface twist is determined by [11]:

$$\gamma_{\theta l} = \frac{r \cdot \phi}{l} \quad (2.30)$$

where r is the tube radius, l is the length of the tube and ϕ is the transport angle with respect to the shear deformation due to surface twist. This transport angle is illustrated in Figure 2.21:

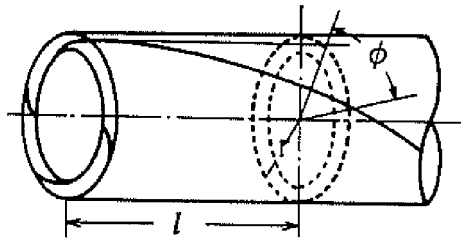


Figure 2.21: Definition of the transport angle related to the shear deformation due to surface twist [11].

The shear strain due to surface twist decreases, as the feed angle becomes larger while it increases with increasing cross angle. The reduction of the shear deformation due to surface twist is associated with increasing piercing ratio (Figure 2.22).

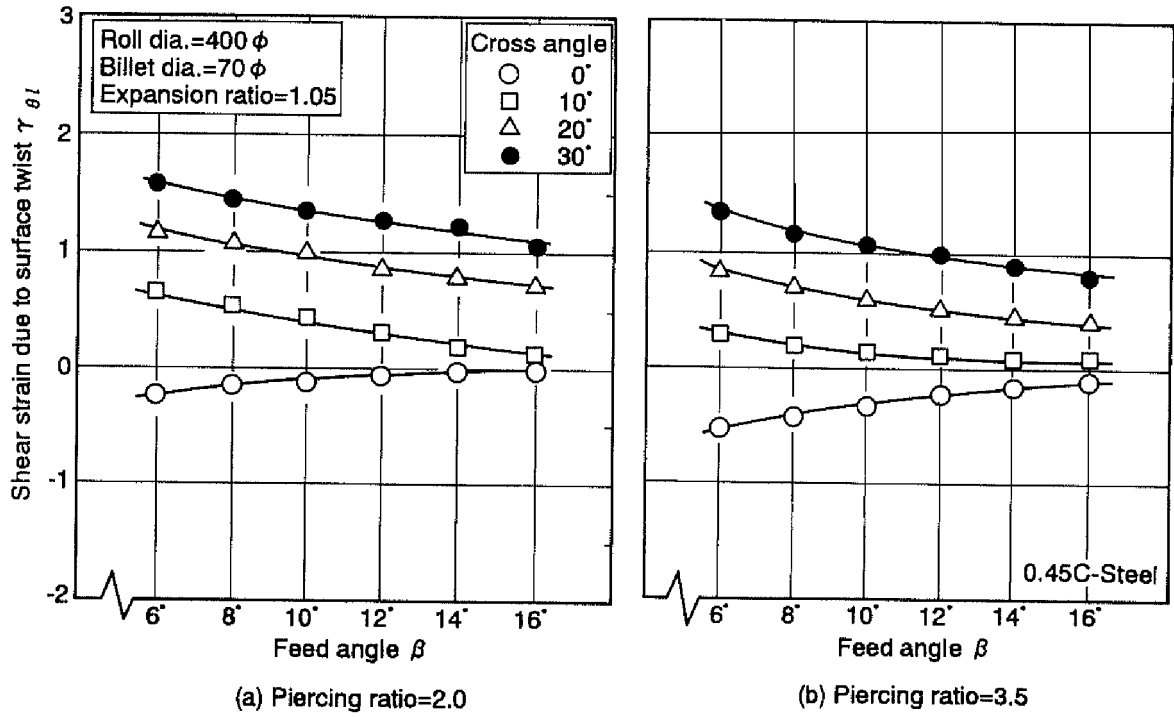


Figure 2.22: Effect of feed, cross angle and piercing ratio on the shear deformation due to surface twist [11].

In comparison with the circumferential shear deformation, shear strain due to surface twist and longitudinal shear strain can be ignored [11].

3. Theoretical Model Background

In metal forming, the workpiece is deformed applying external loads, thus, these forces are converted to deformation energy and kinetic energy. In the quasi-static problems, the acceleration vector can be assumed to be zero and gravity is negligible. Then the equation of conservation of momentum is reduced to [20]:

$$\text{div } \boldsymbol{\sigma} = 0 \quad (3.1)$$

This equation is multiplied by an arbitrary or virtual velocity field, $\mathbf{v}^*(\mathbf{x}, t)$, and is integrated over the domain Ω , where $\dot{\boldsymbol{\varepsilon}}^*$ is the virtual strain rate.

Since the stress tensor, $\boldsymbol{\sigma}$, is symmetric [20]:

$$\text{div } \boldsymbol{\sigma} \cdot \mathbf{v}^* = \text{div } (\boldsymbol{\sigma} \cdot \mathbf{v}^*) - \boldsymbol{\sigma} : \dot{\boldsymbol{\varepsilon}}^* \quad (3.2)$$

and with respect to the divergence theorem, we obtain [20]:

$$\int_{\Omega} \boldsymbol{\sigma} : \dot{\boldsymbol{\varepsilon}}^* dV - \int_{\partial\Omega} (\boldsymbol{\sigma} \cdot \mathbf{n}) \cdot \mathbf{v}^* dS = 0 \quad (3.3)$$

The stress vector (\mathbf{F}) acting on a surface inside the domain Ω or at a part of the boundary $\partial\Omega$, if \mathbf{n} is the surface normal, is defined by [20]:

$$\mathbf{F} = \boldsymbol{\sigma} \cdot \mathbf{n} \quad (3.4)$$

Hence, the equilibrium equation based on the principle of virtual power can be expressed by [20]:

$$\int_{\Omega} \boldsymbol{\sigma} : \dot{\boldsymbol{\varepsilon}}(\mathbf{v}^*) dV - \int_{\partial\Omega} \mathbf{F} \cdot \mathbf{v}^* dS = 0 \quad (3.5)$$

The above mentioned equation is the basic equation for the finite-element formulation and should be solved at each time increment. In this equation, \mathbf{F} , $\boldsymbol{\sigma}$, $\dot{\boldsymbol{\varepsilon}}$ are functions of \mathbf{v} . By discretizing the basic equation (3.5) according to the interpolation of the velocity field, it is changed into a system of equations, which refer to the nodal and velocity field number where only the nodal components of the velocity are unknown $[\mathbf{R}(\mathbf{v})]$. By derivating $[\partial\mathbf{R}/\partial\mathbf{v}]$, a set of algebraic equations (stiffness equation) can be obtained, which are non-linear equations. These equations can be solved using the Newton-Raphson method [20, 21].

3.1 Material Modeling

The Norton-Hoff viscoplastic material behavior provides a good approximation of the behavior of materials at temperatures $T > 2/3 T_{melting}$ in K [22]:

$$\mathbf{s} = 2K(\sqrt{3} \dot{\varepsilon}_{eq})^{m-1} \dot{\boldsymbol{\varepsilon}} \quad (3.6)$$

where s is the deviatoric stress, m is the strain rate sensitivity coefficient, and K is the viscoplastic consistency. These parameters express the strain hardening condition and the ductility increase due to increased temperature [22]:

$$K = K_0(\varepsilon_{eq} + \varepsilon_0)^n \exp\left(\frac{\zeta}{T}\right) \quad (3.7)$$

$$m = m_0 + m_1 T \quad (3.8)$$

where K_0 is a constant, n is the coefficient of sensitivity to the work hardening, ζ is the coefficient of sensitivity to the temperature and ε_0 is the term of regulation of work hardening. The coefficients K_0 , ε_0 , n , ζ , m_0 , m_1 can be evaluated by simple tests at different strain rates and temperatures.

3.2 Boundary Conditions

The boundary surface can be separated in three different parts [20]:

$$\partial\Omega = \partial\Omega_v + \partial\Omega_F + \partial\Omega_c \quad (3.10)$$

where $\partial\Omega_v$ is the velocity boundary condition, $\partial\Omega_F$ is the subjected part by the stress vector, and $\partial\Omega_c$ is tool-workpiece interface.

On the tool-workpiece interface two types of conditions can be observed [22]:

- Unilateral contact condition: In this case, the workpiece does not penetrate the tool (Signorini condition):

$$\left. \begin{aligned} (\mathbf{v} - \mathbf{v}_{tool}) \cdot \mathbf{n} &\leq 0 \\ \sigma_n &\leq 0 \\ [(\mathbf{v} - \mathbf{v}_{tool}) \cdot \mathbf{n}] \sigma_n &= 0 \end{aligned} \right\} \quad (3.11)$$

where v_{tool} is the tool velocity and σ_n is the contact pressure.

- Friction condition: The tangential stress vector is expressed by:

$$\mathbf{F}_\tau = \mathbf{F} - (\mathbf{F} \cdot \mathbf{n})\mathbf{n} \quad (3.12)$$

The vector \mathbf{F}_τ is orthogonal to \mathbf{n} and thus situated in the tangent plane (Figure 3.1).

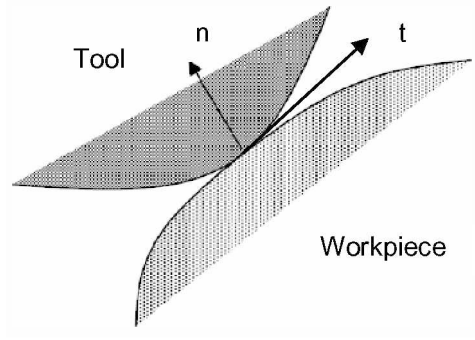


Figure 3.1: Definition of normal vector [22].

The friction between the tool and workpiece is modeled by the Norton's friction law for the pure viscoplastic behavior [20,21]:

$$\mathbf{F}_\tau = -\alpha_f K |\mathbf{v}_s|^{P_f - 1} \mathbf{v}_s \quad (3.13)$$

where \mathbf{v}_s is the relative slip velocity vector between tool and workpiece and α_f as well as P_f are the coefficients characterizing the friction, which can be determined by simple tests.

The tangential friction stress vector depends on a viscoplastic friction potential φ_f [20,21]:

$$\mathbf{F}_\tau = -\frac{\partial \varphi_f}{\partial \mathbf{v}} = -\alpha_f K \left(\frac{|\mathbf{v}_s|}{V_{ref}} \right)^{P_f} \frac{1}{|\mathbf{v}_s|} \mathbf{v}_s \quad (3.14)$$

3.3 Finite Element Formulation

On the base of the virtual power, the equilibrium equation at any time during piercing is given by:

$$\int_{\Omega} \boldsymbol{\sigma} : \dot{\boldsymbol{\varepsilon}}^* dV - \int_{\partial\Omega_v} \mathbf{F} \cdot \mathbf{v}^* dS - \int_{\partial\Omega_F} \bar{\mathbf{F}} \cdot \mathbf{v}^* dS - \int_{\partial\Omega_c} \mathbf{F}_\tau \cdot \mathbf{v}^* dS = 0 \quad (3.15)$$

With respect to the deviatoric stress tensor, ($\mathbf{s} = \boldsymbol{\sigma} + p\mathbf{I}$), the virtual velocity fields are kinematically admissible to zero (integral over $\partial\Omega_v$ is zero) [20, 22]:

$$\int_{\Omega} 2K(\sqrt{3} \dot{\epsilon}_{eq})^{m-1} \dot{\boldsymbol{\epsilon}} : \dot{\boldsymbol{\epsilon}}^* dV - \int_{\Omega} p \mathbf{I} : \dot{\boldsymbol{\epsilon}}^* dS - \int_{\partial\Omega_F} \bar{\mathbf{F}} \cdot \mathbf{v}^* dS - \int_{\partial\Omega_c} \mathbf{F}_\tau \cdot \mathbf{v}^* dS = 0 \quad (3.16)$$

In the case of incompressibility, ($\mathbf{I} : \dot{\boldsymbol{\epsilon}}^* = \text{Tr} \dot{\boldsymbol{\epsilon}}^* = \text{div} \mathbf{v}^* = 0$), the stationary condition for the velocity field functional, Φ , is given by [20, 22]:

$$\Phi(\mathbf{v}) = \int_{\Omega} \varphi(\mathbf{v}) dV - \int_{\partial\Omega_F} \bar{\mathbf{F}} \cdot \mathbf{v} dS + \int_{\partial\Omega_c} \varphi_f(\mathbf{v}) dS \quad (3.17)$$

and by introducing the weak compressibility condition [20, 22]:

$$p = -\chi_p \text{div} \mathbf{v} \quad (3.18)$$

where the penalty constant χ_p is very large and positive.

Finally, the equilibrium equation at every time step can be solved, which minimizes the following velocity field functional [20,21, 22]:

$$\Phi_p(\mathbf{v}) = \Phi(\mathbf{v}) + \int_{\Omega} \frac{\chi_p}{2} (\text{div} \mathbf{v})^2 dV \quad (3.19)$$

4. Modeling of the Rotary Piercing Process

In this chapter, the three-dimensional commercial FE-code Forge2007 was used to compute the resulting geometry of the tube, the twisting and the stretching of the groove during the forming process. In order to validate the FEM model, a new experimental method was developed and applied.

4.1 Previous Modeling Work

In the past, several studies have been done to simulate the rotary piercing process using mechanical models. Doremus and Oudin [1] analyzed the stress, strain, strain rate and final seamless tube outer diameter using a two-dimensional kinematic element model. Finite element methods provide a better understanding of the process and supply more information for the simulation of the rotary piercing process. Urbanski and Kazanecki [23] studied the strain distribution with an axisymmetric model using the two-dimensional FEM. Mori *et al.* [3, 24] proposed a simplified three-dimensional rigid plastic finite element method using generalized plane strain modeling. In their study, the cross section geometry and the occurrence of a central crack are analyzed taking into account the twisting shear deformation.

Pietsch and Thieven [8] describe of the geometry and kinematics of the rotary piercing process using the three-dimensional FE model. Capoferri *et al.* [25] predicted the fracture initiation by two-dimensional simulation and used a fracture criterion based on the maximum principal stress. Ceretti *et al.* [10] calculated stress and deformation distributions in the billet and defined the parameters affecting the cavity formation using a 3D model. Komori [7] applied the three-dimensional rigid-plastic finite element method. A method of analysis was proposed for the steady-state formulation in the case that the sides of the finite element cannot be made to coincide with the streamline of the material flow. Pater *et al.* [19] simulated the piercing process using a thermo-mechanical 3D model. In this study, strain, strain rate, mean stress and temperature distributions were determined. In another work [26], they consider the temperature changes in the plug during piercing. Reggio *et al.* [27] implemented a finite volume method to simulate the heat transfer and flow processes using the transient three-dimensional analysis.

Berazategui *et al.* [5] conducted a 3D simulation using the flow formulation, implemented via the pseudo-concentrations technique. The stress and strain distribution and the cross section geometry were obtained by this simulation. Fanini *et al.* [14] predicted the cavity formation in the centre of the billet using different damage criteria. Chiluveru [12] used the Gurson-

Tvergaard-Needleman model of porous plasticity based on the element removal technique to simulate the Mannesmann effect.

Recent investigations on the simulation of rotary piercing process and Mannesmann effect are summarized in Table 5.

Table 5: Investigation on the simulation of rotary piercing process.

Reference	Method	Model	Software	Geometry prediction	Fracture prediction	Temperature distribution	Stress, Strain, analysis
[7]	FEM	3D	-	-	-	-	+
[3]	FEM	3D	-	+	+	-	+
[1]	Kinematic	2D	-	+	-	-	+
[8]	FEM	3D	Super-form.MSC	-	-	-	+
[14]	FEM	3D	Forge	-	+	-	-
[13]	FEM	2D	Super-form.MSC	-	+	-	-
[10]	FEM	3D	Deform	-	+	-	+
[19]	FEM	3D	Super-form.MSC	+	-	+	+
[5]	FEM	3D	-	+	+	-	+
[12]	FEM	3D	-	-	+	-	+
[23]	FEM	2D	Pdrawing. Troll	-	-	-	+
[24]	FEM	3D	-	+	+	-	-
[25]	FEM	2D	Deform	-	+	-	+
[26]	FEM	3D	Super-form.MSC	+	-	+	+
[27]	FVM	2D	Star-CD.CFD	-	-	+	-
[28]	FEM	3D	Forge	-	+	-	+

4.2 Experimental Procedure

In order to validate the finite element model of rotary piercing, the numerical prediction must be compared with experimental results. For this purpose, four series of experiments (4 x 6 tests totally), in which two series were neutral types and two series were reduced types, were carried out at the piercing mill of the Voestalpine Tubulars in Kindberg. The differences between the neutral and reduced types are in the final inner and outer diameter of the hollow.

For this work stickers were performed in order to investigate the material's behavior in the forming zone. A sticker is a partially pierced billet. With the purpose of the sticker's production, process must be stopped during piercing.

Cylindrical billets from steel of St37 type (with dimensions $\varnothing 230 \times 1000 \text{ mm}$) were used as charge. On the surface of the billet thin grooves (10 mm depth and 6 mm width) were cut with distances of 90 mm from each other. It has to be mentioned that the distance between the first groove and top of the billet is 30 mm. The details are illustrated in Figure 4.1.

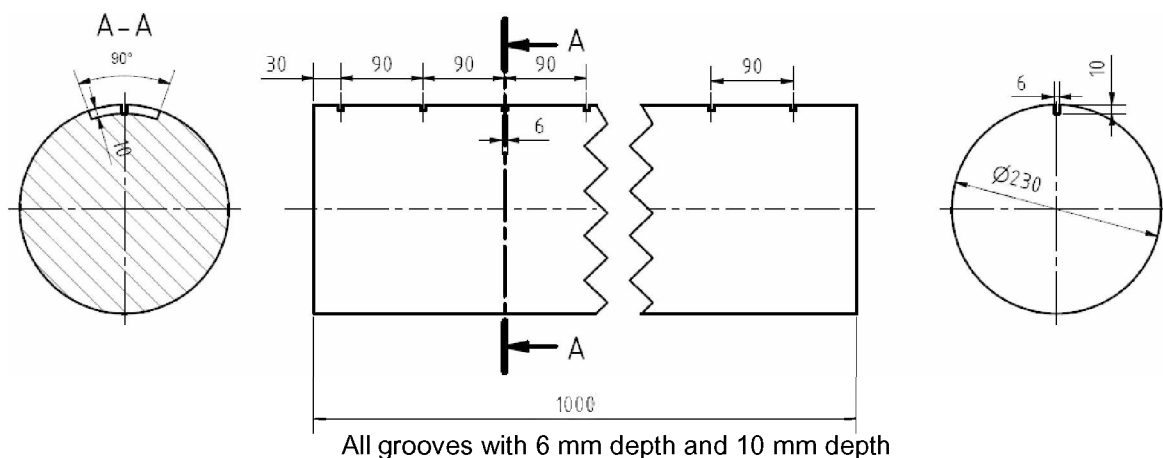


Figure 4.1: Cylindrical billet to be analyzed for the validation of the FEM model.

The piercing experiment was conducted on this billet to determine the twisting and the stretching, as shown in Figure 4.2. These parameters help to analyze the friction behavior during the forming process. The twisting and the stretching were calculated related to the coordination system. It should be pointed out that the gorge (the minimum roll gap) is the zero point.

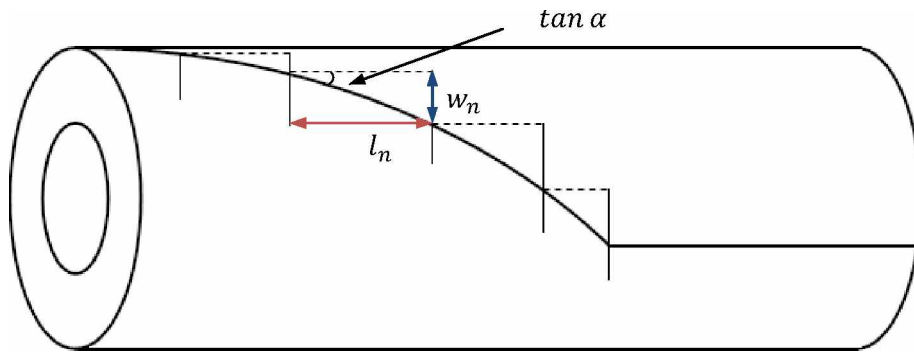


Figure 4.2: Twist and stretch of the groove.

The twisting and stretching can be calculated by equations 4.1 and 4.2:

$$Twisting = \tan \alpha = \frac{w_n}{l_n} \quad (4.1)$$

$$Stretching = \frac{l_n - 90 \text{ (30, for first step)}}{90 \text{ (30, for first step)}} \quad (4.2)$$

where w_n is the transverse twist of the groove and l_n is the longitudinal stretch of the groove.

The stickers needed to be cut into several fine segments. The outer surface and the inner surface were plotted on a paper. Subsequently, the contour lines were analyzed by a developed software. This program recognizes the domain between the outer and the inner ellipses, which are restricted with red lines, as shown in Figure 4.3.

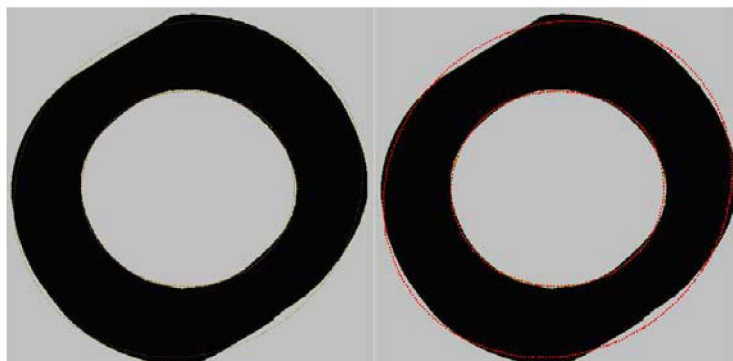


Figure 4.3: Cuttings and measurement of the contour.

Out-put data represent information about the major axis (denoted by a) and the minor axis (denoted by b) referring to the inner and the outer ellipses (Figure 4.4a).

Delta phi ($\Delta\varphi$) indicates the difference between the major axis's position of the inner and the outer ellipses (Figure 4.4b).

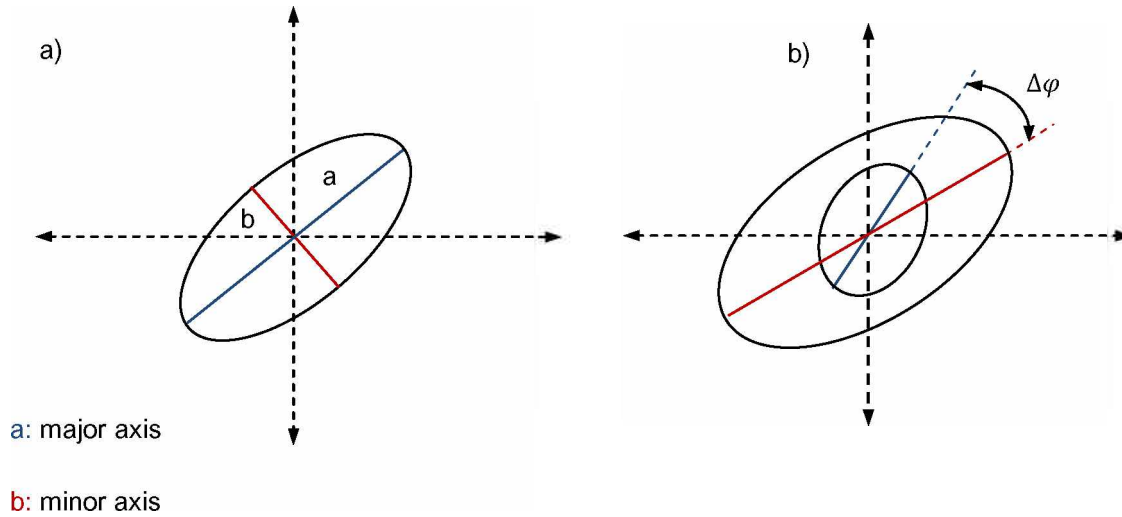


Figure 4.4: Definition of major and minor axis (a) and delta phi (b).

Hence, the outer and inner diameter of the cross sections, the thickness and delta phi ($\Delta\varphi$) related to the coordination system can be calculated from equations 4.3 - 4.5:

$$d_o = 2 \cdot \sqrt{a_o \cdot b_o} \quad (4.3)$$

$$d_i = 2 \cdot \sqrt{a_i \cdot b_i} \quad (4.4)$$

$$t = \frac{d_o - d_i}{2} \quad (4.5)$$

where d_o is the outer diameter, d_i the inner diameter, t the wall thickness of the tube, a_o the major axis of the outer ellipse, b_o the minor axis of the outer ellipse, a_i the major axis of the inner ellipse and b_i the minor axis of the inner ellipse.

These data help to compare the finite element computation with the experimental. In order to obtain the accurate position of the slice, the cutting width is taken into account. The average cutting width is estimated from the difference between the primary sticker length and the sum of the height of cuts with respect to the number of cuts.

The experiments were performed for different rolling set-ups. The following parameters were varied: feed angle, plug advance, minimum roll gap and distance between the Diescher Discs. The experimental design is outlined in Table 6.

The diameter of the rolls is different due to the mechanical reworking. The roll surface has different areas of roughness. The roll geometry and the surface roughness of the roll are illustrated in Figure 4.5. Figure 4.6 and Figure 4.7 show the calibration of the plugs and the Diescher Discs used for the rolling.

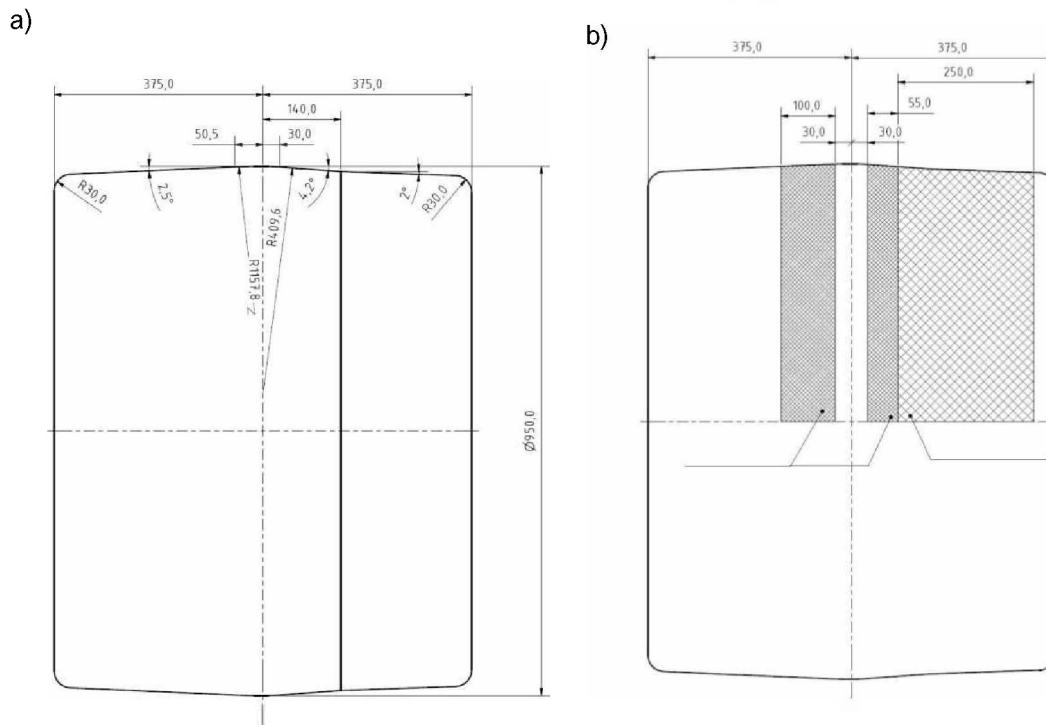


Figure 4.5: (a) Roll geometry, (b) Different areas of surface roughness.

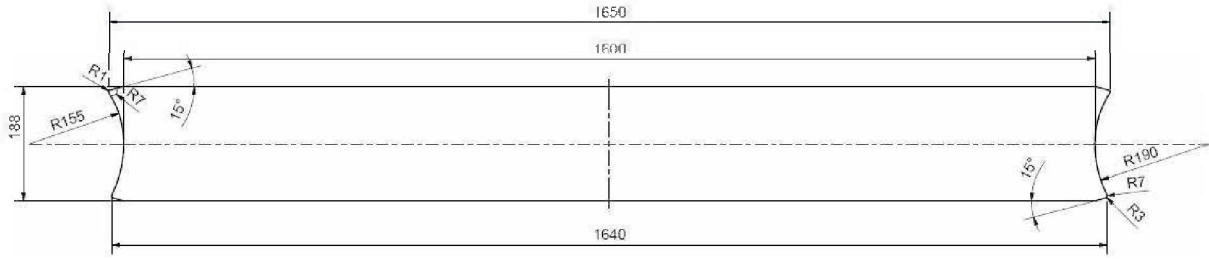
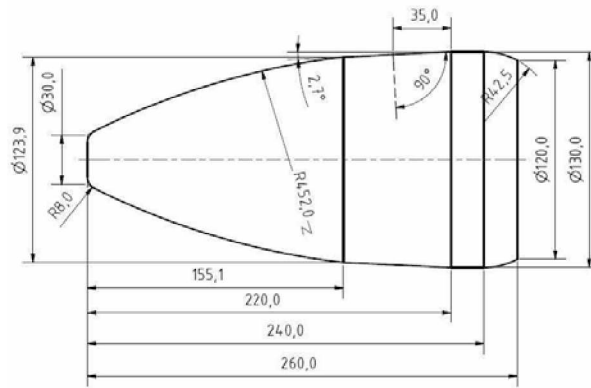


Figure 4.6: Diescher Discs geometry.

a)



b)

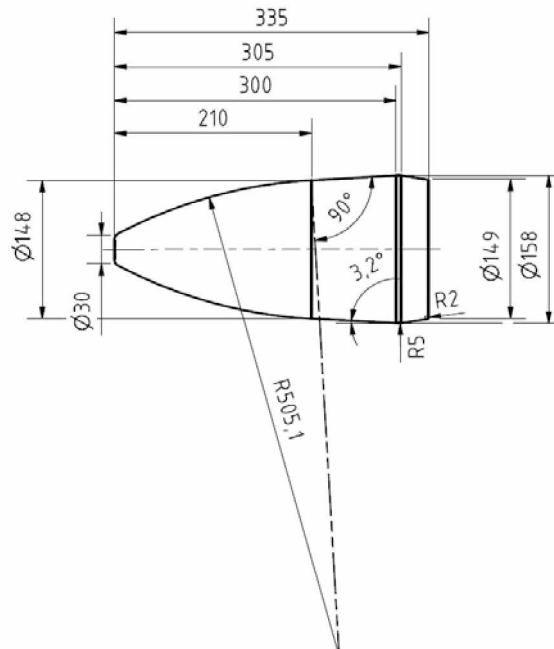


Figure 4.7: Plug geometry: (a) maximum plug diameter, 130 mm, (b) maximum plug diameter, 158 mm.

Table 6: Experimental conditions.

No.	Material	Type	A [mm]	E [mm]	γ [°]	LD [mm]	D _P [mm]	D _R [mm]
1-1	St37	neutral	215	198	9	125	158	923
1-2	St37	neutral	215	198	13	125	158	923
1-3	St37	neutral	215	198	11	125	158	923
1-4	St37	neutral	213	196	13	100	158	923
1-5	St37	neutral	213	196	11	100	158	923
1-6	St37	neutral	213	196	9	100	158	923
2-1	St37	neutral	215	198	13	125	158	907
2-2	St37	neutral	215	198	9	125	158	907
2-3	St37	neutral	213	196	13	100	158	907
2-4	St37	neutral	213	196	11	100	158	907
2-5	St37	neutral	213	196	9	100	158	907
2-6	St37	neutral	215	198	11	125	158	907
3-1	St37	reduced	210	194	13	160	130	854
3-2	St37	reduced	210	194	11	160	130	854
3-3	St37	reduced	210	194	9	160	130	854
3-4	St37	reduced	210	194	13	130	130	854
3-5	St37	reduced	210	194	11	130	130	854
3-6	St37	reduced	210	194	9	130	130	854
4-1	St37	reduced	210	194	13	160	130	925
4-2	St37	reduced	210	194	11	160	130	925
4-3	St37	reduced	210	194	9	160	130	925
4-4	St37	reduced	210	194	13	130	130	925
4-5	St37	reduced	210	194	11	130	130	925
4-6	St37	reduced	210	194	9	130	130	925

A Distance between the Diescher Discs

E Minimum roll gap

γ Feed angle

LD Plug advance

D_P Plug diameter

D_R Roll diameter

4.3 FEM Model Description

In order to simulate the cross-roll piercing process a three dimensional finite element model was developed. In the present study, firstly, four series of simulation were implemented to predict the geometry evolution, twisting, stretching. Secondly, in order to fit the experimental analysis with the numerical prediction, various friction model assumptions were employed. The analysis was conducted with the implicit commercial software Forge 2007. This software was earlier successfully used by Pschera [29] and Fanini [14] for the simulation of the cross-roll piercing process.

In the model, the objects were defined as two barrel-shaped rolls, a cylindrical billet (with dimensions $\varnothing 230 \times 900 \text{ mm}$), a plug and two support guides in type of Diescher Discs as shown in Figure 4.8. Since the elastic deformations were small, the billet was modeled as rigid-viscoplastic while other tools were considered to be rigid and not floating.

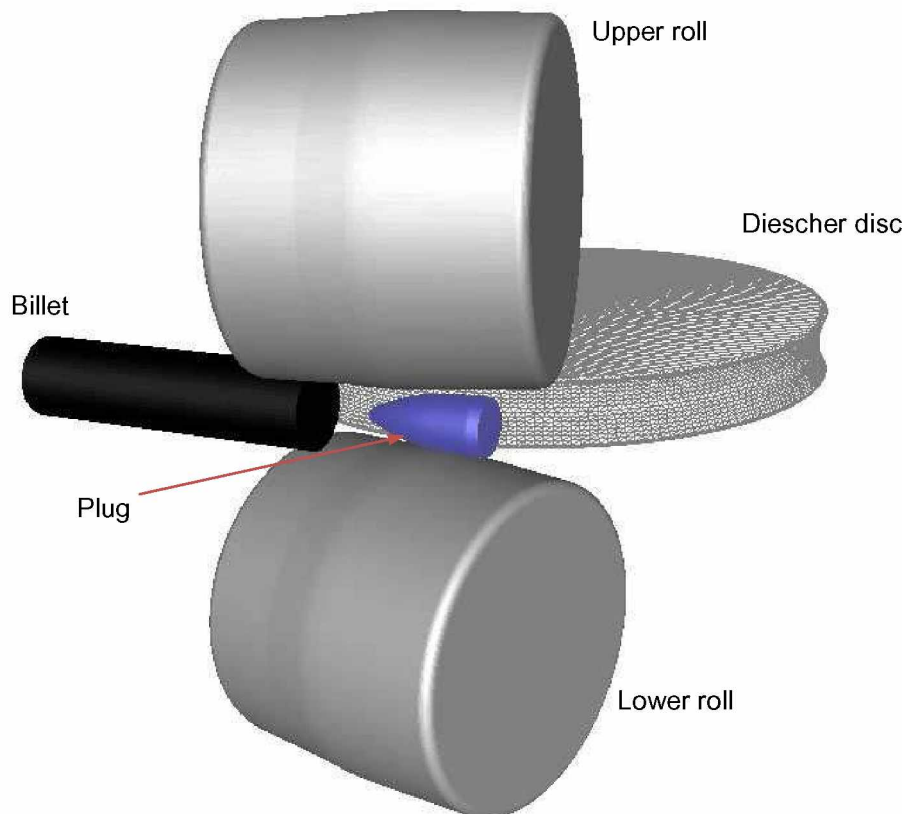


Figure 4.8: 3D view of the FEM model of the rotary piercing process.

The rotational velocity of the working rolls was 89 rpm. These rolls rotate in the same direction and their rotation axis was determined according to the feed angle. Their vertical position is determined by the roll diameter and the minimum roll gap, as given by equation 4.6 to 4.9. It should be mentioned that the upper roll had a positive rotation around the z-axis to obtain the feed angle while the lower roll had a negative rotation.

$$\text{Rotation axis, upper roll} = (-\cos\gamma, -\sin\gamma, 0) \quad (4.6)$$

$$\text{Axis point, upper roll} = \left(0, 0, \left(\frac{D_R}{2} + \frac{E}{2}\right)\right) \quad (4.7)$$

$$\text{Rotation axis, lower roll} = (-\cos\gamma, \sin\gamma, 0) \quad (4.8)$$

$$\text{Axis point, lower roll} = \left(0, 0, -\left(\frac{D_R}{2} + \frac{E}{2}\right)\right) \quad (4.9)$$

where D_R is the roll diameter, E is the minimum roll gap and γ is the feed angle.

The Diescher Discs rotated in opposite directions with the rotary velocity equal to 11.9 rpm. The Diescher Discs rotated z-axis and axis point can be calculated in relation to the Diescher Discs diameter and the distance between the Diescher Discs (equation 4.11).

$$\text{Rotation axis, Diescher Discs} = (0, 0, 1) \quad (4.10)$$

$$\text{Axis point, Diescher Discs} = \left(0, \pm\left(\frac{D_D}{2} + \frac{A}{2}\right), 0\right) \quad (4.11)$$

where D_D is the Diescher Discs diameter and A is the distance between the Diescher Discs.

With the purpose of getting information about the twisting and the stretching of the billet, a number of sensors with distance of 40 mm from each other were fixed inside the billet. Since the billet diameter changes during the forming process and the remeshing, these sensors were not set on the surface of the billet but with a distance of about 10 mm from the surface, as shown in Figure 4.9, connecting them with a finite element.

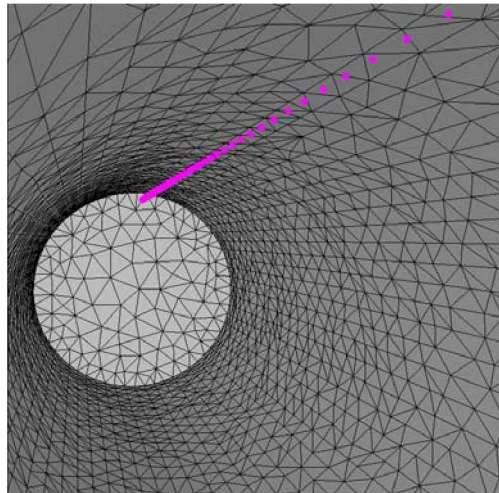


Figure 4.9: Sensors-set up in the billet.

The surface of rolls, plug and Diescher Discs were discretized in surface elements (triangle) and the billet was meshed with four-node tetrahedral elements. The remeshing procedure was performed automatically depending on the element distortion.

In the analysis of three-dimensional rotary piercing processes, the number of finite elements (mesh size) is limited due to computational time and memory capacity. Thus, in the first series of the simulations, the mesh had approximately 50233 elements and 10600 nodes (Figure 4.10a). In the center of the billet with radius 35 mm, the mesh size was finer (set equal to 6 mm) while outside of this cylinder the mesh size was coarser (set equal to 12 mm). Since the computational time with this mesh size was very long, for the second simulation series a coarser mesh was used (set as global mesh size equal to 25 mm). This mesh had about 20873 elements and 4807 nodes (Figure 4.10b). For the succeeding simulations, the mesh had around 23513 elements and 5357 nodes. In these simulations as well, in the center of the billet with radius 35 mm, the mesh size was set equal to 12, while outside of this cylinder the mesh size was equal to 24 (Figure 4.10c). The mesh sizes of each simulation are summarized in table 7.

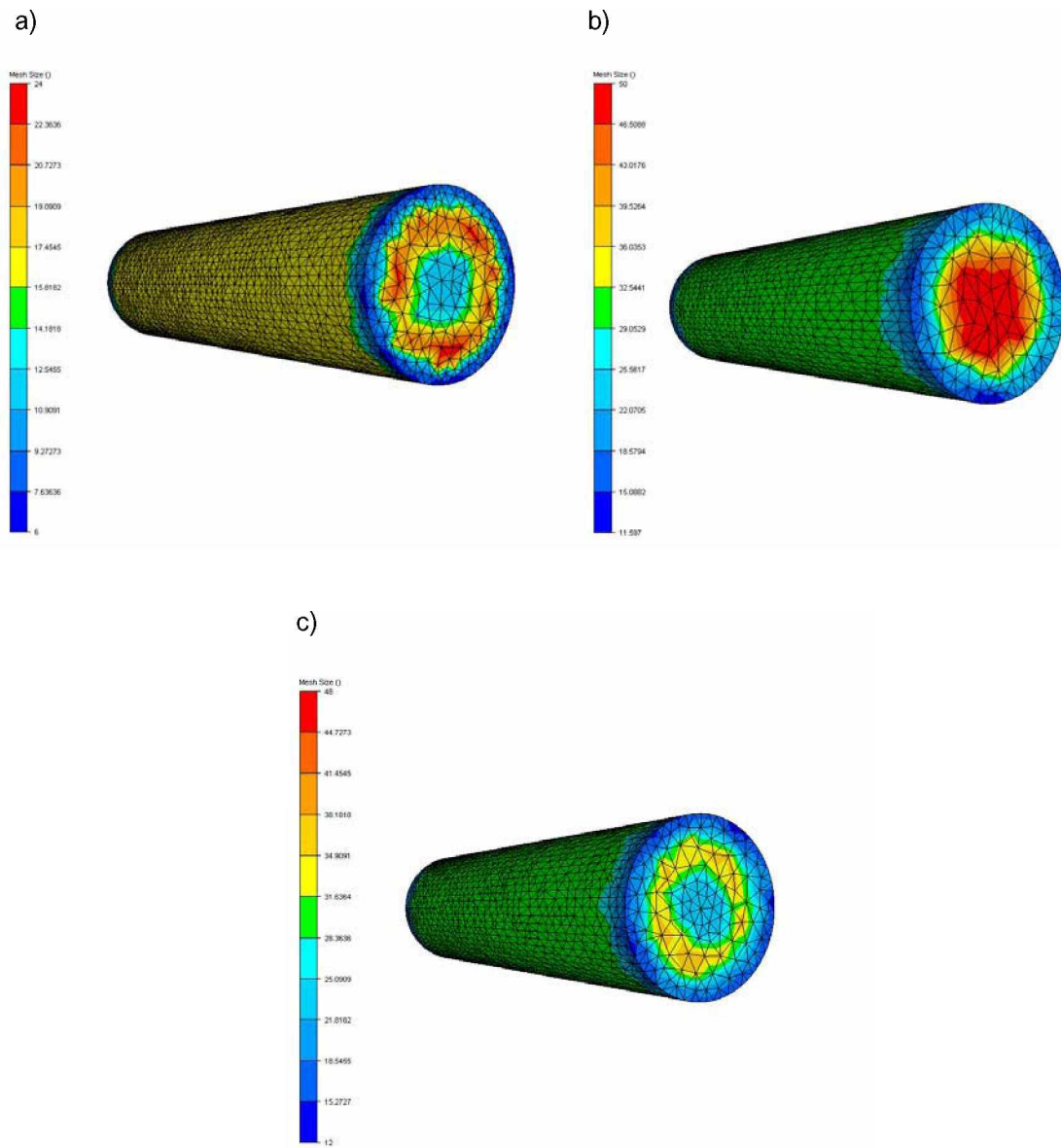


Figure 4.10: Finite element mesh: (a) 1th series, (b) 2th series, (c) 3th and 4th series.

Table 7: Mesh properties of each simulation's series.

No.	Mesh size (global, mm)	Mesh size (center, mm)	Number of elements	Number of nodes	Computational time (min/step)
1th series	12	6	50233	10600	17.48
2th series	25	25	20873	4807	2.71
3th series	24	12	23513	5357	4.16
4th series	24	12	23513	5357	3.34

The simulations were performed with an initial billet temperature equal to 1200° C while the temperatures of rolls and plug and support guides was 200 ° C. In order to reduce the

computation time, the temperature was set constant during the forming process (isothermal condition).

The material characteristics were taken from the library of the software Forge 2007. The material properties and the Hensel-Spittel parameters are listed in Table 8.

Table 8: Material properties and Hensel-Spittel's equation coefficients.

Material name	S235J
Material type	Steels
Material subtype	unalloyed C Steels
Temperature [° C]	844.8 - 1250
Strain [-]	0.04 - 1.5
Strain rate [s⁻¹]	0.01 - 500
Hensel-Spittel's equation	$\sigma_f = A e^{m_1 T} T^{m_9} \varepsilon^{m_2} e^{\frac{m_4}{\varepsilon}} (1 + \varepsilon)^{m_5 T} e^{m_7 \varepsilon} \dot{\varepsilon}^{m_3} \dot{\varepsilon}^{m_8 T}$
Hensel-Spittel's equation coefficients	$A_1=720.4452, \quad m_1=-0.00219, \quad m_2=-0.1523,$ $m_3=0.13792, \quad m_4=-0.0486, \quad m_5=m_6=m_7=m_8= m_9=0$

In the current study, simulations were divided into two parts. The first ones were related to the geometry prediction and the second ones were related to the twisting and stretching along the billet. In the first part, the friction conditions were not changed and a unique assumption was applied. However, in the subsequent part, various friction conditions were employed to coincide the experimental results with the numeric predictions.

In order to predict the geometry applying FEM model, a uniform friction model assumption was utilized to identify the friction behavior between the billet and rolls while friction between the billet and other rigid tools was considered to follow the sliding condition. This friction behavior (as global condition) assumes that the constant shear stress friction depends on the slip velocity between metal and roll. The roll surface was divided into three domains and each domain was covered with its own friction model. These domains are illustrated in Figure 4.11. Friction conditions taking place between the billet and the rolls are described by the Tresca friction model (Equation 4.12), Coulomb's friction law (Equation 4.13) and the viscoplastic friction laws (Equation 4.14):

$$F_{\tau} = m \frac{\sigma_0}{\sqrt{3}} \quad (4.12)$$

$$F_{\tau} = \mu \sigma_n \quad (4.13)$$

$$F_{\tau} = -\alpha_f K |v_s|^{P_f - 1} v_s \quad (4.14)$$

where F_{τ} is the vector of the friction forces, m the friction factor, σ_0 the base stress (flow stress of the softest material), α_f the viscoplastic friction parameter dependent on the contact surface state, P_f the strain rate sensitivity of the material, v_s the relative slip velocity vector between the tool and workpiece, μ Coulomb's friction coefficient and σ_n the normal pressure between the surfaces.

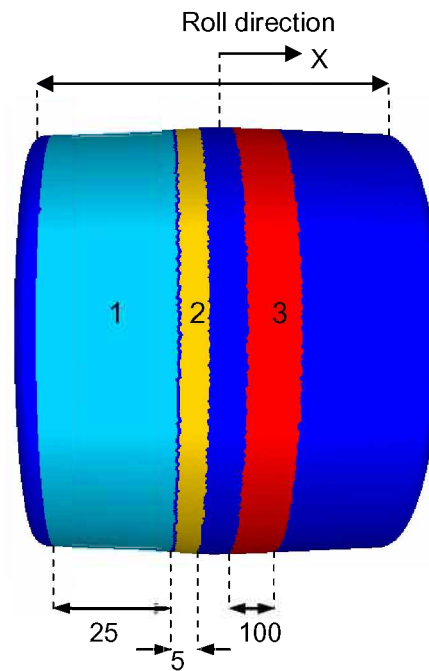


Figure 4.11: Definition of friction domains on the roll surface: (1) viscoplastic friction law with $\alpha_f = 1$, (2) viscoplastic friction law with $\alpha_f = 0.7$, (3) viscoplastic friction law with $\alpha_f = 0.7$.

The friction model in the dark blue areas as shown in Figure (4.11) was supposed to observe Tresca's law with the friction factor (m) equal to 0.45. The light blue domain followed the viscoplastic type law, in which the viscoplastic friction parameter (α_f) and the strain rate

sensitivity of the material (P_f) are 1 and 0.15, respectively. The second and third domains (yellow and red) obeyed the visco-plastic law as well, but the coefficients were $\alpha_f= 0.7$ and $P_f=0.15$, respectively. The friction behavior of the roll surface is summarized in Table 9.

Table 9: Definition of friction domains on the roll surface.

Domain	Law	Equation	Coefficient
Global	Tresca	$F_\tau = m \frac{\sigma_0}{\sqrt{3}}$	$m = 0.45$
Light blue	Viscoplastic	$F_\tau = -\alpha_f K v_s ^{P_f - 1} v_s$	$\alpha_f = 1$ $P_f = 0.15$
Yellow	Viscoplastic	$F_\tau = -\alpha_f K v_s ^{P_f - 1} v_s$	$\alpha_f = 0.7$ $P_f = 0.15$
Red	Viscoplastic	$F_\tau = -\alpha_f K v_s ^{P_f - 1} v_s$	$\alpha_f = 0.7$ $P_f = 0.15$

Another part of this thesis deals with the application of various friction models to improve the coincidence of the numerical results with the experimental data (as summarized in table 10) according to the twisting and stretching of the billet. This case was employed for the neutral and the reduced type of the rotary piercing in separate models. The material, which was used in this part, was selected from the library of the software Forge 2007. The material properties and Hensel-Spittel parameters are listed in Table 11.

Table 10: Material properties and Hensel-Spittel's equation coefficients.

Material name	10CrMo9-10
Material type	Steels
Material subtype	Cr-Mo Steels
Temperature [° C]	711.2 - 1250
Strain [-]	0.04 - 1.5
Strain rate [s⁻¹]	0.01 - 500
Hensel-Spittel's equation	$\sigma_f = A e^{m_1 T} T^{m_9} \varepsilon^{m_2} e^{\frac{m_4}{\varepsilon}} (1 + \varepsilon)^{m_5 T} e^{m_7 \varepsilon} \varepsilon^{m_3} \dot{\varepsilon}^{m_8 T}$
Hensel-Spittel's equation coefficients	$A_1=1387.0205$, $m_1=-0.0025$, $m_2=-0.05814$, $m_3=0.14668$, $m_4=-0.0346$, $m_5=m_6=m_7=m_8= m_9=0$

Table 11: Experimental condition for the validation of the FEM model according to the applied friction models.

No.	Material	Type	A [mm]	E [mm]	γ [°]	LD [mm]	D_p [mm]	D_R [mm]
NF-1	10CrMo9-10	neutral	215	198	13	125	158	925
NF-2	10CrMo9-10	neutral	215	198	13	125	158	925
NF-3	10CrMo9-10	neutral	215	198	13	125	158	925
RF-1	10CrMo9-10	reduced	210	194	13	100	130	925
RF-2	10CrMo9-10	reduced	210	194	13	160	130	925
RF-3	10CrMo9-10	reduced	210	194	12	160	130	925
RF-4	10CrMo9-10	reduced	210	194	12	160	130	925

The used friction laws on the roll surface for the different models are summarized in Table 12. In the first model of this part (RF-M1) based on the reduced type of the rotary piercing process, the application of the friction model on the surface of the roll obeyed the viscoplastic law. As shown in Figure 4.12, the blue area followed the viscoplastic type law with coefficients 1 and 0.15 for α_f and P_f , respectively, while the red area was assigned to the Tresca's law with m equal to 0.45.

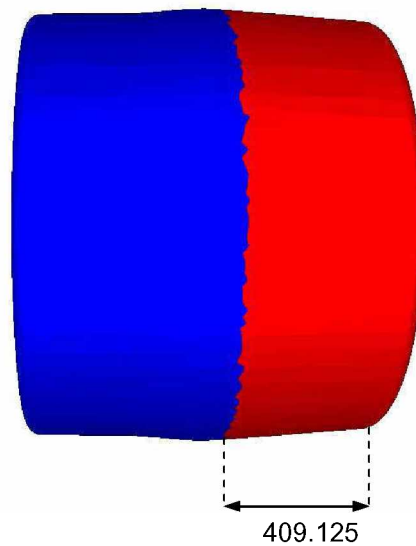


Figure 4.12: Friction domains on the roll surface in RF-M1.

In the simulations RF-M2, RF-M3, NF-M1 and NF-M2 the roll surface was divided into three domains as in the first part of the study (geometry prediction) (Figure 4.11).

Table 12: Definition of the new friction models.

Label	Type	Domain	Law	Equation
RF-M1	reduced	global	Viscoplastic	$F_{\tau} = -K v_s ^{-0.85}v_s$
		red	Tresca	$F_{\tau} = \frac{\sigma_0}{\sqrt{3}}$
RF-M2	reduced	global	Viscoplastic	$F_{\tau} = -0.7K v_s ^{-0.85}v_s$
		light blue	Viscoplastic	$F_{\tau} = -K v_s ^{-0.85}v_s$
		yellow	Viscoplastic	$F_{\tau} = -0.9K v_s ^{-0.85}v_s$
		red	Viscoplastic	$F_{\tau} = -K v_s ^{-0.85}v_s$
RF-M3	reduced	global	Tresca	$F_{\tau} = 0.8 \frac{\sigma_0}{\sqrt{3}}$
		light blue	Viscoplastic	$F_{\tau} = -K v_s ^{-0.85}v_s$
		yellow	Tresca	$F_{\tau} = \frac{\sigma_0}{\sqrt{3}}$
		red	Tresca	$F_{\tau} = \frac{\sigma_0}{\sqrt{3}}$
NF-M1	neutral	global	Viscoplastic	$F_{\tau} = -0.7K v_s ^{-0.85}v_s$
		light blue	Viscoplastic	$F_{\tau} = -K v_s ^{-0.85}v_s$
		yellow	Viscoplastic	$F_{\tau} = -0.9K v_s ^{-0.85}v_s$
		red	Viscoplastic	$F_{\tau} = -0.9K v_s ^{-0.85}v_s$
NF-M2	neutral	global	Viscoplastic	$F_{\tau} = -0.7K v_s ^{-0.85}v_s$
		light blue	Viscoplastic	$F_{\tau} = -K v_s ^{-0.85}v_s$
		yellow	Viscoplastic	$F_{\tau} = -0.9K v_s ^{-0.85}v_s$
		red	Tresca-1	$F_{\tau} = \frac{\sigma_0}{\sqrt{3}}$

5. Results and Discussion

In the following chapters the effect of the rolling conditions is discussed and the validation of the model is shown.

5.1 Effect of Feed Angle on the Geometry

The influence of the feed angle on the average outer diameter (d_a) is shown in Figure 5.1. In the forming zone (approximately at coordinate +200 to -200) the outer diameter reaches a minimum value, which always is reasonable in the gorge. It can be seen that with increasing feed angle the average billet diameter increases slightly behind the gorge (minimum roll gap, $x=0$). This is because that the minimum distance between the rolls increases with raising the feed angle resulting in a larger outer tube diameter. Figure 5.1(b) illustrates that the variation of the average outer diameter with feed angle is less for the reduced type of rotary piercing process.

Figure 5.2 shows the effect of the feed angle on the average inner diameter (d_i). It can be observed that the final inner diameter is achieved when the billet passes the forming zone and then the inner diameter reaches a constant value. With increasing feed angle the inner diameter changes negligibly. The inner diameter more depends on the plug diameter and becomes larger by increasing the plug diameter [7]. Figure 5.2(b) shows the same behavior for the reduced type of rotary piercing.

The influence of the feed angle on the wall thickness of the tube (t) is illustrated in Figure 5.3. It can be observed that a feed angle variation does not present any remarkable changes on the thickness of the tube. Figure 5.3(b) shows the same behavior for the reduced type of rotary piercing.

Figure 5.4 depicts the effect of the feed angle on the twisting along the sticker during the forming process. Clearly it can be seen that the maximum amount of twisting occurs in the forming zone, which becomes larger with increasing feed angle and following the magnitude of twisting becomes smaller to the end of the sticker where it increases again. The reason is that the friction force along the rolling direction increases with increasing feed angle, since the contact area gets larger. On the other hand, generally, the forward motion of the billet is caused by the inclination of the axes of the rolls and it has been found that as the feed angle increases, the forming velocity becomes higher; thus, the friction forces along the rolling direction (x -component) are higher. Figure 5.4(b) shows the same effect for the reduced type of rotary piercing.

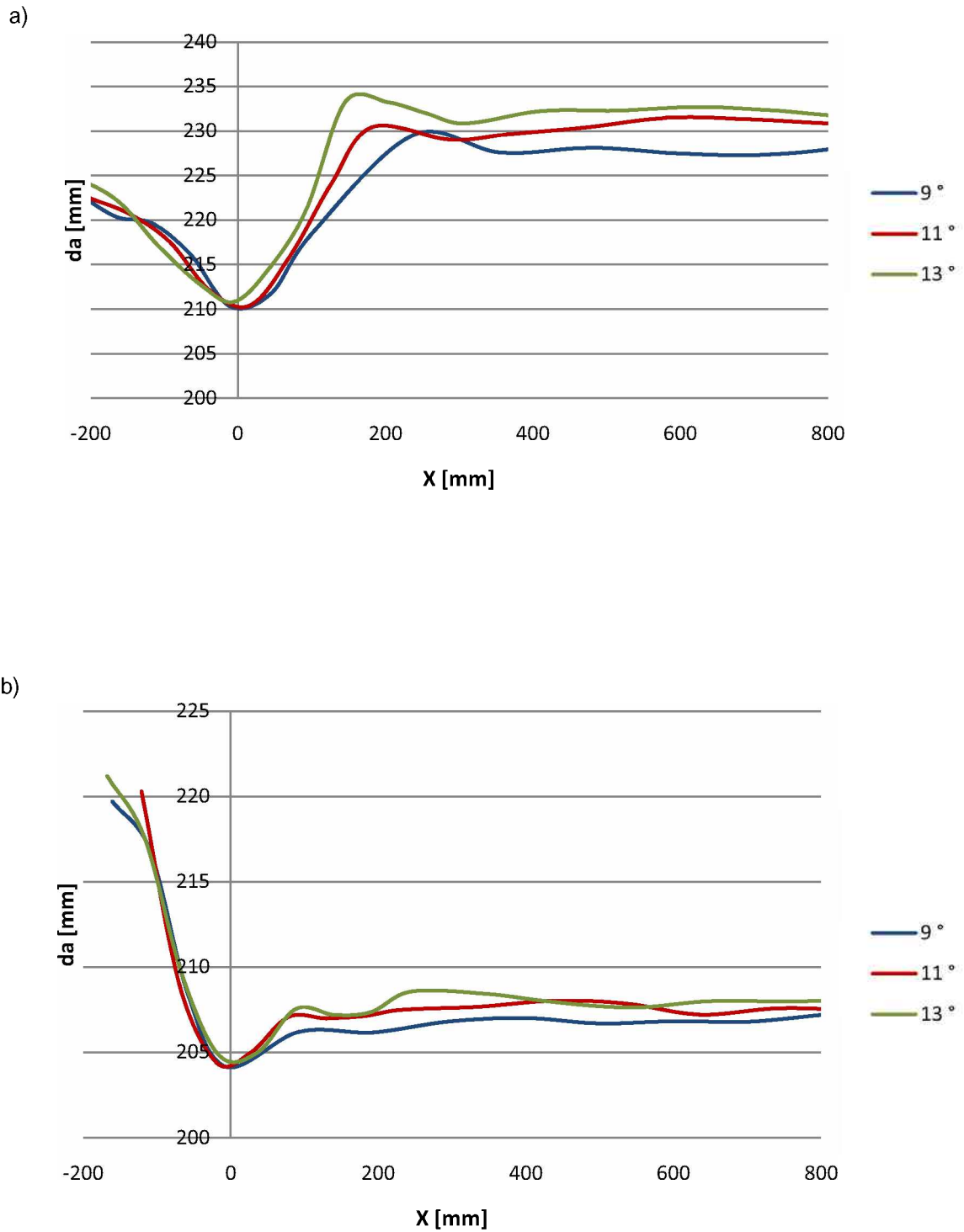


Figure 5.1: Effect of feed angle on the average outer diameter: (a) neutral type, comparison between experiments No. 1-4, 1-5, 1-6, (b) reduced type, comparison between experiments No. 4-4, 4-5, 4-6.

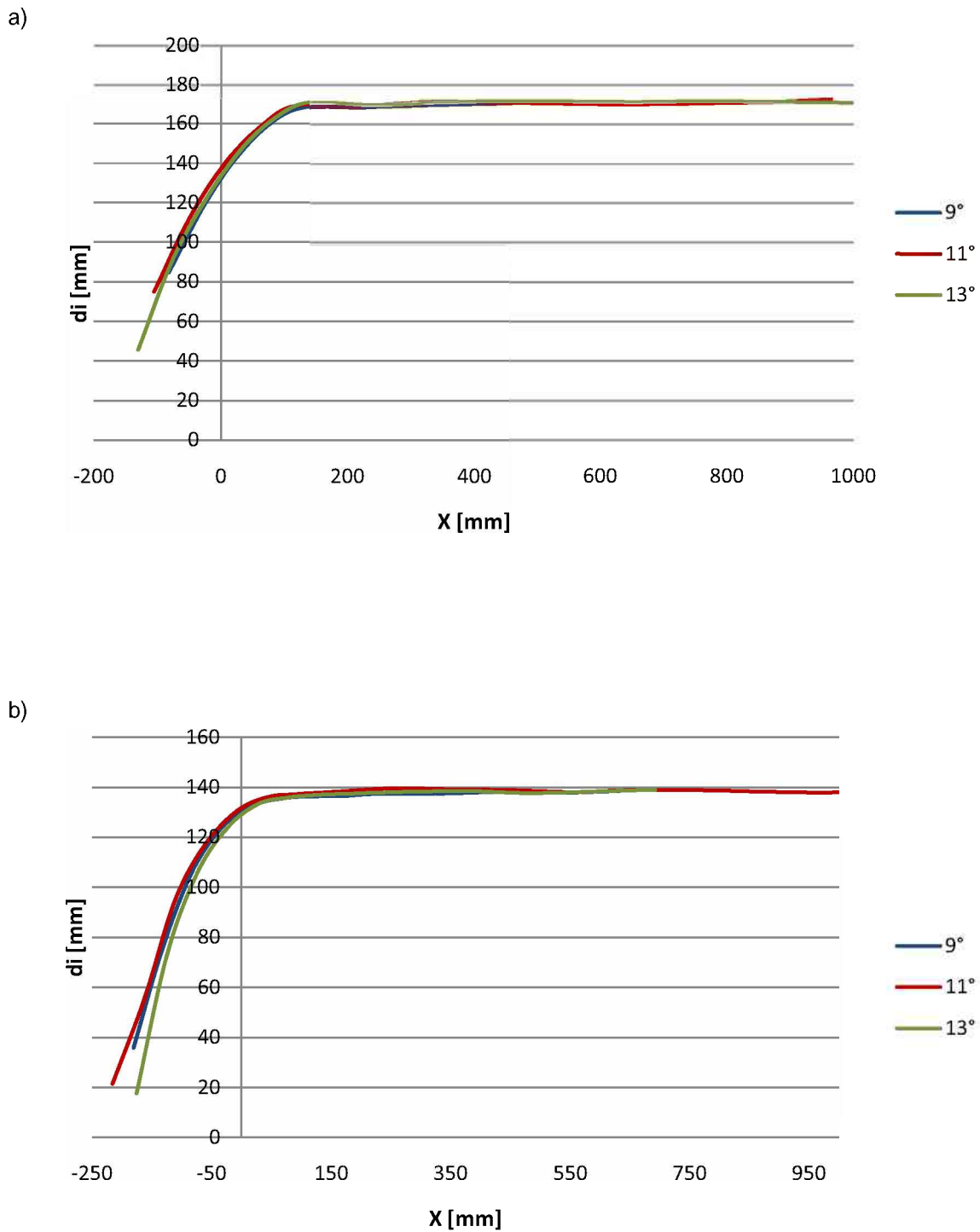


Figure 5.2: Effect of feed angle on the average inner diameter: (a) neutral type, comparison between experiments No. 1-1, 1-2, 1-3, (b) reduced type comparison between experiments No. 4-1, 4-2, 4-3.

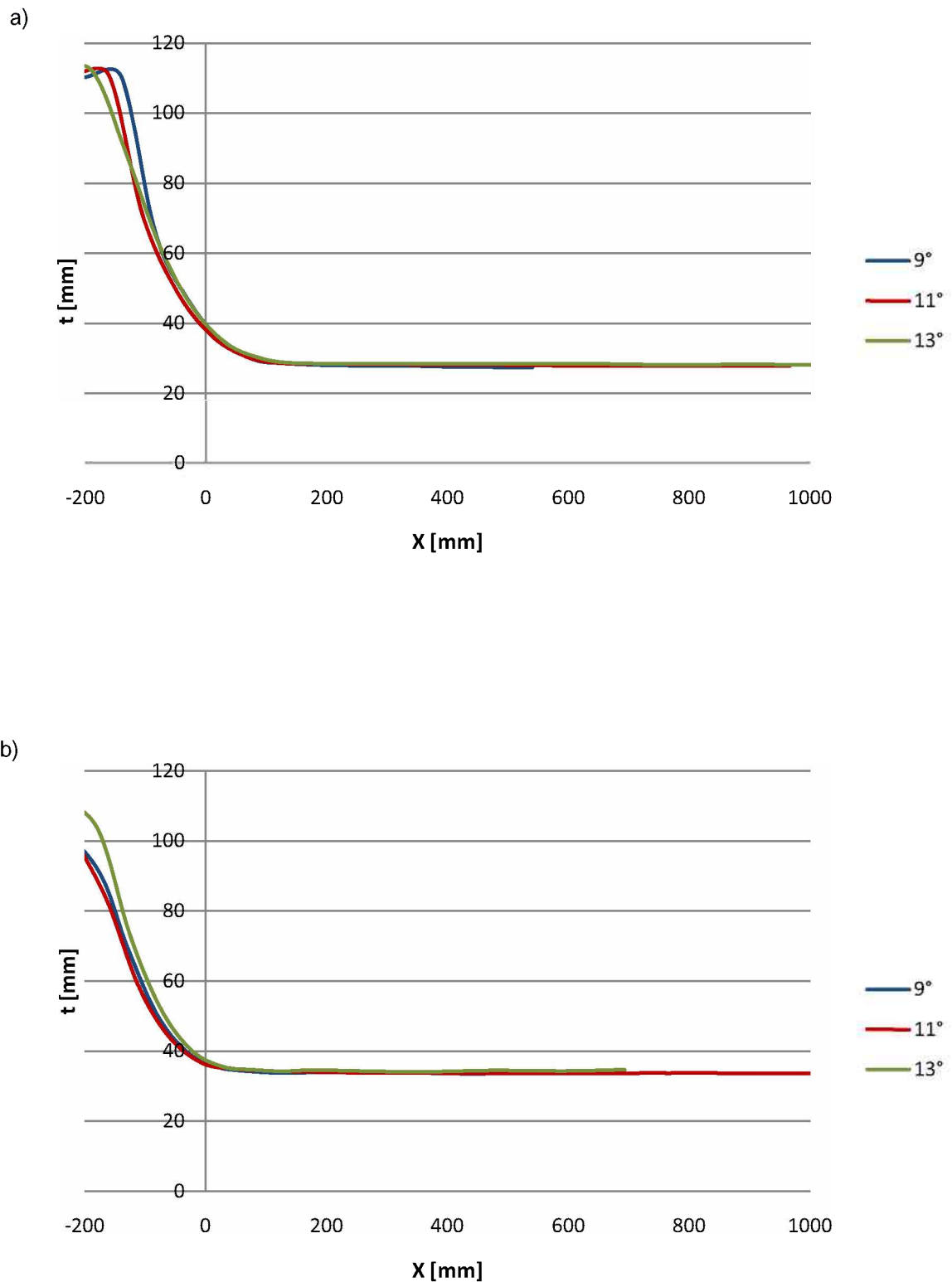


Figure 5.3: Effect of feed angle on the wall thickness: (a) neutral type, comparison between experiments No. 1-1, 1-2, 1-3, (b) reduced type comparison between experiments No. 4-1, 4-2, 4-3.

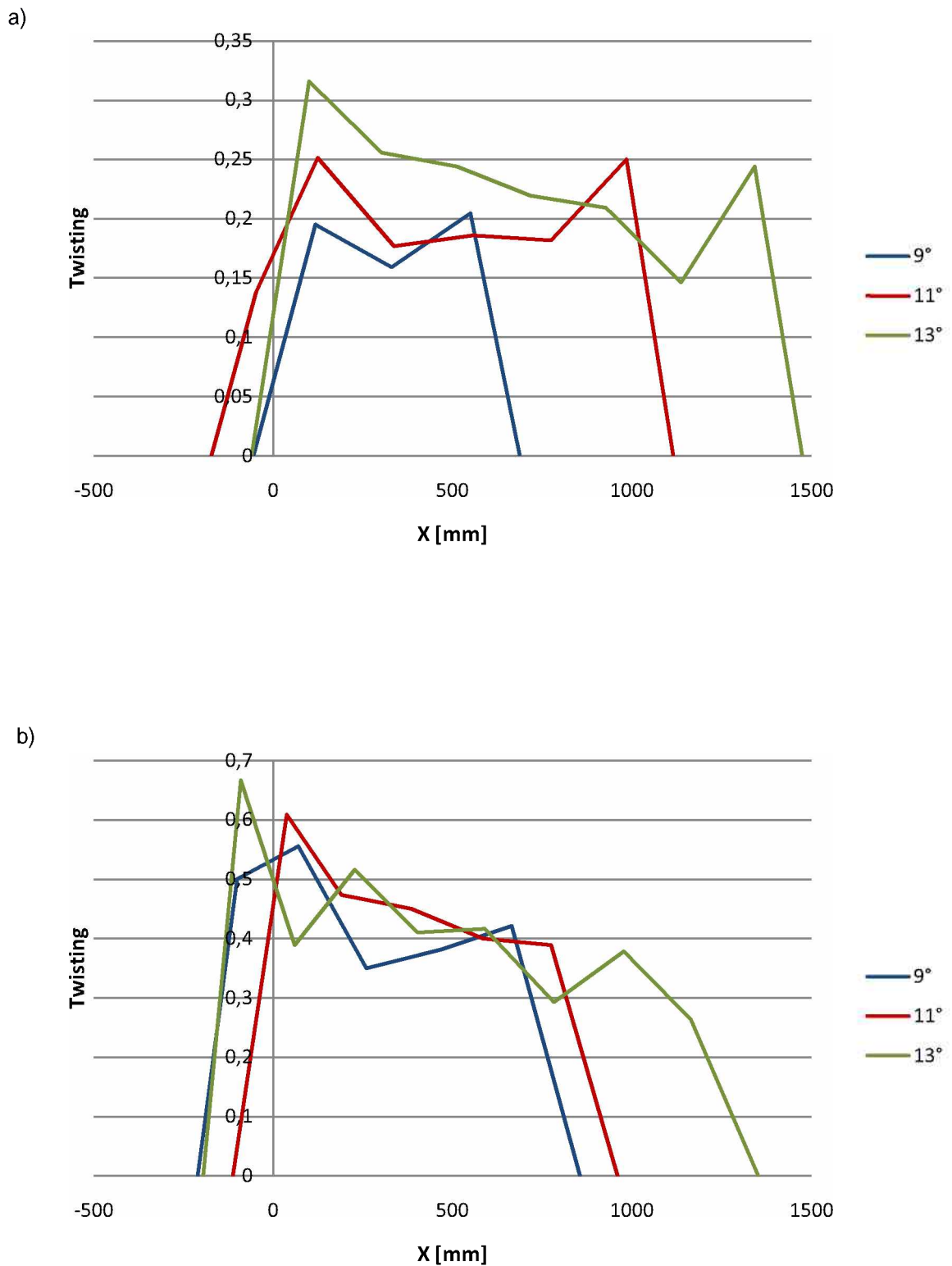


Figure 5.4: Effect of feed angle on the twisting along the rolling direction: (a) neutral type, comparison between experiments No. 1-1, 1-2, 1-3, (b) reduced type, comparison between experiments No. 3-4, 3-5, 3-6.

5.2 Effect of Plug Advance on the Geometry

Figure 5.5 illustrates the variation of the average outer diameter (d_a) with the plug advance. It can be seen that as the plug advance increases, the average outer diameter decreases. The differences are more remarkable when the billet passes the forming zone. Figure 5.5(b) shows that this declaration is also valid for the reduced type of the rotary piercing but the changes are less than with neutral type.

The influence of the plug position on the average inner diameter (d_i) is shown in Figure 5.6. It can be observed that the final inner diameter is not affected by the plug position. A notable difference occurs in the forming zone where the central cavity is created first. As illustrated, the average inner diameter increases with increasing the plug advance. Figure 5.6(b) shows the same behavior for the reduced type of rotary piercing.

Figure 5.7 shows the change in the wall thickness (t) during the rotary piercing process. In this figure, the wall thickness decreases with increasing the plug advance in the forming zone but, finally, achieves a constant value. Figure 5.7(b) shows that this statement is accurate for the reduced type of rotary piercing as well.

Figure 5.8 indicates that the plug position does not have a significant influence on the magnitude of twisting. Therefore, the twisting is affected by varying the minimum roll gap and the distance between the Diescher Discs as shown in Figure 5.9. With increasing the minimum roll gap and the distance between the Diescher Discs, the magnitude of twisting shifts to higher values. The reason could be that the roll forces decrease by increasing these parameters and the material may rotate more around itself as it moves forward, thus, the billet stays a longer period of time in contact with tools.

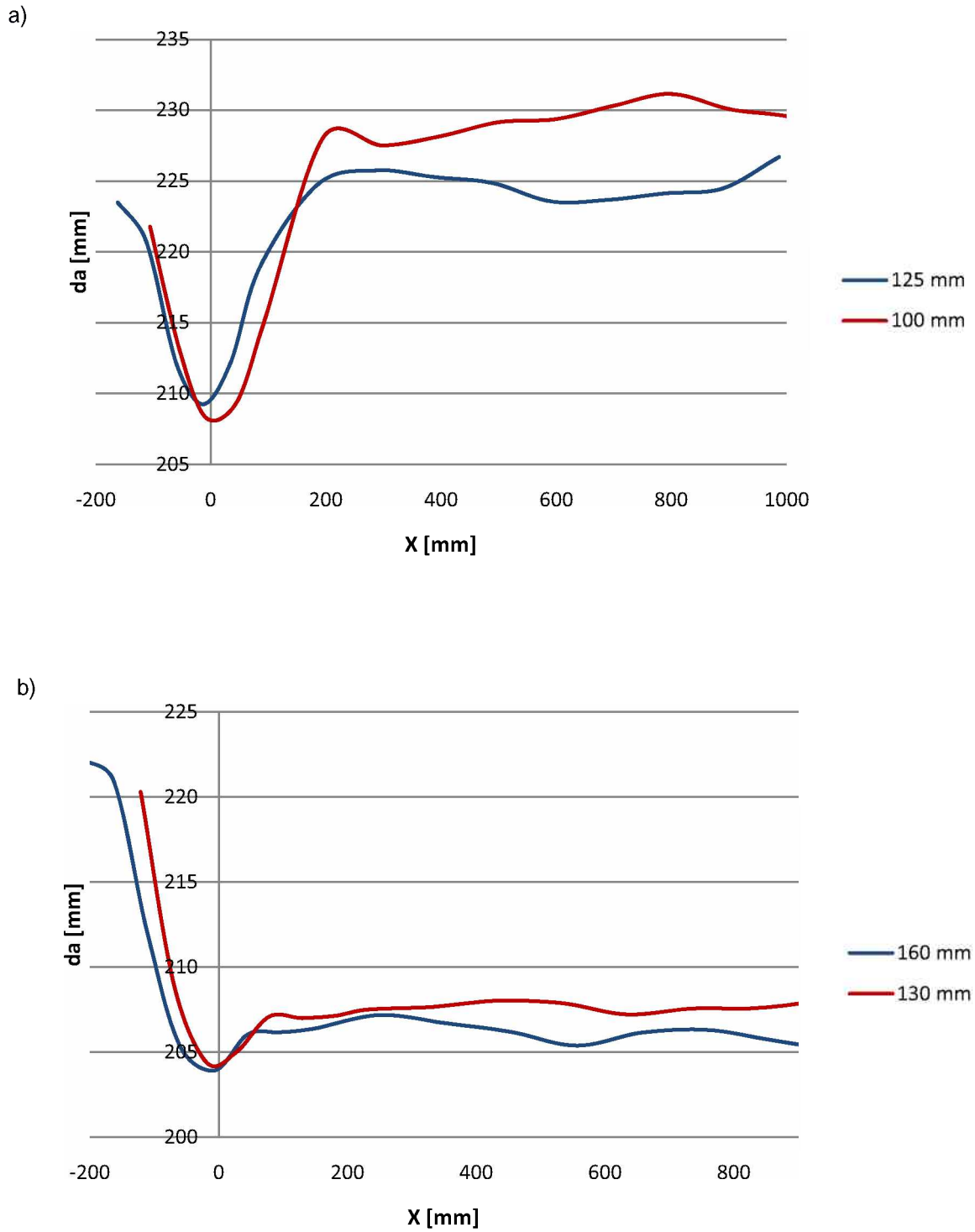


Figure 5.5: Effect of plug advance on the average outer diameter: (a) neutral type, comparison between experiments No. 2-1, 2-4, (b) reduced type, comparison between experiments No. 4-2, 4-5.

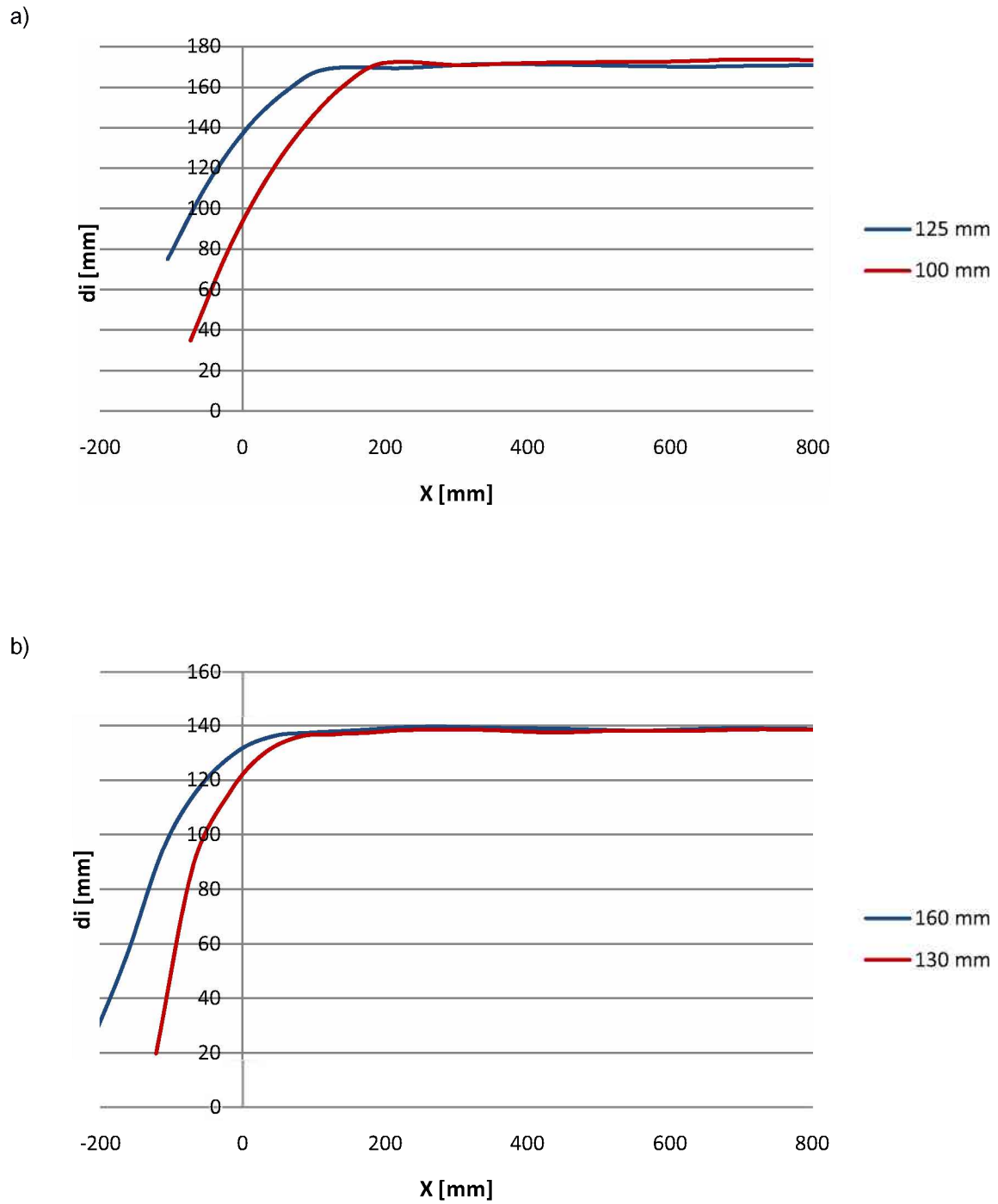


Figure 5.6: Effect of plug advance on the average inner diameter: (a) neutral type, comparison between experiments No. 1-3, 1-5 (b) reduced type, comparison between experiments No. 4-2, 4-5.

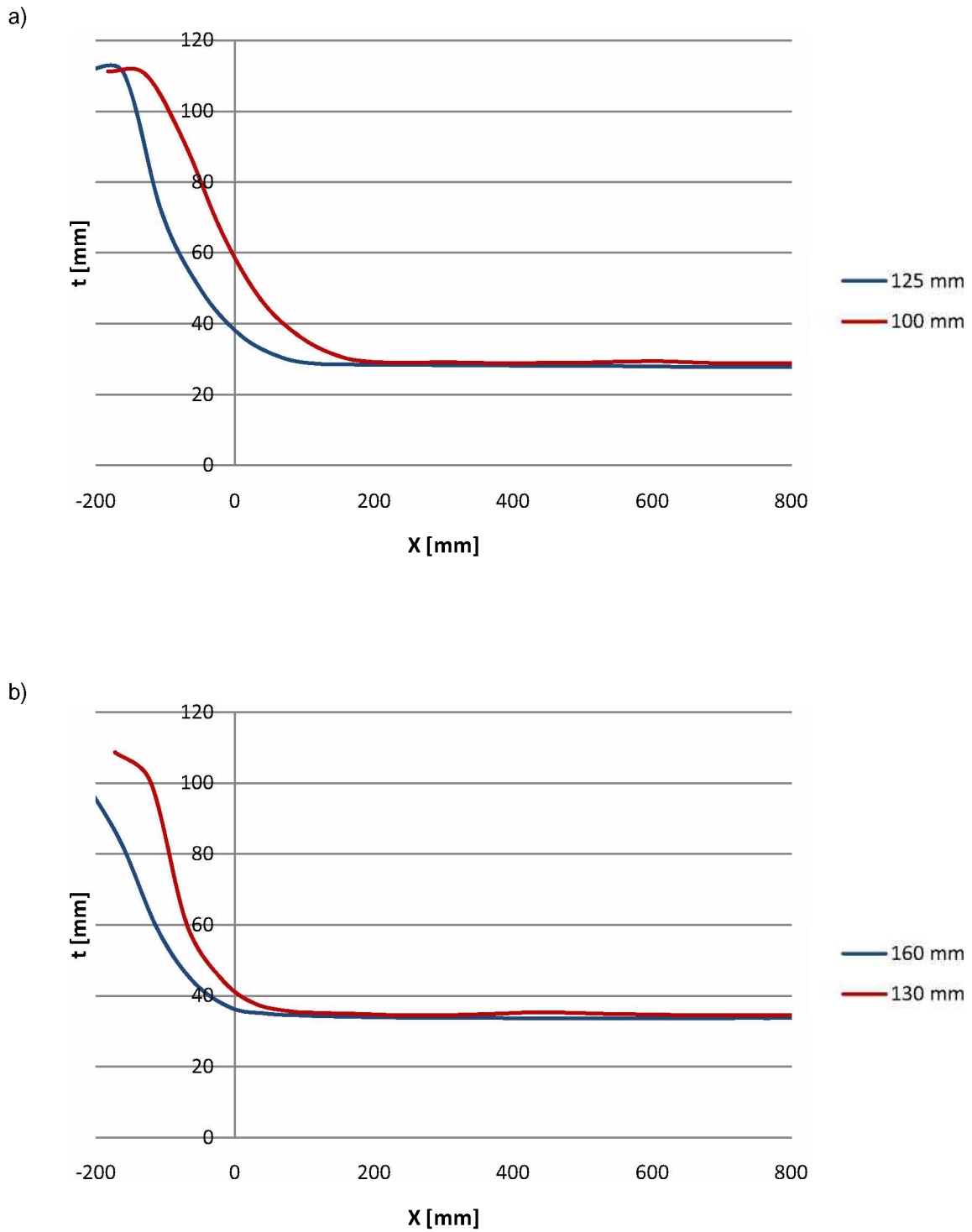


Figure 5.7: Effect of plug advance on the wall thickness: (a) neutral type, comparison between experiments No. 1-3, 1-5 (b) reduced type, comparison between experiments No. 4-2, 4-5.

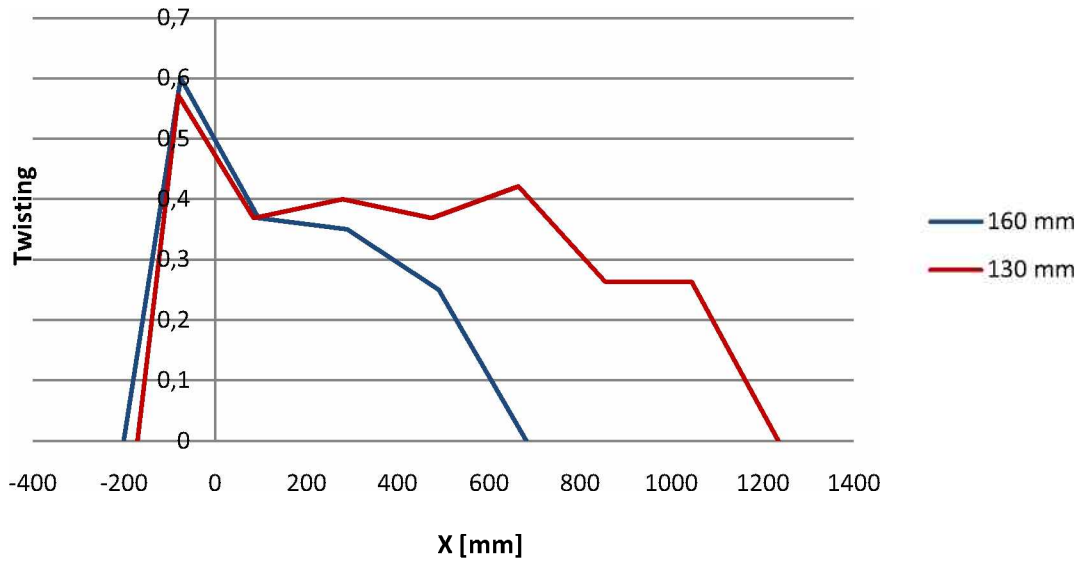


Figure 5.8: Effect of plug advance on the twisting along the rolling direction, reduced type, comparison between experiments No. 4-1, 4-4.

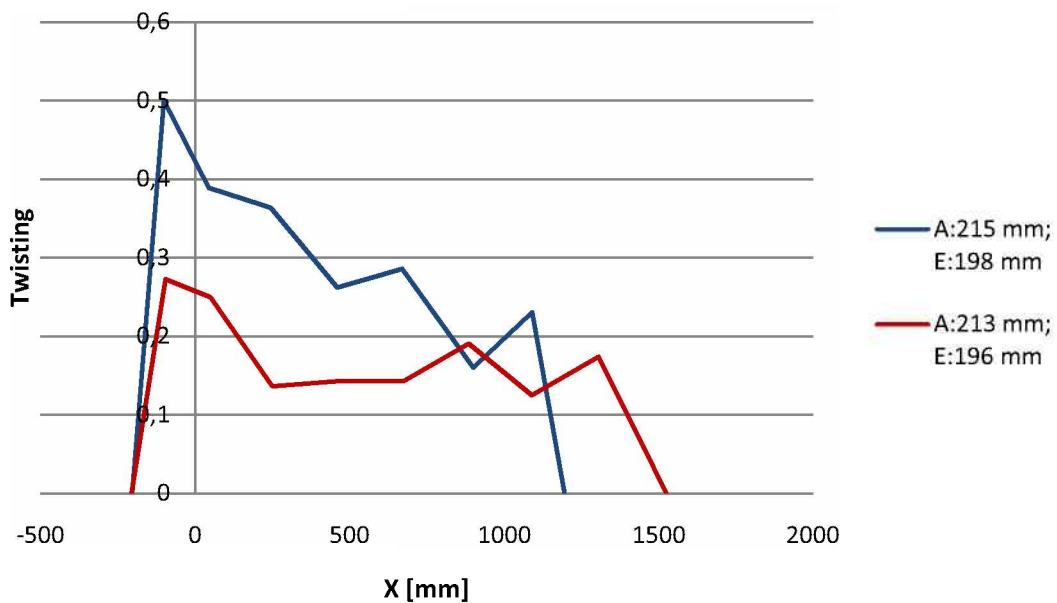


Figure 5.9: Effect of the minimum roll gap and the distance between the Diescher discs on the twisting along the rolling direction, neutral type, comparison between experiments No. 2-3, 2-5.

5.3 Effect of Feed Angle on the Forces

In this section, the effects of feed angle on the force parameters are studied. The results based on the FEM-calculation are given in Figure 5.10. It can be seen that as the feed angle increases, the roll force increases slightly in the beginning and then tend to reach a steady state (Figure 5.10a). Figure 5.10b shows that with increasing the feed angle, the mandrel force increases. The high axial movement of material may be a cause of this increase. Figure 5.10c illustrates the variation of roll torque with the feed angle. It can be observed that the roll torque increases at first and then it changes negligibly. Furthermore, the changes of Diescher Discs force with the feed angle are not notable. The Diescher Discs force depends on the distance between the discs (Figure 5.10d).

On the base of the reduced type, it can be seen that the magnitude of all the forces are lower than with the neutral type of the piercing process.

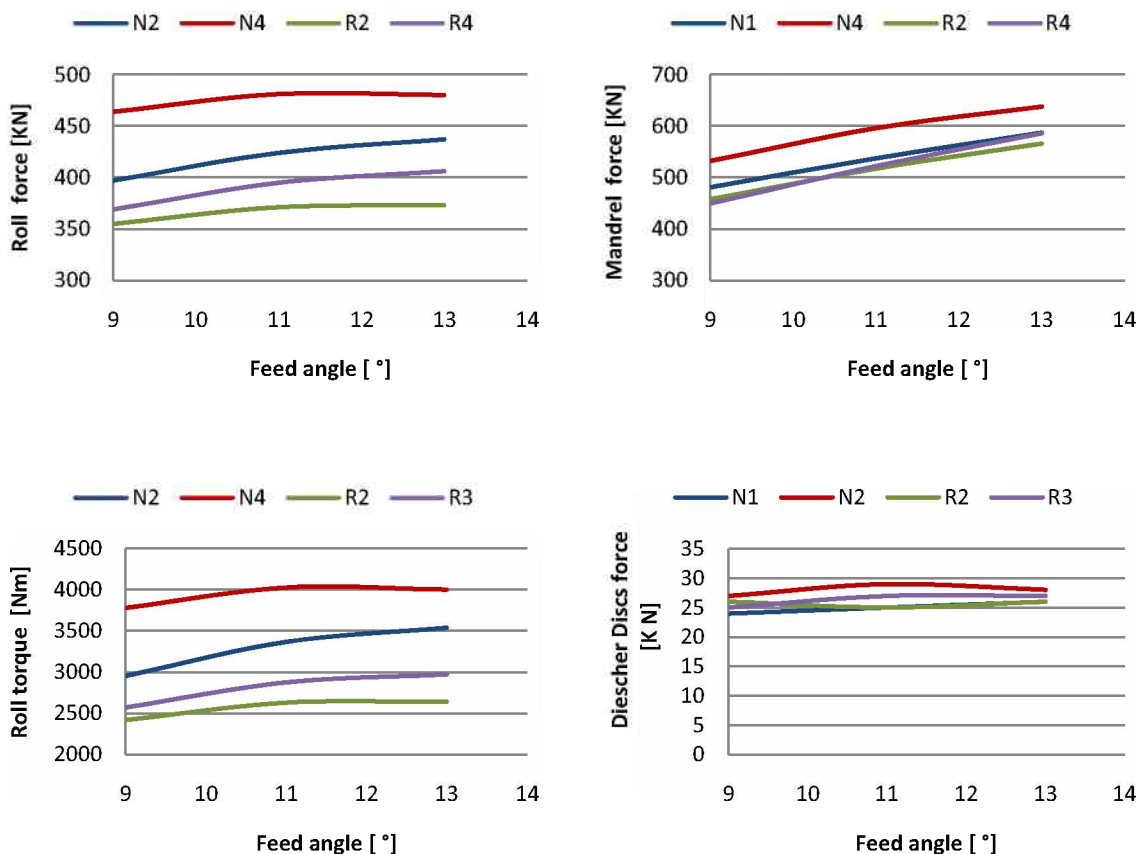


Figure 5.10: Effect of feed angle on the roll force (a), mandrel force (b), roll torque (c) and the Diescher Discs force for the neutral (N) and reduced (R) type.

5.4 Effect of Plug Advance on the Forces

The effect of plug advance on the roll force, mandrel force, roll torque and Diescher Discs force using FEM-calculation are illustrated in Figure 5.11. It is observed that as the plug advance increases, the roll force decreases, as shown in Figure 5.11a. The reason is that if the plug is located more in the front, the effective surface will decrease [7]. Figure 5.11b depicts that the mandrel force increases with the plug advance but the variation is not remarkable. The mandrel force practically does not change with the plug advance in the reduced type of the rotary piercing process.

Clearly it can be seen in Figure 5.11c that the position of plug affects the magnitude of roll torque. By increasing the plug advance, the roll torque decreases but it is more notable in case of the neutral rolling type.

Figure 5.11d shows that the Diescher Discs force decreases with the plug advance, but the variation is not significant.

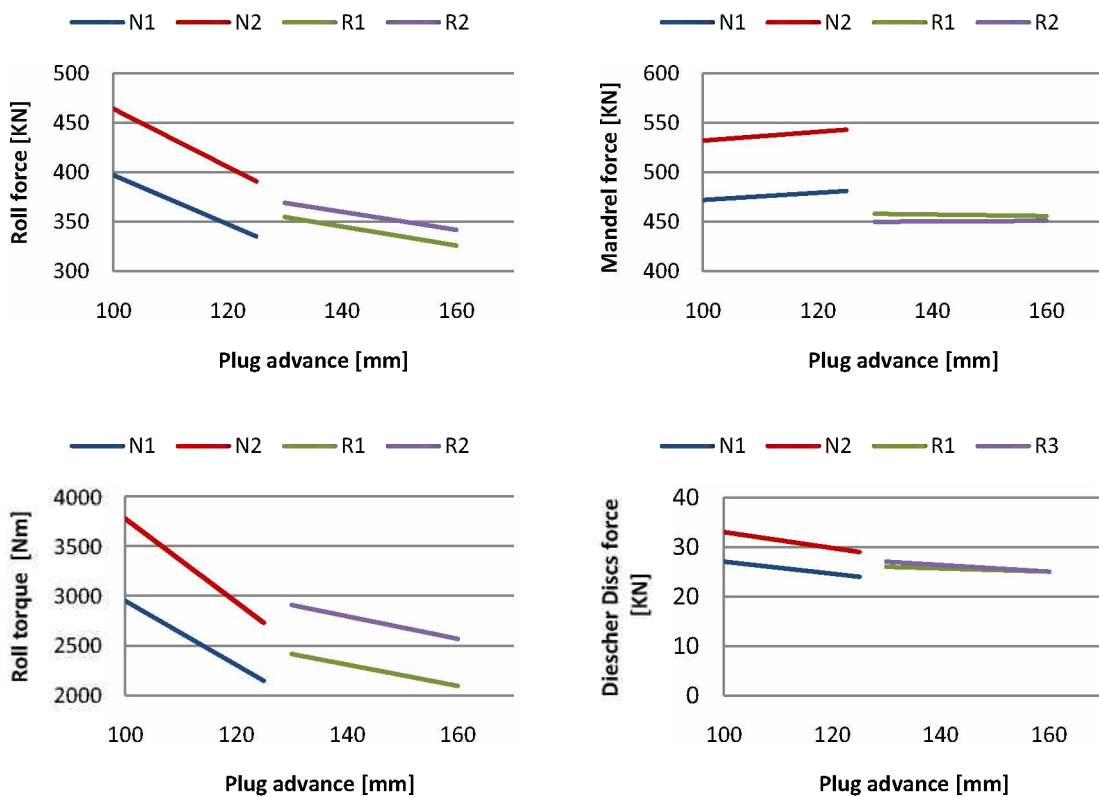


Figure 5.11: Effect of plug advance on the roll force (a), mandrel force (b), roll torque (c) and the Diescher Discs force for the neutral (N) and reduced (R) type.

5.5 Model Validation

In order to verify the FE-model, the results of experiments are compared with the calculations in the following sections.

5.5.1 Model Validation According to the Geometry

Experimental results of average outer diameter, inner diameter and wall thickness are compared with computed results in Figure 5.12. Comparison of the changes in average outer diameter (blue curves) shows that the agreement between the FEM-calculation and the experiment is almost perfect. Because of scaling of the billet in the rotary hearth furnace, the billet diameter is smaller than the FEM prediction at the beginning of the forming process. It can be seen that the final outer diameter calculated by FEM becomes slightly smaller than the experimental determination. It may be explained with respect to the stronger ovality due to the material's volume dilatation as the billet passes the minimum roll gap in experimental condition [29]. Exact coincidence reaches where the material stays in contact with the tools.

Red curves in Figure 5.12 represent the average inner diameter calculated by FEM and that obtained by the experiment. It can be observed that the FEM computation agrees with the experimental result. There is a difference between the diameters at the beginning of the hollow formation. The plug wear condition may be a cause of this dissimilarity. In addition, the shape of the plug tip varies during the forming process and that affects the hollow formation at the first steps. Here it can be seen that the model can predict the final inner diameter very exactly.

The wall thickness variations during the process along the rolling direction are indicated in Figure 5.12 by green curves. Clearly it can be seen that the FEM-calculated wall thickness coincide with the experimental results and the final wall thickness can be predicted exactly. The discrepancy at the very beginning of the process can be explained as above.

Figure 5.13 shows the same comparison with respect to the reduced rolling type. It can be seen that the difference between FEM and experiment in the forming zone is larger than with the neutral type but the final prediction is more exact.

Figure 5.14 represents the difference between the major axis' rotation of the inner and the outer ellipses along the rolling direction, which is denoted by delta phi ($\Delta\varphi$). Comparison of the variations in delta phi ($\Delta\varphi$) shows that the agreement between FEM-calculation and experiment is good in term of trends but not in term of magnitudes. Several reasons can be given for this discrepancy. In experiments the plug rotates around itself with different

peripheral velocity in comparison to the billet. Furthermore, some uncertainties are obviously associated with the friction conditions on the plug's surface. Figure 5.12(b) shows the same statement in case of the reduced type of rotary piercing.

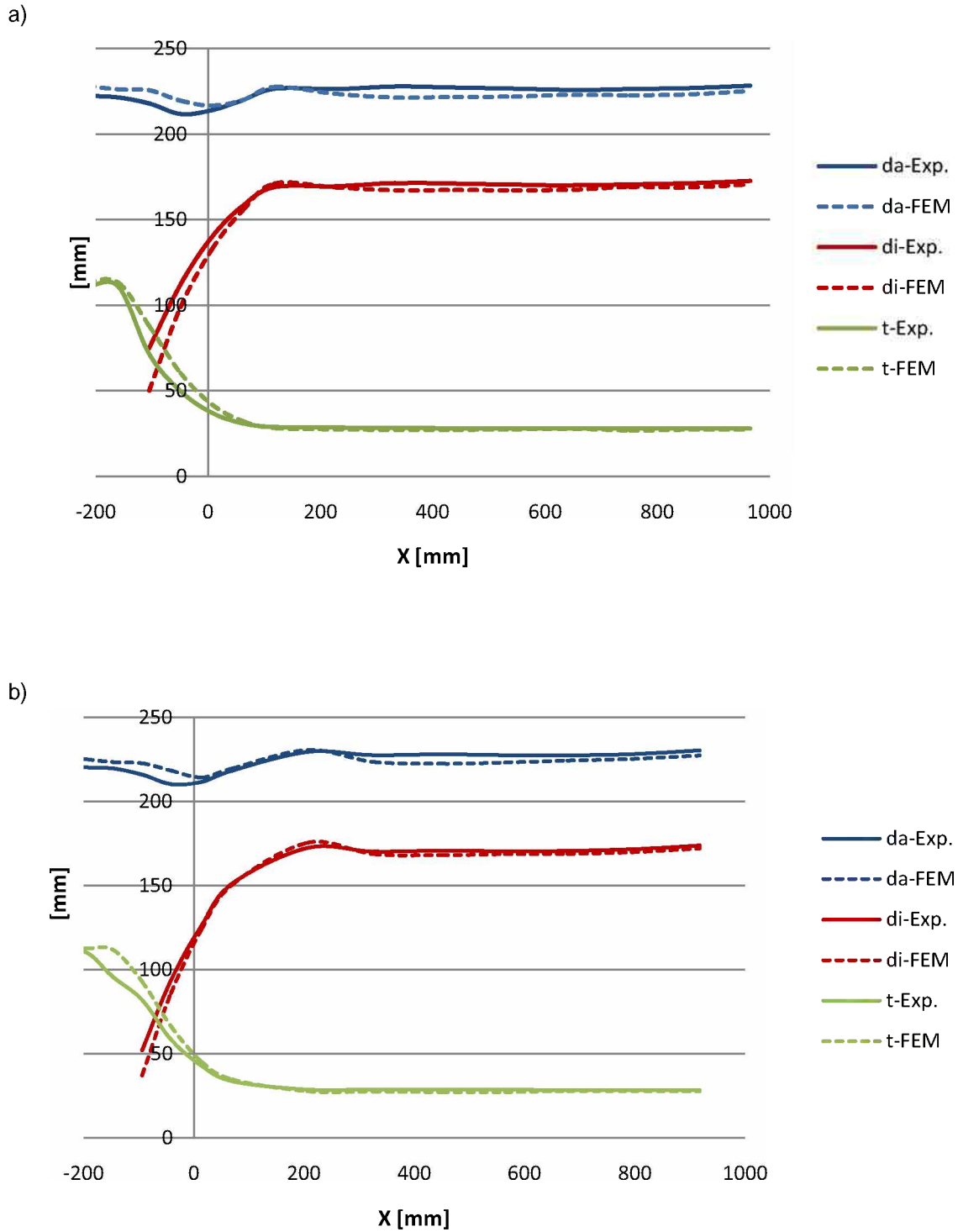


Figure 5.12: Comparison of the geometry behavior between the FEM and experiment in case of neutral type: (a) 1st series, No. 1-3, (b) 2nd series, No. 2-5.

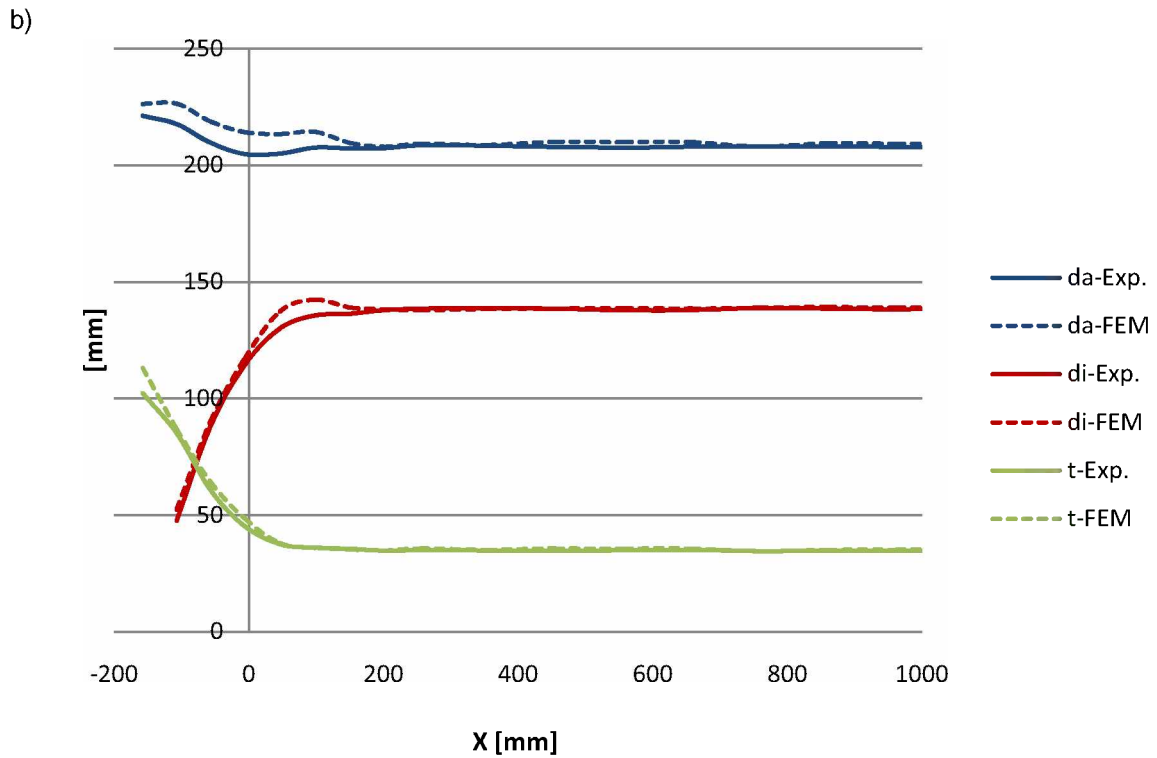
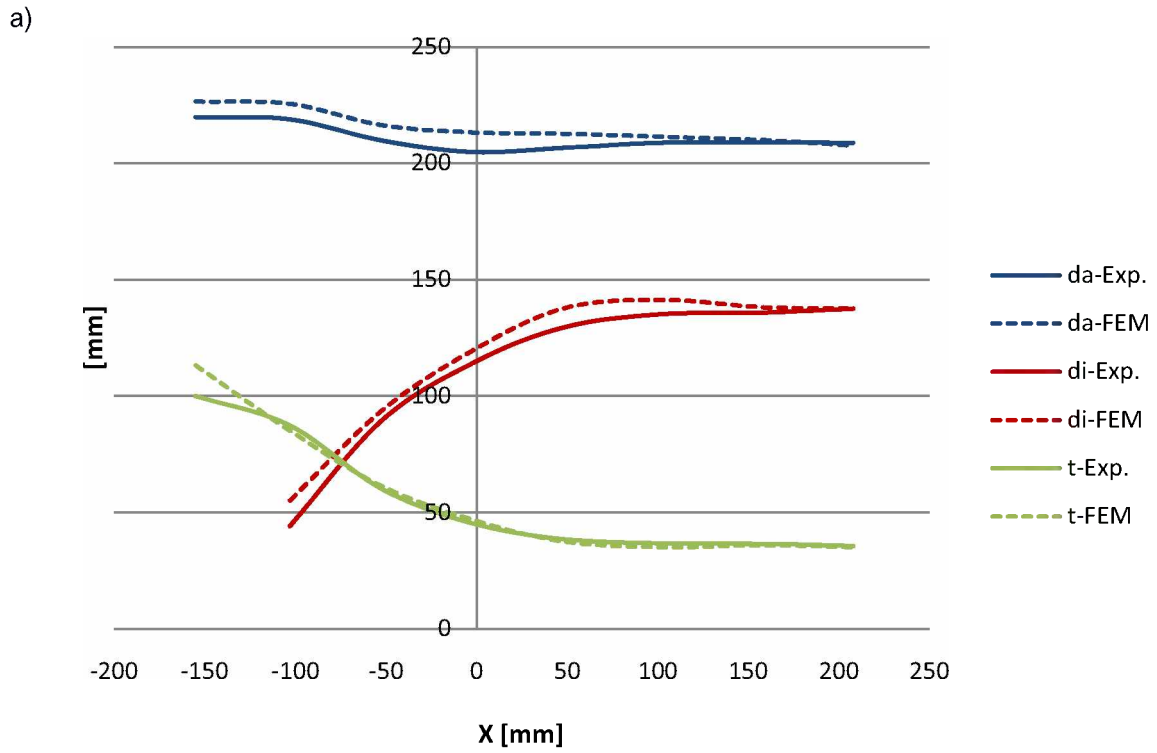


Figure 5.13: Comparison of the geometry behavior between the FEM and experiment in case of reduced type: (a) 3rd series, No. 3-4, (b) 4th series, No. 4-4.

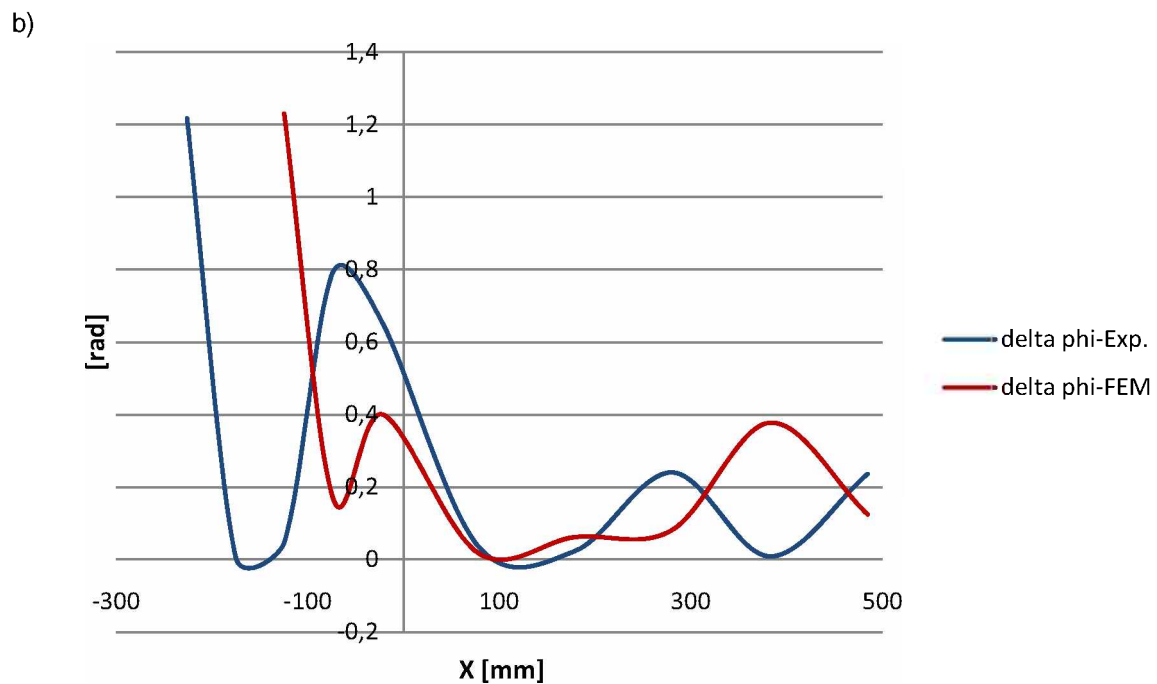
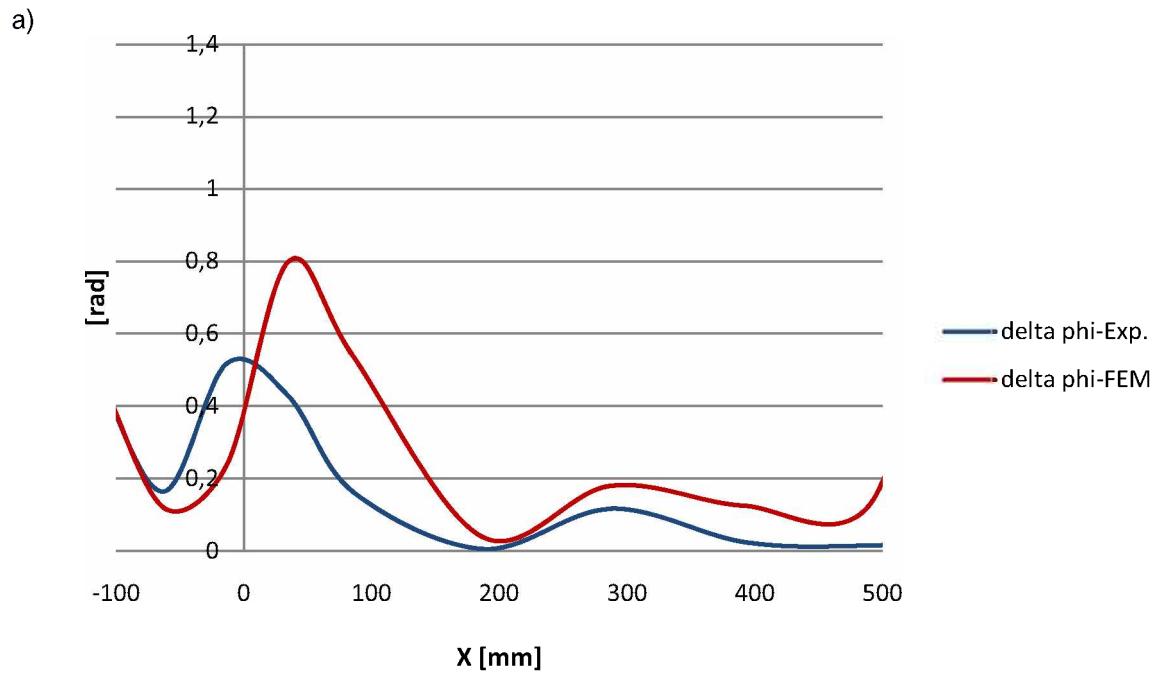


Figure 5.14: Comparison of the delta phi between the FEM and experiment: (a) neutral type, 2nd series, No. 2-3, (b) reduced type, 4th series, No. 4-6.

5.5.2 Model Validation According to the Twisting and the Stretching

In order to optimize the accordance of the numerical results with the experiments regarding the twisting and stretching, various friction models of the roll surface were employed. In this investigation, for the neutral and the reduced type of the rotary piercing separate models were used.

Figure 5.15 compares the varying friction models with respect to the twist of the billet along the x-axis in case of the neutral type. It can be seen that the green curve using a viscoplastic friction model (the details of modes are summarized in Table 12) is more acceptable and it behaves similar in term of trends and magnitude but exact similarity requires new aspects in the application of friction models.

Figure 5.16 shows the same comparison, however based on the reduced type of rotary piercing process. Three different friction models are employed and the details about these models are listed in Table 12. The violet curve based on the Tresca law as global definition indicates a total different behavior. The red curve represents a good coincidence in the rolling gap but it twists less when the material leaves the rolling gap. The green curve shows a good agreement between the calculated billet and the experiment. Both the experiment results and the FEM-calculations depict the twisting in the range of 0.4 to 0.5 when the material loses its contact with the tools.

Figure 5.17 illustrates the comparison between the stretching in the experiment with FEM predictions with respect to the different friction models in case of the neutral type. It can be seen that the different models indicate the same prediction about the strain of the groove along the x-axis. The agreement between the FEM calculation and the experiment is quite good and it behaves exactly in the forming zone. The cumulative error depends on the depth of the hollows, which is a result of the chosen datum point, i.e. the tip of the plug [29].

Based on the reduced type of rotary piercing, the comparisons are illustrated in Figure 5.18. The same statement as with the neutral type can be stated.

Further assumptions will be developed using a friction model that depends on the normal pressure.

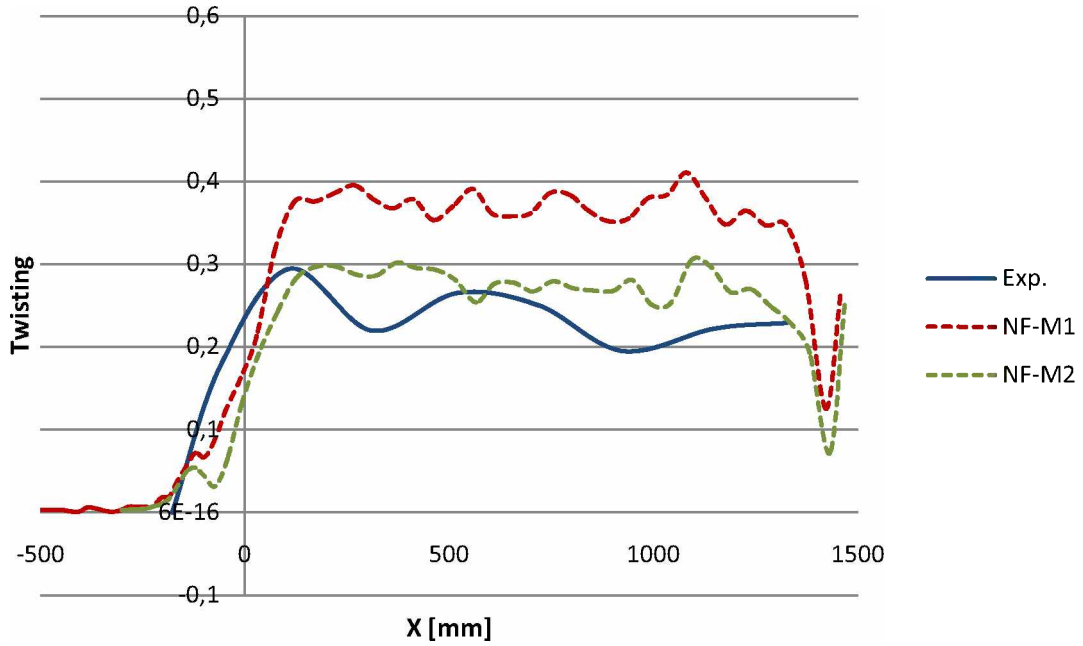


Figure 5.15: Comparison of the twisting along the rolling direction between the experiment and FEM applying different friction models, neutral type No. NF-2.

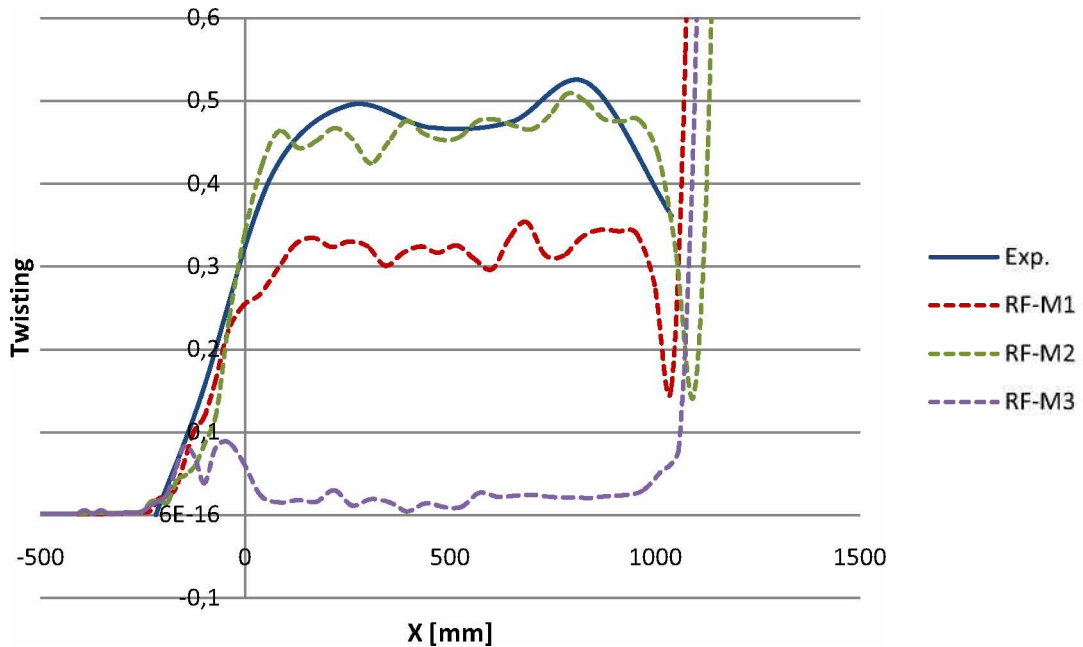


Figure 5.16: Comparison of the twisting along the rolling direction between the experiment and FEM applying different friction models, reduced type No. RF-3.

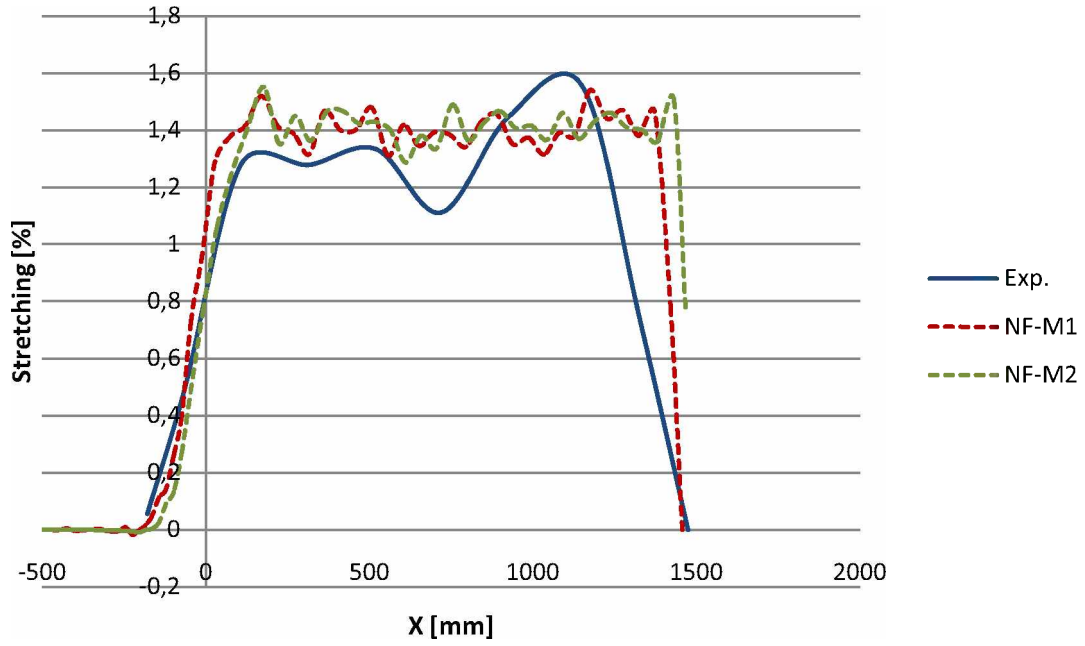


Figure 5.17: Comparison of the stretching between the experiment and FEM applying different friction models, neutral type No. NF-2

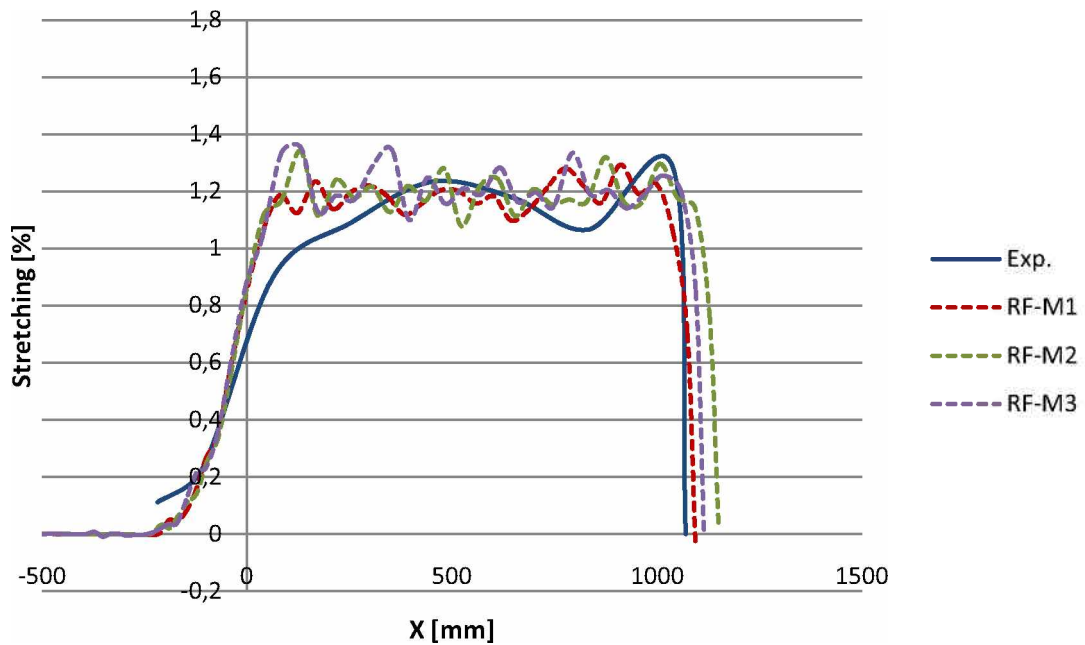


Figure 5.18: Comparison of the stretching between the experiment and FEM applying different friction models, reduced type No. RF-3.

6. Conclusions

The main aim of this study was the prediction of the tube's geometry during the piercing process. A three-dimensional numerical model of the piercing process in a skew rolling mill using the implicit commercial code Forge2007 was developed. A comprehensive experimental program for both neutral and reduced type of piercing process was carried out at Voestalpine-Tubulars GmbH & Co KG in Kindberg, in order to compare the FEM predictions with experimental determinations.

Based on the experimental results, the effect of the feed angle and the plug advance on the geometry behavior was studied. It was found that as the feed angle increases, the average outer diameter increases while the average inner diameter and the wall thickness changed negligibly. In addition, it had been observed that the average outer diameter decreases when the plug advance increases. The effect of plug advance on the average inner diameter and wall thickness is more remarkable at the beginning of the hollow formation. Furthermore, the magnitude of twisting along the billet increases as the feed angle increases and the minimum roll gap and the distance between the Diescher Discs increases.

Based on the FEM-calculation, the effect of the feed angle and the plug advance on the roll force, the mandrel force, roll torque and the Diescher Discs force was studied. It was found that as the feed angle increases, the mandrel force increases while the roll force and the roll torque increase slightly. The variation in the Diescher Discs force with the feed angle is not notable. Furthermore, the roll force and the roll torque decrease with the plug advance while the mandrel force increases slightly. The effect of plug advance on the Diescher Discs is insignificant.

The results showed that the model used for the simulation is able to predict the average outer diameter, the average inner diameter and the wall thickness very well. The delta phi ($\Delta\varphi$) can be calculated well in the term of tendency. The accuracy of the calculated delta phi ($\Delta\varphi$) could be improved by considering the peripheral velocity of the plug and the friction condition on the plug surface.

Friction models were utilized to improve the calculated twisting and stretching along the billet. It was found that the viscoplastic type law is more flexible to obtain the accurate results. Further assumption will be developed using a friction model that depends on the normal pressure.

7. List of Figures

Figure 1.1: Process chain for the production of seamless tubes.	3
Figure 2.1: The rotary tube piercing process: (a) side view, (b) front view, (c) 3D overview, (d) plan view.	4
Figure 2.2: Definition of the geometry parameters associated with the ovality and eccentricity.	5
Figure 2.3: Effect of feed angle (a), minimum roll gap (b), plug advance (c) and maximum plug diameter (d) on roll force and mandrel force [7].	8
Figure 2.4: Maximum principal stress distribution in the transversal cross section of the billet at coordinate $x=-150$ mm according to the coordinate system as shown in Figure 2-1 with feed angle equal to 9°	9
Figure 2.5: Maximum principal stress distribution in the transversal cross section of the billet according to the coordinate system as shown in Figure 2-1 with feed angle equal to 9° and plug advance equal to 125 mm.	10
Figure 2.6: 1th principal stress distribution in the transversal cross section of the billet at coordinate $x=-150$ mm according to the coordinate system as shown in Figure 2-1 with feed angle equal to 13°	11
Figure 2.7: Shear stress distribution in the billet cross section [9].	11
Figure 2.8: 1th principal stress distribution in the transversal cross section of the billet near to the plug position (at coordinate $x=-100$ mm according to the coordinate system as shown in Figure 2-1) with feed angle equal to 9°	12
Figure 2.9: Schematic illustration of plug advance: (a) right, (b) behind, (c) ahead of the central cavity [10].	12
Figure 2.10: Damage evolution according to Le Maitre [15].	16
Figure 2.11: (a) Dragging velocity components at the interface between the roll and material, (b) Definition of the contact line in the transversal cross section [16].	17
Figure 2.12: The cone-type piercing mill [17].	18
Figure 2.13: Effect of feed and cross angle and piercing ratio on the number of billet rotations [11]. .	19
Figure 2.14: Schematic illustration of the deformation zone, which is hatched by the thin line [18]. ...	22
Figure 2.15: Effect of feed angle and maximum plug diameter on the equivalent strain distribution: (a) 9° , 33 mm, (b) 6° , 33 mm (c) 12° , 33 mm (d) 9° , 25 mm [7].	23
Figure 2.16: Strain rate distribution in the rotary piercing process with feed angle equal to 9° , (a) on the exterior tube surface, (b) cut plan with normal vector $\{010\}$, (c) cut plan with normal vector $\{001\}$	24
Figure 2.17: Strain rate distribution in the rotary piercing process with feed angle equal to 13° , (a) on the exterior tube surface, (b) cut plan with normal vector $\{010\}$, (c) cut plan with normal vector $\{001\}$	25
Figure 2.18: Schematic illustration of shear deformation: (a) round billet with marker, (b) circumferential shear deformation, (c) shear deformation due to surface twist [11].	26
Figure 2.19: Definition of transport angle related to the circumferential shear deformation [11].	27

Figure 2.20: Effect of feed, cross angle and piercing ratio on the circumferential shear deformation [11].	28
Figure 2.21: Definition of the transport angle related to the shear deformation due to surface twist [11].	29
Figure 2.22: Effect of feed, cross angle and piercing ratio on the shear deformation due to surface twist [11].	30
Figure 3.1: Definition of normal vector [22].	34
Figure 4.1: Cylindrical billet to be analyzed for the validation of the FEM model.	38
Figure 4.2: Twist and stretch of the groove.	39
Figure 4.3: Cuttings and measurement of the contour.	39
Figure 4.4: Definition of major and minor axis (a) and delta phi (b).	40
Figure 4.5: (a) Roll geometry, (b) Different areas of surface roughness.	41
Figure 4.6: Diescher Discs geometry.	42
Figure 4.7: Plug geometry: (a) maximum plug diameter, 130 mm, (b) maximum plug diameter, 158 mm.	42
Figure 4.8: 3D view of the FEM model of the rotary piercing process.	44
Figure 4.9: Sensors-set up in the billet.	46
Figure 4.10: Finite element mesh: (a) 1th series, (b) 2th series, (c) 3th and 4th series.	47
Figure 4.11: Definition of friction domains on the roll surface: (1) viscoplastic friction law with $\alpha f = 1$, (2) viscoplastic friction law with $\alpha f = 0.7$, (3) viscoplastic friction law with $\alpha f = 0.7$.	49
Figure 4.12: Friction domains on the roll surface in RF-M1.	51
Figure 5.1: Effect of feed angle on the average outer diameter: (a) neutral type, comparison between experiments No. 1-4, 1-5, 1-6, (b) reduced type, comparison between experiments No. 4-4, 4-5, 4-6.	54
Figure 5.2: Effect of feed angle on the average inner diameter: (a) neutral type, comparison between experiments No. 1-1, 1-2, 1-3, (b) reduced type comparison between experiments No. 4-1, 4-2, 4-3.	55
Figure 5.3: Effect of feed angle on the wall thickness: (a) neutral type, comparison between experiments No. 1-1, 1-2, 1-3, (b) reduced type comparison between experiments No. 4-1, 4-2, 4-3.	56
Figure 5.4: Effect of feed angle on the twisting along the rolling direction: (a) neutral type, comparison between experiments No. 1-1, 1-2, 1-3, (b) reduced type, comparison between experiments No. 3-4, 3-5, 3-6.	57
Figure 5.5: Effect of plug advance on the average outer diameter: (a) neutral type, comparison between experiments No. 2-1, 2-4, (b) reduced type, comparison between experiments No. 4-2, 4-5.	59
Figure 5.6: Effect of plug advance on the average inner diameter: (a) neutral type, comparison between experiments No. 1-3, 1-5 (b) reduced type, comparison between experiments No. 4-2, 4-5.	60

Figure 5.7: Effect of plug advance on the wall thickness: (a) neutral type, comparison between experiments No. 1-3, 1-5 (b) reduced type, comparison between experiments No. 4-2, 4-5. 61

Figure 5.8: Effect of plug advance on the twisting along the rolling direction, reduced type, comparison between experiments No. 4-1, 4-4. 62

Figure 5.9: Effect of the minimum roll gap and the distance between the Diescher discs on the twisting along the rolling direction, neutral type, comparison between experiments No. 2-3, 2-5. 62

Figure 5.10: Effect of feed angle on the roll force (a), mandrel force (b), roll torque (c) and the Diescher Discs force for the neutral (N) and reduced (R) type. 63

Figure 5.11: Effect of plug advance on the roll force (a), mandrel force (b), roll torque (c) and the Diescher Discs force for the neutral (N) and reduced (R) type. 64

Figure 5.12: Comparison of the geometry behavior between the FEM and experiment in case of neutral type: (a) 1st series, No. 1-3, (b) 2nd series, No. 2-5. 66

Figure 5.13: Comparison of the geometry behavior between the FEM and experiment in case of reduced type: (a) 3rd series, No. 3-4, (b) 4th series, No. 4-4. 67

Figure 5.14: Comparison of the delta phi between the FEM and experiment: (a) neutral type, 2nd series, No. 2-3, (b) reduced type, 4th series, No. 4-6. 68

Figure 5.15: Comparison of the twisting along the rolling direction between the experiment and FEM applying different friction models, neutral type No. NF-2. 70

Figure 5.16: Comparison of the twisting along the rolling direction between the experiment and FEM applying different friction models, reduced type No. RF-3. 70

Figure 5.17: Comparison of the stretching between the experiment and FEM applying different friction models, neutral type No. NF-2. 71

Figure 5.18: Comparison of the stretching between the experiment and FEM applying different friction models, reduced type No. RF-3. 71

8. List of Tables

Table 1: Cause of eccentricity of tube in Mannesmann piercing [4].	6
Table 2: Effect of increasing feed angle, minimum roll gap, plug advance and maximum plug diameter on roll force and mandrel force.	9
Table 3: Equivalent strain to fracture and average stress triaxiality for typical upsetting tests [12].	13
Table 4: Damage mechanism depending on the average stress triaxiality [12].	14
Table 5: Investigation on the simulation of rotary piercing process.	37
Table 6: Experimental conditions.	43
Table 7: Mesh properties of each simulation's series.	47
Table 8: Material properties and Hensel-Spittel's equation coefficients.	48
Table 9: Definition of friction domains on the roll surface.	50
Table 10: Material properties and Hensel-Spittel's equation coefficients.	50
Table 11: Experimental condition for the validation of the FEM model according to the applied friction models.	51
Table 12: Definition of the new friction models.	52

9. References

- [1] E. Doremus and J. Oudin: "Kinematic element modeling of horizontal two-roll piercing", *Journal of Materials Processing Technology*, 42, 1994, pp. 293-310.
- [2] E. Ermann: "The influence of the processing parameters on the performance of the two-roll piercing operation", *Journal of Mechanical Working Technology*, 15, 1987, pp. 167-79.
- [3] H. Yoshimura and Y. Mihara: "Simplified 3-D FE simulation of rotary piercing controlling rotation of plug", *Simulation of Materials Processing*, 2001, pp. 577-582.
- [4] Y. Mihara et al.: "Study on the Accuracy of Wall Thickness in Seamless Tube Rolling Process", *Nippon Kokan Technical Report, Overseas No.44*, 1985, pp. 30-40.
- [5] D. A. Berazategui et al.: "On the modeling of complex 3D bulk metal forming processes via the pseudo-concentrations technique. Application to the simulation of the Mannesmann piercing process", *Int. J. Numer. Meth. Engng*, 65, 2006, pp. 1113-1144.
- [6] A. Al-Dahwi and T. Blazynski: "Inhomogeneity of flow, force parameters and pass geometry in rotary cone-roll tube", *Mat.-wiss. und Werkstofftech*, 23, 1992, pp. 29-38.
- [7] K. Komori: "Simulation of Mannesmann piercing process by the three-dimensional rigid-plastic finite-element method", *International Journal of Mechanical Science*, 47, 2005, pp. 1838-1853.
- [8] J. Pietsch and P. Thieven: "FEM simulation of the rotary tube piercing process", *MPT International*, 2, 2003, pp. 52-60.
- [9] T. Leisten: "Auswirkungen von Umformparametern auf die productgeometrie und die Prozessbedingungen beim Schräglochwalzen von Stählen", *PHD thesis, Technische Universität Bergakademie Freiberg, Germany*, 2001.
- [10] E. Ceretti, C. Giardini and A. Attanasio: "Rotary tube piercing study by FEM analysis-3D simulations and experimental results", *Tube and Pipe Technology*, 2004, pp. 55-58.
- [11] C. Hayashi and T. Yamakawa: "Influence of feed and cross angle on rotary forging effects and redundant shear deformations in rotary piercing process", *ISIJ international*, 37, 1997, pp. 146-52.
- [12] S. Chiluveru: "Computational modeling of crack initiation in cross-rolling piercing", *Master thesis, Massachusetts Institute of Technology, USA*, 2007.
- [13] S.Z. Li et al.: "FE simulation of centre crack occurrence in tube rounds during two-roll rotary rolling process". *Acta Metall. Sin. (Engl. Lett.)*, 20, 2007, pp. 225-234.
- [14] S. Fanini, A. Ghiotti and S. Bruschi: "Prediction of the fracture due to Mannesmann effect in tube piercing", *MATERIALS PROCESSING AND DESIGN; Modeling, Simulation and Applications, NUMIFORM' 07, Proceedings of the 9th International Conference on Numerical Methods in Industrial Forming Processes*, 908, Porto, Portugal, June 2007, pp. 1407-1412.
- [15] J. LeMaitre: "A course on damage mechanics", *Springer, New York*, 2nd edition, 1996, pp.1-152.
- [16] J.C. Gelin, E. Doremus, P. Hrycaj and J. Oudin: "Kinematic and thermal analysis of hot piercing rolling of seamless tubes", *Ann. CIRP*, 33, 1984, pp. 1155-159.
- [17] C. Hayashi and T. Yamakawa: "Influences of piercing ratio, expansion ratio, feed, cross and skew angles on available piercing size range in rotary piercing process", *ISIJ International*, 38, 1998, pp. 1255-1261.
- [18] L.N. Pussegoda, R. Brbosa, S. Yue, J. Jonas and J. Hunt: "Laboratory simulation of seamless-tube rolling", *Journal of Materials Processing Technology*, 25, 1991, pp. 69-90.
- [19] Z. Pater, J. Kazanecki and J. Bartnicki: "Three dimensional thermo-mechanical simulation of the tube forming process in Diescher's mill", *Journal of Material Processing Technology*, 177 (1-3), 2006, pp.167-170.
- [20] M. Rappetz, M. Bellet and M. Deville: "Numerical modeling in materials science and engineering", *Springer Series in Computational Mathematic*, 2002.
- [21] S. Kobayashi, S. Oh and T. Altan: "Metal forming and finite-element method", *Oxford University Press, New York*, 1989.
- [22] B. Rey: "Methode Multigrilles Pour Les Grandes Deformations Et Simulation Numerique Du Procede De Roulage", *PHD thesis, Ecole Des Mines De Paris*, April 2007.
- [23] S. Urbanski and J. Kazanecki: "Assessment of the strain distribution in the rotary piercing process by the finite element method", *Journal of Materials Processing Technology*, 45, 1994, pp. 335-340.
- [24] K. Mori et al.: "Simplified three-dimensional simulation of rotary piercing of seamless pipe by rigid-plastic finite-element method", *Journal of Materials Processing Technology*, 80-81, 1998, pp. 700-706.

- [25] G. Capoferri et al.: "FEM analysis of rotary tube piercing process", Tube & Pipe Technology, May/June 2002, pp. 55-58.
- [26] P. Zbigniew and J. Kazanecki: "Thermo-mechanical analysis of piercing plug loads in the skew rolling process of thick-walled tube shell", Metallurgy and Foundry Engineering, 32, 2006, pp. 31-39.
- [27] M. Reggio et al.: "Computational analysis of the process for manufacturing seamless tubes", Applied Thermal Engineering, 22, 2002, pp. 459-470.
- [28] H. Schoß and G. Lehmann: "Axialdruck-Schrägwalzlochen Experiment und Simulation" TU Bergakademie Freiberg, Germany.
- [29] R. Pschera, J. Klarner und C. Sommitsch: " Finite-Elemente-Modellierung des Schrägwalzens", BHM, 152.Jg. Heft 7, 2007, pp. 205-210.
- [30] N. Nakahashi, et al.: "Development of rolling technique for stainless steel seamless pipe with plug mill process", Iron and Steelmaker, 30, 2003, pp. 37-42.

10. Appendix

In this appendix all data related to experimental and FEM calculations and their comparison are given.

Table A 1: Experimental data according to the geometry for 1st series, No.1-1.

x	a _i	b _i	a _o	b _o
-310,5	0,0	0,0	114,3	113,0
-254,1	0,0	0,0	112,9	111,2
-199,8	0,0	0,0	111,8	108,8
-139,4	0,0	0,0	114,2	106,9
-82,0	43,6	41,1	112,5	103,1
-24,6	62,3	57,4	110,3	100,7
26,8	76,1	67,8	112,1	102,1
79,1	86,6	74,1	116,8	103,3
131,5	91,1	77,6	119,8	105,9
228,9	87,9	80,9	115,6	109,1
341,3	85,8	84,0	113,8	111,8
434,6	86,3	84,2	113,7	111,9
540,0	87,3	84,4	114,4	112,1

Table A 2: FEM calculations according to the geometry for 1st series, No.1-1.

x	a _i	b _i	a _o	b _o
-310,5	0,0	0,0	115,7	115,6
-254,1	0,0	0,0	115,3	113,8
-199,8	0,0	0,0	114,5	111,5
-139,4	0,0	0,0	111,5	111,5
-82,0	36,6	35,2	120,1	104,5
-24,6	61,3	55,4	118,9	99,7
26,8	76,5	67,0	116,1	100,3
79,1	89,4	73,6	120,6	102,0
131,5	98,2	75,9	125,1	103,5
228,9	88,7	80,3	116,4	107,1
341,3	84,2	83,4	111,8	110,3
434,6	84,4	83,4	111,9	110,7
540,0	85,3	84,0	111,9	111,6

Table A 3: Experimental data according to the geometry for 1st series, No.1-3.

x	a _i	b _i	a _o	b _o
-327,0	0,0	0,0	114,8	113,1
-272,5	0,0	0,0	113,4	111,8
-216,0	0,0	0,0	113,4	109,3
-159,5	0,0	0,0	114,6	107,0
-105,0	38,6	36,5	114,2	103,9
-49,5	58,2	54,0	111,0	101,0
7,0	73,5	66,7	112,0	102,1
62,5	85,5	73,3	117,1	103,3
118,0	92,2	77,4	121,2	105,8
225,5	88,7	80,9	116,9	109,6
333,0	86,7	84,7	114,9	113,0
438,5	86,1	85,0	114,5	112,8
543,0	86,0	84,5	114,1	112,5
650,5	85,3	84,8	113,2	112,6
752,0	85,5	85,1	113,6	112,7
858,5	86,3	85,0	114,2	112,7
965,0	86,8	85,9	114,6	113,7

Table A 4: FEM calculations according to the geometry for 1st series, No.1-3.

x	a _i	b _i	a _o	b _o
-327,0	0,0	0,0	116,1	116,0
-272,5	0,0	0,0	116,6	115,3
-216,0	0,0	0,0	115,5	112,8
-159,5	0,0	0,0	116,1	110,1
-105,0	25,1	25,0	119,5	106,6
-49,5	51,2	47,6	117,5	102,6
7,0	69,7	63,3	117,4	100,0
62,5	83,9	72,3	118,8	101,7
118,0	96,8	75,7	125,4	103,3
225,5	88,6	80,4	116,1	107,6
333,0	84,6	82,6	111,5	109,9
438,5	84,2	83,2	110,9	110,9
543,0	84,2	83,0	111,3	110,6
650,5	84,1	83,3	111,6	111,3
752,0	85,4	83,8	112,1	110,5
858,5	84,9	84,0	112,5	110,8
965,0	86,0	84,6	112,9	112,3

Table A 5: Experimental data according to the geometry for 1st series, No.1-4.

x	a _i	b _i	a _o	b _o
-268,7	0,0	0,0	113,9	110,9
-211,5	0,0	0,0	113,4	108,7
-158,3	17,1	14,9	119,6	98,6
-100,1	40,8	38,9	111,0	101,9
-55,0	56,7	52,4	109,8	101,2
-5,8	71,1	64,4	111,5	103,5
43,4	82,5	73,0	116,3	105,3
95,6	96,0	80,6	124,9	108,9
153,7	96,0	80,7	124,7	109,0
206,9	92,5	81,6	121,5	110,7
259,1	89,4	83,5	118,0	112,9
362,3	88,8	85,7	118,2	114,1
466,4	90,0	84,3	118,7	113,7
570,6	89,9	85,0	118,9	113,9
671,8	89,6	85,3	118,9	113,5
774,0	89,7	84,8	118,2	113,4
877,1	89,6	84,5	118,1	113,1
978,3	87,6	85,3	116,6	113,6
1080,5	86,8	86,3	115,4	114,4
1185,7	87,4	86,0	115,8	114,7

Table A 6: FEM calculations according to the geometry for 1st series, No.1-4.

x	a _i	b _i	a _o	b _o
-268,7	0,0	0,0	117,0	115,1
-211,5	0,0	0,0	116,7	112,2
-158,3	0,0	0,0	117,3	109,4
-100,1	0,0	0,0	120,0	105,5
-55,0	37,1	36,5	118,5	101,7
-5,8	56,3	53,7	118,8	99,0
43,4	71,7	65,6	121,2	99,1
95,6	86,8	73,1	121,4	102,6
153,7	102,2	76,2	130,4	104,5
206,9	99,2	78,3	126,4	106,1
259,1	90,8	80,7	118,1	108,7
362,3	84,8	84,1	114,1	111,0
466,4	86,0	83,5	113,5	111,9
570,6	85,0	84,0	114,9	110,9
671,8	84,9	83,7	113,0	111,9
774,0	85,1	83,8	113,1	111,8
877,1	86,0	84,0	113,6	112,5
978,3	85,2	84,3	113,6	112,8
1080,5	86,0	83,8	114,2	113,0
1185,7	86,4	84,8	114,5	113,4

Table A 7: Experimental data according to the geometry for 1st series, No.1-5.

x	a _i	b _i	a _o	b _o
-182,6	0,0	0,0	112,8	109,8
-128,4	0,0	0,0	113,4	107,4
-73,2	19,8	15,4	113,8	104,0
-17,9	41,5	39,5	111,6	100,8
36,3	60,3	55,8	110,9	99,9
90,5	75,2	67,4	113,7	102,5
145,7	88,5	73,9	120,2	104,3
200,9	94,9	77,9	124,5	106,6
307,1	90,5	80,6	119,5	109,7
384,3	87,9	83,9	116,8	112,9
491,5	87,5	84,8	116,7	113,7
599,7	87,1	85,6	116,9	114,5
708,9	87,8	85,9	116,6	114,7
827,2	88,4	84,7	117,4	113,5
938,4	88,3	84,2	117,5	113,1
1062,6	87,3	85,6	115,9	114,5
1167,8	87,0	86,7	115,8	115,2
1299,0	89,4	87,7	117,4	116,5

Table A 8: FEM calculations according to the geometry for 1st series, No.1-5.

x	a _i	b _i	a _o	b _o
-182,6	0,0	0,0	115,4	110,3
-128,4	0,0	0,0	117,5	107,4
-73,2	28,4	28,3	120,1	103,1
-17,9	53,1	49,9	123,3	97,1
36,3	70,5	64,1	120,9	98,6
90,5	85,7	72,5	119,1	102,6
145,7	101,7	75,7	111,9	111,9
200,9	100,1	78,2	125,6	105,9
307,1	88,7	81,4	116,1	109,4
384,3	85,9	83,2	113,7	110,9
491,5	84,6	83,9	112,1	111,9
599,7	84,7	84,0	112,2	112,2
708,9	84,9	84,3	113,1	110,4
827,2	85,1	84,0	112,8	112,4
938,4	86,1	84,7	113,0	113,0
1062,6	86,4	84,6	114,9	112,6
1167,8	86,8	86,1	114,6	114,2
1299,0	90,0	88,9	117,2	116,5

Table A 9: Experimental data according to the geometry for 1st series, No.1-6.

x	a _i	b _i	a _o	b _o
-357,8	0,0	0,0	115,3	113,6
-305,2	0,0	0,0	113,1	112,8
-249,6	0,0	0,0	112,2	110,9
-195,1	0,0	0,0	112,1	108,3
-146,5	16,9	11,9	113,4	106,3
-93,9	27,1	24,9	113,2	103,1
-41,3	48,4	45,2	110,5	100,1
14,3	66,0	60,5	111,4	100,6
69,9	81,1	70,5	116,1	102,8
206,5	94,3	78,8	122,3	107,7
326,1	86,7	83,5	115,5	112,1
449,6	86,2	84,6	115,2	112,9
564,2	85,9	84,5	115,1	112,4
677,8	86,1	84,5	114,5	112,9
794,4	87,1	84,5	115,6	112,6
918,0	88,5	85,4	116,5	113,9

Table A 10: FEM calculations according to the geometry for 1st series, No.1-6.

x	a _i	b _i	a _o	b _o
-357,8	0,0	0,0	116,1	116,0
-305,2	0,0	0,0	116,4	115,2
-249,6	0,0	0,0	113,8	113,8
-195,1	0,0	0,0	114,7	110,4
-146,5	0,0	0,0	115,3	108,3
-93,9	18,6	18,5	119,0	104,3
-41,3	44,6	41,5	118,5	100,7
14,3	65,3	58,9	115,9	99,1
69,9	80,9	70,0	119,4	101,2
206,5	98,0	78,5	125,9	105,5
326,1	86,1	82,6	113,7	109,9
449,6	84,1	84,1	111,3	111,3
564,2	84,7	84,0	111,6	111,6
677,8	85,2	83,8	112,5	111,9
794,4	85,8	84,0	112,9	112,5
918,0	86,5	85,6	113,9	113,5

Table A 11: Experimental data according to the geometry for 2nd series, No.2-1.

x	a _i	b _i	a _o	b _o
-209,0	0,0	0,0	113,8	111,9
-162,0	0,0	0,0	114,0	109,5
-112,0	27,1	26,3	114,6	106,3
-60,0	48,0	46,2	110,4	101,9
-14,5	62,7	58,7	109,0	100,5
34,0	74,3	68,4	110,6	101,7
85,0	85,1	73,9	115,8	103,4
186,0	89,1	78,8	117,6	107,4
286,5	86,2	82,8	114,5	111,3
387,5	85,5	83,6	113,7	111,5
490,0	85,7	82,9	113,8	111,1
590,0	85,2	83,1	112,8	110,8
691,0	85,5	83,2	113,2	110,5
789,0	87,2	82,7	114,5	109,7
889,0	87,1	83,0	114,2	110,3
987,0	85,8	85,3	113,6	113,1

Table A 12: FEM calculations according to the geometry for 2nd series, No.2-1.

x	a _i	b _i	a _o	b _o
-209,0	0,0	0,0	116,1	113,1
-162,0	0,0	0,0	116,7	110,7
-112,0	21,3	21,2	112,1	112,1
-60,0	45,1	43,3	117,5	103,9
-14,5	61,8	57,8	118,6	100,3
34,0	75,5	68,4	117,9	101,3
85,0	88,7	73,9	119,9	103,2
186,0	83,1	83,1	122,2	104,8
286,5	84,8	81,8	110,4	110,4
387,5	83,3	82,5	111,3	110,8
490,0	83,7	83,0	111,5	111,1
590,0	84,7	82,9	112,2	111,5
691,0	84,8	83,7	113,0	112,3
789,0	84,9	83,7	113,1	112,3
889,0	85,2	83,9	113,4	111,1
987,0	86,0	84,9	113,6	113,1

Table A 13: Experimental data according to the geometry for 2nd series, No.2-2.

x	a _i	b _i	a _o	b _o
-211,2	0,0	0,0	113,0	110,0
-161,7	0,0	0,0	112,9	109,5
-114,3	14,6	13,6	119,2	99,8
-62,8	39,1	36,9	112,8	103,0
-13,4	57,5	53,4	109,9	100,1
35,1	70,9	65,0	110,0	101,0
85,5	82,9	72,6	114,6	102,3
187,0	90,0	78,8	117,7	106,8
287,4	85,7	83,0	113,1	110,5
393,9	85,9	83,7	113,3	111,5
494,3	86,6	83,2	113,7	110,3
594,8	86,7	82,9	114,1	110,1
694,2	86,8	82,4	113,7	110,0
793,7	87,5	81,9	114,8	109,2
894,1	87,1	82,8	114,1	109,9
994,6	85,6	83,9	112,8	111,6
1100,0	86,0	85,1	113,5	112,5

Table A 14: FEM calculations according to the geometry for 2nd series, No.2-2.

x	a _i	b _i	a _o	b _o
-211,2	0,0	0,0	116,1	110,9
-161,7	0,0	0,0	118,2	108,8
-114,3	33,0	31,7	114,9	105,5
-62,8	56,0	51,1	119,5	101,5
-13,4	71,0	63,9	115,7	100,3
35,1	75,5	75,5	117,9	101,5
85,5	94,7	74,8	109,6	109,6
187,0	82,6	82,6	110,3	110,3
287,4	84,3	81,8	110,5	109,4
393,9	83,2	82,2	110,5	108,9
494,3	83,1	82,7	111,3	107,5
594,8	83,0	83,0	110,6	110,4
694,2	83,6	83,1	111,0	109,8
793,7	83,7	83,2	111,6	111,1
894,1	84,8	83,6	114,1	109,9
994,6	84,4	83,7	113,3	110,3
1100,0	85,2	84,7	112,7	112,4

Table A 15: Experimental data according to the geometry for 2nd series, No.2-3.

x	a _i	b _i	a _o	b _o
-105,7	12,9	8,2	115,2	106,7
-54,6	31,5	30,6	110,9	102,5
-8,4	48,6	46,9	108,5	99,9
44,7	64,9	60,8	108,7	100,9
93,9	77,0	70,7	112,2	103,3
195,0	92,2	78,9	121,1	107,4
296,1	87,9	83,4	116,3	111,2
398,3	87,2	85,1	115,3	112,8
499,4	89,6	83,5	117,4	111,8
599,6	89,9	83,7	117,9	111,6
700,7	88,3	83,3	117,8	112,6
800,9	89,5	82,3	118,8	112,5
903,0	89,0	82,9	118,3	111,9
1006,1	88,4	82,9	117,0	112,6
1107,3	87,0	82,5	116,1	112,1
1208,4	86,5	84,3	115,3	112,8
1308,6	85,8	85,1	114,7	113,3

Table A 16: FEM calculations according to the geometry for 2nd series, No.2-3.

x	a _i	b _i	a _o	b _o
-105,7	0,0	0,0	119,8	105,9
-54,6	37,6	36,2	120,5	101,3
-8,4	56,9	52,3	118,2	98,6
44,7	73,0	65,5	105,9	105,9
93,9	87,1	72,4	119,9	102,4
195,0	97,7	77,6	112,2	112,2
296,1	86,9	82,0	112,2	112,2
398,3	85,5	83,1	113,7	111,7
499,4	84,2	83,9	112,6	112,2
599,6	84,5	83,4	112,9	112,1
700,7	84,5	83,5	113,2	110,3
800,9	84,8	83,2	112,6	111,9
903,0	84,6	83,9	112,7	112,7
1006,1	85,3	83,8	113,4	112,5
1107,3	86,1	83,5	114,6	111,3
1208,4	85,2	84,3	114,0	112,1
1308,6	85,7	84,4	114,0	113,3

Table A 17: Experimental data according to the geometry for 2nd series, No.2-4.

x	a _i	b _i	a _o	b _o
-190,8	0,0	0,0	113,7	111,4
-140,4	0,0	0,0	114,0	110,1
-91,1	0,0	0,0	114,0	108,1
-41,7	20,9	19,1	113,2	104,8
8,6	37,4	36,0	110,6	101,2
56,0	57,0	53,5	108,2	99,4
99,8	71,6	66,2	111,0	101,4
198,2	82,7	72,2	114,9	102,5
295,5	94,6	78,2	122,9	105,9
393,9	89,3	80,3	117,3	108,3
494,3	86,3	83,4	114,8	112,0
595,6	85,5	84,5	113,6	113,2
697,5	85,7	84,5	114,8	112,7
799,3	86,7	84,6	114,7	113,2
899,7	87,5	85,1	114,8	113,0
1001,0	87,3	85,3	114,9	113,5
1102,4	86,3	84,9	114,2	113,5

Table A 18: FEM calculations according to the geometry for 2nd series, No.2-4.

x	a _i	b _i	a _o	b _o
-190,8	0,0	0,0	111,7	111,7
-140,4	0,0	0,0	116,4	108,2
-91,1	19,3	18,8	119,5	104,0
-41,7	44,6	41,3	115,7	100,6
8,6	63,5	57,0	115,4	98,5
56,0	77,6	67,4	118,0	100,4
99,8	89,7	73,0	122,0	102,1
198,2	96,3	78,1	121,9	106,0
295,5	87,7	81,2	115,2	109,6
393,9	83,7	83,7	112,1	111,5
494,3	84,3	83,3	111,6	111,6
595,6	84,6	83,5	112,5	111,8
697,5	84,4	83,6	112,2	111,4
799,3	84,1	84,1	112,3	112,0
899,7	84,7	83,8	113,1	110,0
1001,0	85,1	83,8	112,9	112,2
1102,4	84,6	83,6	112,7	111,5

Table A 19: Experimental data according to the geometry for 2nd series, No.2-5.

x	a _i	b _i	a _o	b _o
-210,1	0,0	0,0	114,0	110,1
-160,4	0,0	0,0	114,0	108,1
-102,8	20,9	19,1	113,2	104,8
-65,1	37,4	36,0	110,6	101,2
-11,5	57,0	53,5	108,2	99,4
43,2	71,6	66,2	111,0	101,4
87,8	82,7	72,2	114,9	102,5
184,5	94,6	78,2	122,9	105,9
279,1	89,3	80,3	117,3	108,3
379,8	86,3	83,4	114,8	112,0
484,4	85,5	84,5	113,6	113,2
601,0	85,7	84,5	114,8	112,7
690,2	86,7	84,6	114,7	113,2
785,8	87,5	85,1	114,8	113,0
893,5	87,3	85,3	114,9	113,5
987,1	86,3	84,9	114,2	113,5

Table A 20: FEM calculations according to the geometry for 2nd series, No.2-5.

x	a _i	b _i	a _o	b _o
-210,1	0,0	0,0	114,9	112,2
-160,4	0,0	0,0	115,2	110,2
-102,8	0,0	0,0	117,9	107,2
-65,1	20,3	19,3	117,5	104,6
-11,5	46,5	43,1	116,5	100,0
43,2	66,2	59,8	119,2	98,7
87,8	79,5	68,8	117,5	101,4
184,5	99,9	76,4	126,7	104,4
279,1	88,8	80,4	117,9	107,6
379,8	85,3	82,2	110,8	110,8
484,4	83,9	83,2	111,4	111,4
601,0	83,9	83,2	113,4	109,9
690,2	84,3	82,9	111,8	110,4
785,8	85,1	83,2	114,2	109,7
893,5	84,2	83,6	111,8	111,8
987,1	84,4	83,7	112,1	111,0

Table A 21: Experimental data according to the geometry for 3rd series, No.3-1.

x	a _i	b _i	a _o	b _o
-166,1	17,8	15,6	114,7	107,3
-115,1	42,5	41,3	111,6	104,1
-61,1	56,3	53,6	106,8	100,7
-8,6	65,7	61,3	104,8	99,0
41,4	70,1	64,8	105,7	99,7

Table A 22: FEM calculations according to the geometry for 3rd series, No.3-1.

x	a _i	b _i	a _o	b _o
-166,1	0,0	0,0	119,8	108,6
-115,1	35,0	34,6	122,1	105,6
-61,1	52,6	51,5	116,7	102,1
-8,6	64,6	61,1	113,3	98,9
41,4	75,9	63,8	114,9	98,1

Table A 23: Experimental data according to the geometry for 3rd series, No.3-2.

x	a _i	b _i	a _o	b _o
-166,0	15,6	13,1	113,9	106,8
-114,5	33,7	32,8	114,5	104,3
-62,5	51,9	50,0	108,4	101,4
-13,0	62,2	58,0	105,6	98,5
35,5	69,4	62,8	106,1	98,4
85,0	70,2	64,8	105,8	99,5

Table A 24: FEM calculations according to the geometry for 3rd series, No.3-2.

x	a _i	b _i	a _o	b _o
-166,0	0,0	0,0	117,4	108,6
-114,5	35,4	35,1	122,3	105,7
-62,5	54,3	51,2	114,5	102,2
-13,0	65,9	60,5	120,5	95,9
35,5	76,6	63,3	114,5	97,9
85,0	77,8	64,4	111,2	98,8

Table A 25: Experimental data according to the geometry for 3rd series, No.3-3.

x	a _i	b _i	a _o	b _o
-184,0	16,5	12,9	124,0	96,0
-135,0	26,9	24,9	115,1	105,7
-88,0	47,0	44,7	109,7	102,7
-41,5	58,7	55,5	106,0	99,3
5,0	67,1	61,8	105,0	98,6
53,5	69,4	64,9	105,3	99,6
105,0	68,9	66,3	103,6	101,0

Table A 26: FEM calculations according to the geometry for 3rd series, No.3-3.

x	a _i	b _i	a _o	b _o
-184,0	0,0	0,0	116,8	108,9
-135,0	26,8	26,3	118,3	106,3
-88,0	48,0	43,8	109,1	109,1
-41,5	61,4	56,0	105,0	105,0
5,0	71,7	62,1	120,0	95,0
53,5	68,3	68,3	116,1	95,9
105,0	71,8	66,3	107,3	99,7

Table A 27: Experimental data according to the geometry for 3rd series, No.3-4.

x	a _i	b _i	a _o	b _o
-103,0	22,9	21,3	113,4	105,5
-52,5	45,7	43,7	107,8	102,1
-2,5	58,3	55,7	105,7	99,1
48,0	66,8	62,7	106,3	100,4
102,5	70,3	64,9	107,7	101,2
157,5	68,7	67,1	105,5	103,4
208,0	69,2	68,3	105,0	103,8

Table A 28: FEM calculations according to the geometry for 3rd series, No.3-4.

x	a _i	b _i	a _o	b _o
-103,0	28,1	27,1	121,2	104,9
-52,5	47,9	45,7	116,7	100,3
-2,5	62,1	57,5	116,6	97,5
48,0	75,6	62,7	115,1	98,3
102,5	77,3	64,6	112,1	99,7
157,5	71,3	67,0	109,9	100,3
208,0	69,8	67,9	104,4	103,2

Table A 29: Experimental data according to the geometry for 3rd series, No.3-5.

x	a _i	b _i	a _o	b _o
-156,0	14,3	10,6	113,3	106,2
-96,5	27,5	26,9	112,7	103,2
-38,5	51,3	49,2	106,8	99,6
13,0	62,4	58,7	105,6	98,6
63,0	69,9	63,4	107,3	99,7
115,5	69,6	65,5	106,2	100,9

Table A 30: FEM calculations according to the geometry for 3rd series, No.3-5.

x	a _i	b _i	a _o	b _o
-156,0	0,0	0,0	116,9	108,1
-96,5	30,9	30,1	120,8	103,9
-38,5	52,1	49,8	116,1	100,0
13,0	66,9	59,9	113,1	97,8
63,0	67,6	67,6	114,0	99,0
115,5	75,4	64,9	111,5	98,8

Table A 31: Experimental data according to the geometry for 3rd series, No.3-6.

x	a _i	b _i	a _o	b _o
-184,0	12,0	9,2	112,8	107,5
-132,5	22,7	17,5	119,2	98,3
-82,0	34,2	33,2	110,7	102,4
-30,0	52,1	49,8	106,5	99,4
20,0	63,1	58,7	105,5	98,7
71,0	69,7	63,5	107,0	99,4

Table A 32: FEM calculations according to the geometry for 3rd series, No.3-6.

x	a _i	b _i	a _o	b _o
-184,0	0,0	0,0	111,4	111,4
-132,5	0,0	0,0	119,0	106,5
-82,0	37,1	35,8	117,0	102,7
-30,0	55,5	51,6	115,9	99,1
20,0	69,2	60,8	115,3	97,7
71,0	77,9	63,5	113,6	98,9

Table A 33: Experimental data according to the geometry for 4th series, No.4-1.

x	a _i	b _i	a _o	b _o
-227,9	0,0	0,0	113,3	110,8
-175,4	9,8	7,9	114,1	108,3
-124,8	36,9	35,6	113,6	105,1
-74,3	53,9	51,6	107,7	102,2
-23,8	63,5	60,2	104,8	99,4
27,8	68,7	64,6	104,9	99,5
78,3	69,9	66,0	105,0	100,3
128,8	69,9	67,1	103,9	101,5
180,4	70,2	67,2	105,2	101,5
280,9	70,4	67,8	104,8	101,8
383,4	71,1	67,4	105,3	101,5
484,9	70,3	67,5	105,4	101,3
587,5	71,1	67,3	105,6	101,4
693,0	71,8	67,3	106,5	101,9

Table A 34: FEM calculations according to the geometry for 4th series, No.4-1.

x	a _i	b _i	a _o	b _o
-227,9	0,0	0,0	116,7	111,9
-175,4	0,0	0,0	119,3	108,9
-124,8	31,3	31,1	124,1	106,4
-74,3	49,4	48,1	121,6	102,5
-23,8	61,4	59,1	114,8	99,2
27,8	74,1	63,0	115,1	98,3
78,3	80,9	64,1	114,4	98,8
128,8	73,1	66,7	107,4	100,6
180,4	71,6	67,5	104,1	102,4
280,9	70,1	68,4	104,8	102,8
383,4	69,5	68,4	103,7	103,3
484,9	69,7	68,5	104,0	102,8
587,5	70,3	68,9	104,2	103,5
693,0	70,0	69,6	105,3	103,8

Table A 35: Experimental data according to the geometry for 4th series, No.4-2.

x	a _i	b _i	a _o	b _o
-215,5	11,7	9,9	114,0	108,3
-162,9	28,0	27,0	114,9	106,2
-111,4	47,9	46,6	109,3	102,9
-60,8	60,1	56,9	105,7	99,8
-6,3	67,9	62,8	105,1	98,9
45,3	71,0	65,3	106,6	99,6
96,9	70,0	67,3	104,8	101,4
149,4	69,7	68,4	103,9	102,5
250,0	71,0	68,5	104,9	102,3
351,5	71,4	67,8	105,0	101,7
454,1	70,7	68,2	104,6	101,6
556,6	69,5	68,6	103,3	102,1
658,2	70,9	68,1	104,7	101,5
760,7	71,3	67,6	105,3	101,0
863,3	69,8	68,4	104,1	101,6
965,8	69,5	68,4	103,1	102,1
1080,4	69,7	68,8	103,3	102,4

Table A 36: FEM calculations according to the geometry for 4th series, No.4-2.

x	a _i	b _i	a _o	b _o
-215,5	0,0	0,0	116,1	110,7
-162,9	0,0	0,0	118,7	108,2
-111,4	37,0	36,1	120,5	105,4
-60,8	55,0	51,7	125,4	98,3
-6,3	68,0	61,2	103,0	103,0
45,3	78,1	63,9	114,0	98,0
96,9	76,4	65,0	110,4	99,1
149,4	71,5	67,0	105,4	101,3
250,0	68,8	68,6	103,1	102,6
351,5	69,5	68,4	103,2	101,8
454,1	69,0	68,5	102,8	102,8
556,6	69,3	68,8	103,7	103,4
658,2	69,4	69,0	103,8	103,6
760,7	69,2	69,2	103,7	102,5
863,3	70,0	68,8	104,1	103,4
965,8	69,3	69,3	104,3	103,5
1080,4	70,2	69,5	104,5	104,1

Table A 37: Experimental data according to the geometry for 4th series, No.4-3.

x	a _i	b _i	a _o	b _o
-281,6	0,0	0,0	112,2	109,8
-180,1	19,0	16,9	113,8	106,9
-129,5	39,2	37,9	113,1	103,6
-79,9	54,7	52,5	107,7	100,2
-28,3	64,8	60,2	105,4	98,4
22,3	69,9	63,2	106,2	97,6
72,9	70,4	65,3	104,8	99,5
122,5	69,3	67,0	103,3	100,6
174,1	68,5	68,0	102,3	102,0
225,6	69,1	68,2	103,0	102,2
326,2	69,9	67,6	103,9	101,3
428,8	70,4	67,8	104,1	101,1
531,4	69,4	68,4	103,2	102,2
633,0	69,6	69,0	104,0	103,0

Table A 38: FEM calculations according to the geometry for 4th series, No.4-3.

x	a _i	b _i	a _o	b _o
-281,6	0,0	0,0	115,3	113,3
-180,1	0,0	0,0	116,4	108,8
-129,5	29,7	29,0	122,6	105,7
-79,9	50,3	46,6	128,0	99,0
-28,3	63,5	58,3	124,0	95,6
22,3	76,1	62,8	109,4	98,5
72,9	79,2	64,2	111,3	98,9
122,5	72,0	66,6	108,8	98,6
174,1	69,7	68,0	103,2	101,9
225,6	69,0	68,4	103,7	102,4
326,2	69,1	68,4	103,1	102,7
428,8	68,7	68,7	103,1	102,8
531,4	69,2	68,8	103,3	103,0
633,0	69,7	69,3	103,8	103,5

Table A 39: Experimental data according to the geometry for 4th series, No.4-4.

x	a _i	b _i	a _o	b _o
-157,2	8,9	7,9	114,1	107,1
-106,8	24,1	23,5	113,9	103,9
-56,4	44,6	43,7	109,0	100,8
-6,0	58,5	55,8	106,3	98,6
46,4	68,1	62,0	106,5	98,6
98,8	71,4	64,4	108,1	99,6
151,2	70,5	65,9	106,1	101,1
200,6	69,8	68,1	104,6	102,8
255,0	70,0	68,5	105,3	103,3
354,4	70,0	68,8	105,2	103,2
454,8	70,2	68,3	104,8	103,1
557,2	69,1	68,8	104,1	103,5
657,6	69,2	68,7	104,5	103,5
758,0	70,2	68,6	104,8	103,1
859,4	69,6	68,9	104,3	103,7
961,8	69,6	68,6	104,2	103,6
1063,2	69,5	69,1	104,2	103,4

Table A 40: FEM calculations according to the geometry for 4th series, No.4-4.

x	a _i	b _i	a _o	b _o
-157,2	0,0	0,0	117,9	108,5
-106,8	26,2	26,2	122,0	105,0
-56,4	45,7	44,6	118,1	101,2
-6,0	60,3	56,8	116,5	98,5
46,4	75,4	62,6	115,5	98,5
98,8	78,5	64,5	115,3	99,6
151,2	72,6	66,5	107,7	101,9
200,6	70,5	67,8	105,1	102,8
255,0	69,1	68,7	107,9	101,4
354,4	69,8	68,6	104,9	103,7
454,8	69,7	68,8	105,5	104,6
557,2	69,4	69,1	105,2	104,8
657,6	69,8	68,7	105,4	104,5
758,0	69,9	69,0	106,1	101,9
859,4	69,9	69,4	104,7	104,7
961,8	69,5	69,5	104,6	104,6
1063,2	69,9	69,4	105,0	104,5

Table A 41: Experimental data according to the geometry for 4th series, No.4-5.

x	a _i	b _i	a _o	b _o
-172,3	0,0	0,0	113,8	103,9
-121,0	10,8	9,1	113,7	106,7
-69,7	44,5	43,6	108,4	100,7
-19,3	58,9	55,9	106,0	98,5
27,0	67,3	61,9	106,4	98,8
78,3	71,2	64,8	107,6	99,6
129,7	70,3	66,5	105,8	101,2
181,0	69,8	67,5	104,7	102,4
231,3	69,5	68,8	104,0	103,5
332,7	70,4	68,0	104,9	102,8
433,0	69,1	68,3	104,4	103,6
533,3	69,5	68,6	104,3	103,6
634,7	69,1	68,9	104,0	103,2
736,0	70,0	68,5	104,3	103,3
836,3	69,3	69,1	103,9	103,7
938,7	69,7	69,3	104,3	103,9
1038,0	70,1	69,9	105,4	104,5

Table A 42: FEM calculations according to the geometry for 4th series, No.4-5.

x	a _i	b _i	a _o	b _o
-172,3	0,0	0,0	116,9	108,8
-121,0	19,6	18,6	120,1	106,0
-69,7	41,3	40,5	120,1	101,7
-19,3	57,5	54,2	116,4	98,8
27,0	69,7	61,7	114,7	98,3
78,3	79,1	64,0	115,2	99,1
129,7	68,8	68,8	107,2	100,8
181,0	71,0	67,2	106,4	102,4
231,3	68,9	68,4	104,5	103,5
332,7	69,1	68,4	104,0	104,0
433,0	69,1	68,4	108,5	101,4
533,3	69,8	68,7	104,8	104,4
634,7	69,4	68,8	104,5	104,0
736,0	69,6	68,9	104,3	104,3
836,3	69,8	69,1	105,4	104,5
938,7	69,5	69,4	105,2	104,9
1038,0	70,2	69,7	106,4	102,5

Table A 43: Experimental data according to the geometry for 4th series, No.4-6.

x	a _i	b _i	a _o	b _o
-226,0	5,9	5,3	118,7	100,7
-175,2	15,0	10,4	113,7	106,2
-124,4	25,5	23,7	113,2	103,8
-73,6	45,1	44,0	108,1	100,5
-21,8	59,3	56,1	106,0	98,3
78,0	70,9	64,2	107,3	99,1
178,8	69,3	67,8	104,1	102,1
280,6	69,6	68,1	103,9	102,9
382,4	70,1	67,6	105,0	102,0
484,2	69,5	68,4	103,8	102,8
586,0	69,4	68,7	103,9	103,0
687,8	69,6	68,4	104,0	102,8
789,6	70,1	68,3	104,3	102,9
891,4	69,7	68,7	103,9	103,6
993,2	69,9	69,4	104,3	103,9
1095,0	70,5	69,9	105,0	104,2

Table A 44: FEM calculations according to the geometry for 4th series, No.4-6.

x	a _i	b _i	a _o	b _o
-226,0	0,0	0,0	115,1	111,0
-175,2	0,0	0,0	116,3	108,4
-124,4	16,9	14,6	110,7	110,7
-73,6	40,7	39,0	119,0	102,2
-21,8	58,0	53,7	116,4	98,6
78,0	77,0	64,0	117,3	96,9
178,8	69,8	67,3	105,4	102,2
280,6	69,0	68,1	103,1	103,1
382,4	68,7	68,1	104,8	100,0
484,2	68,7	68,5	103,9	103,8
586,0	69,0	68,5	106,3	102,1
687,8	69,1	68,7	104,6	102,6
789,6	69,0	68,9	104,6	103,5
891,4	69,4	68,9	104,1	104,1
993,2	69,6	69,3	105,1	103,6
1095,0	70,4	70,2	105,6	105,6

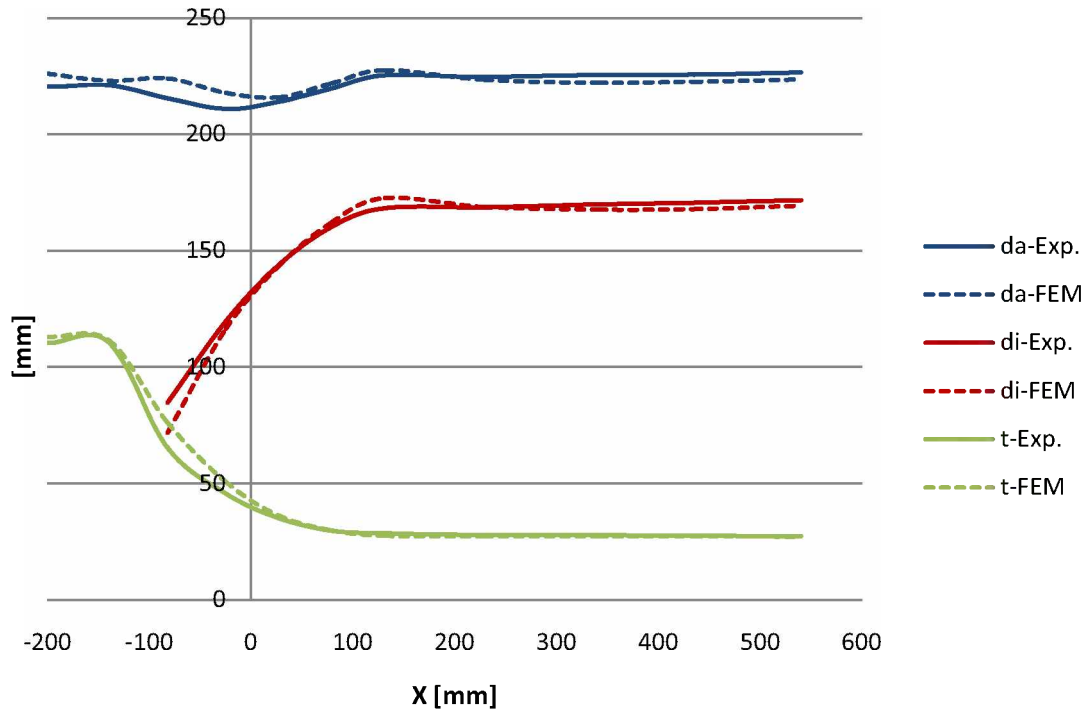


Figure A 1: Comparison of the geometry behavior between the FEM and experiment for 1st series, No.1-1.

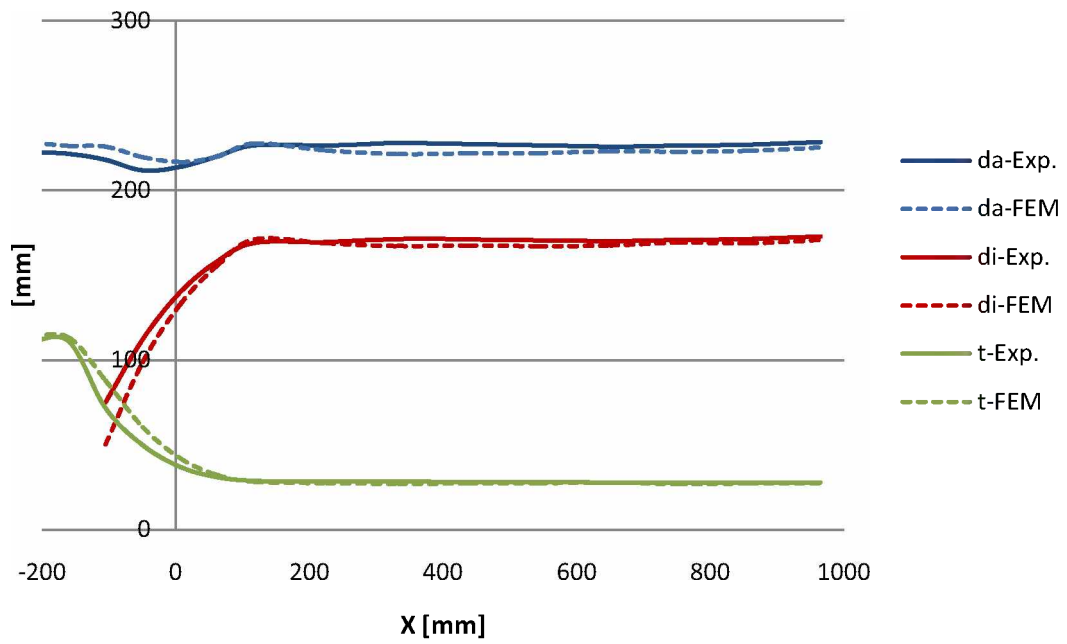


Figure A 2: Comparison of the geometry behavior between the FEM and experiment for 1st series, No.1-3.

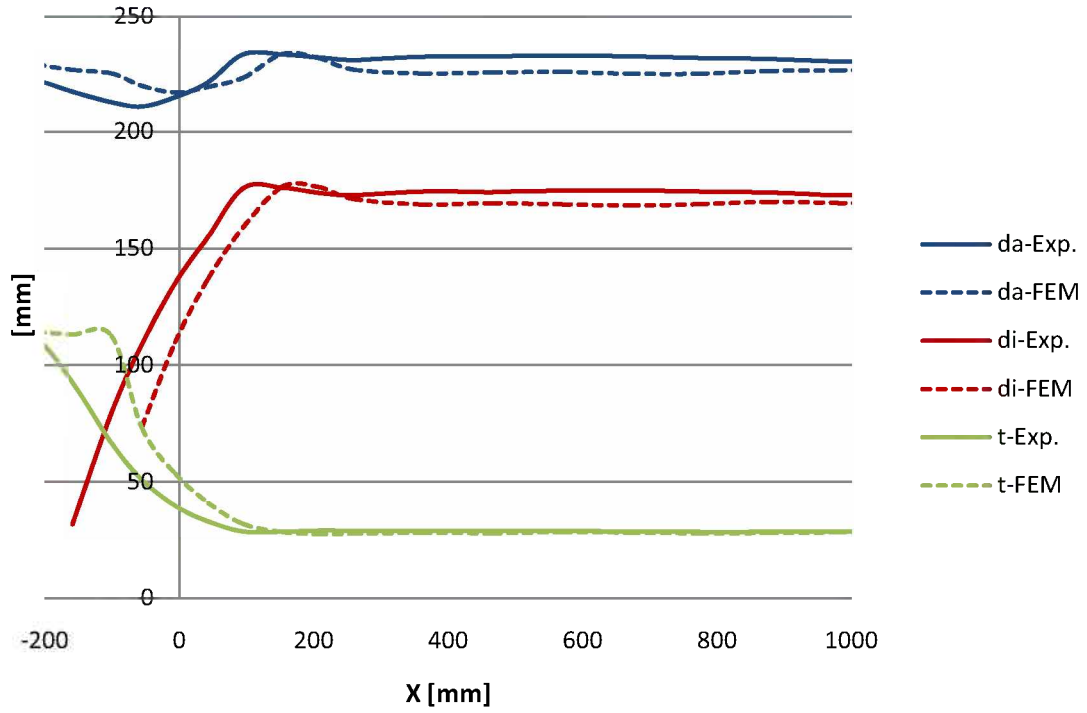


Figure A 3: Comparison of the geometry behavior between the FEM and experiment for 1st series, No.1-4.

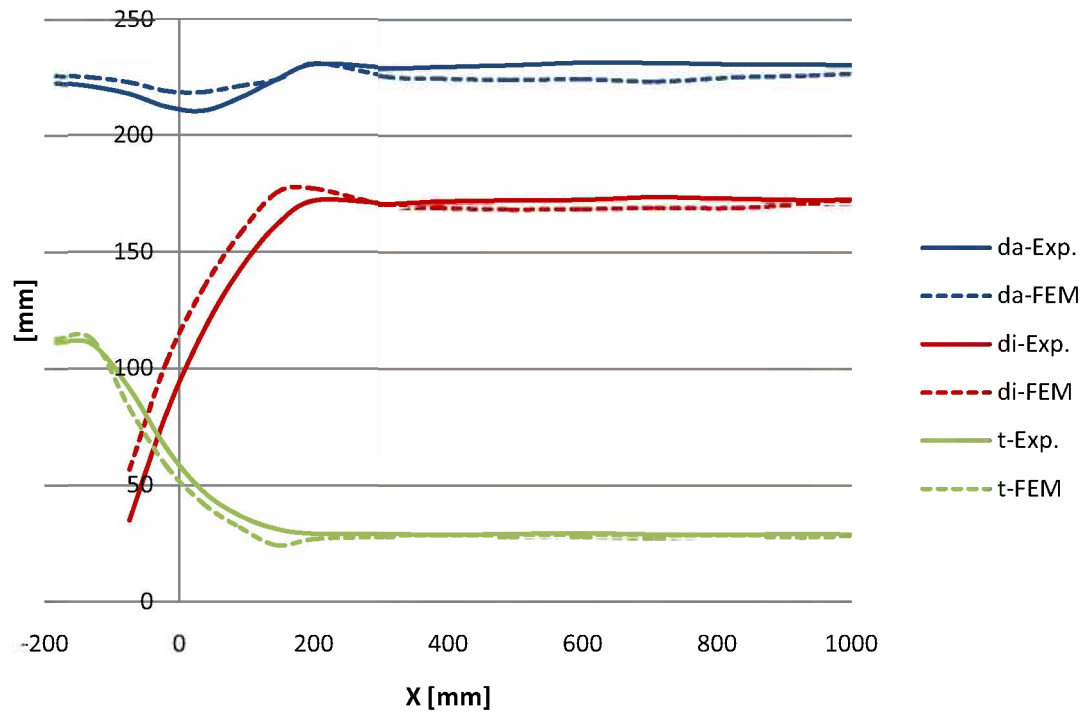


Figure A 4: Comparison of the geometry behavior between the FEM and experiment for 1st series, No.1-5.

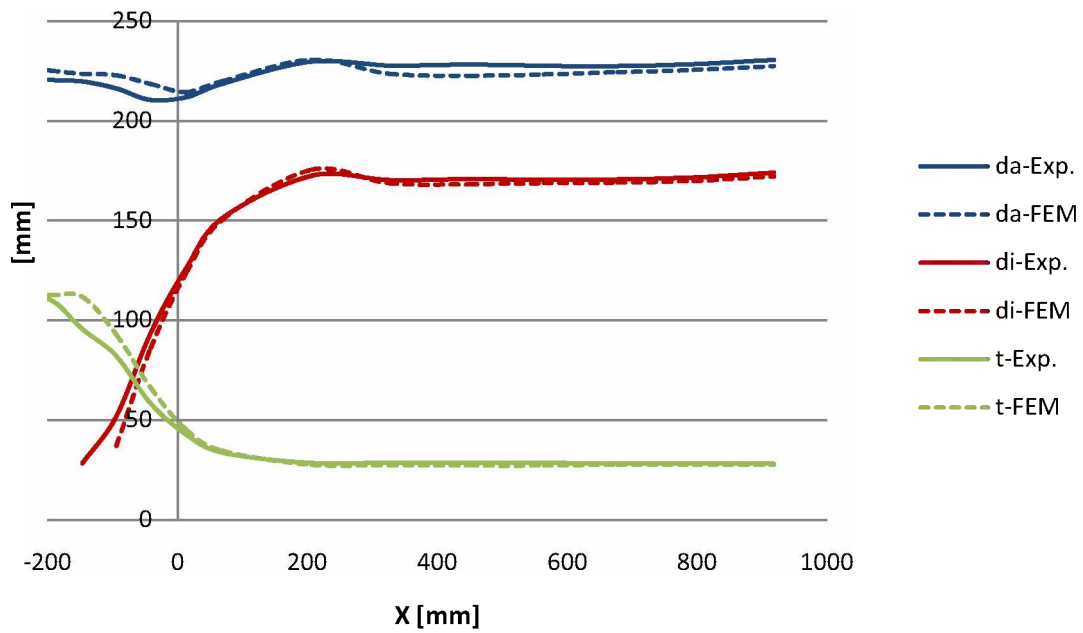


Figure A 5: Comparison of the geometry behavior between the FEM and experiment for 1st series, No.1-6.

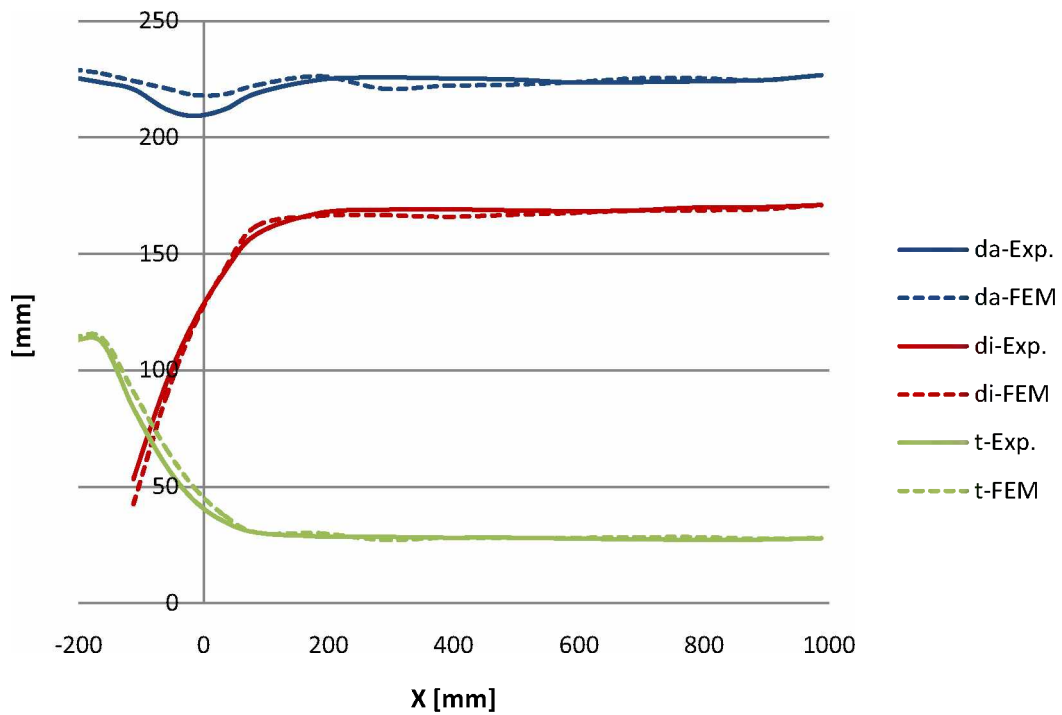


Figure A 6: Comparison of the geometry behavior between the FEM and experiment for 2nd series, No.2-1.

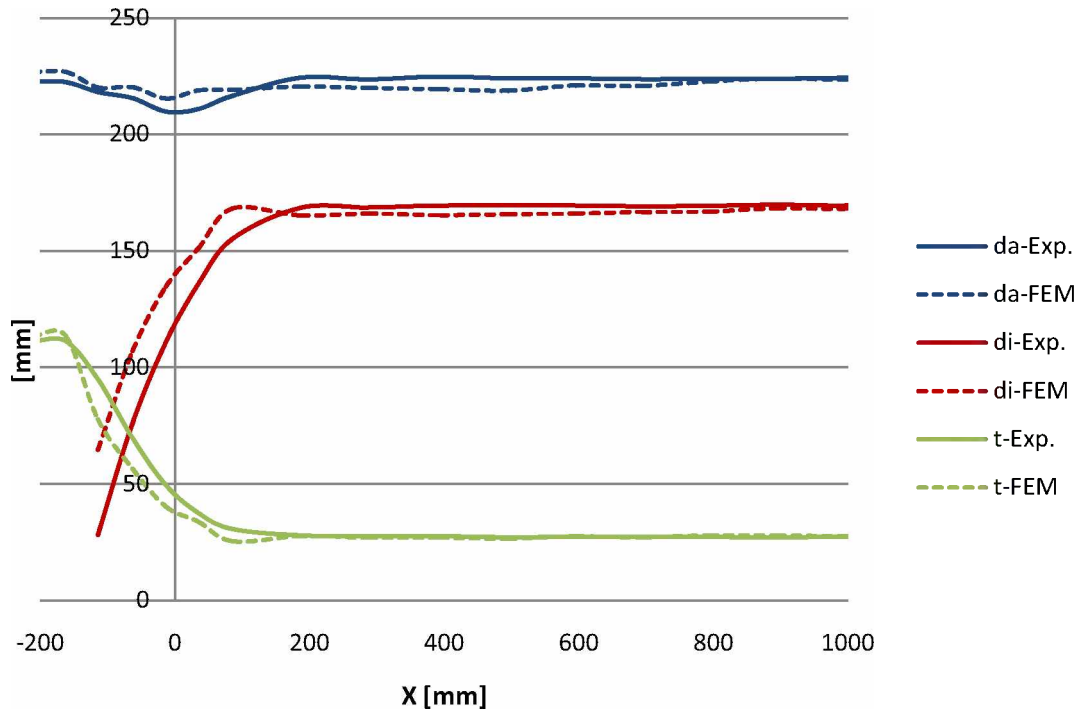


Figure A 7: Comparison of the geometry behavior between the FEM and experiment for 2nd series, No.2-3.

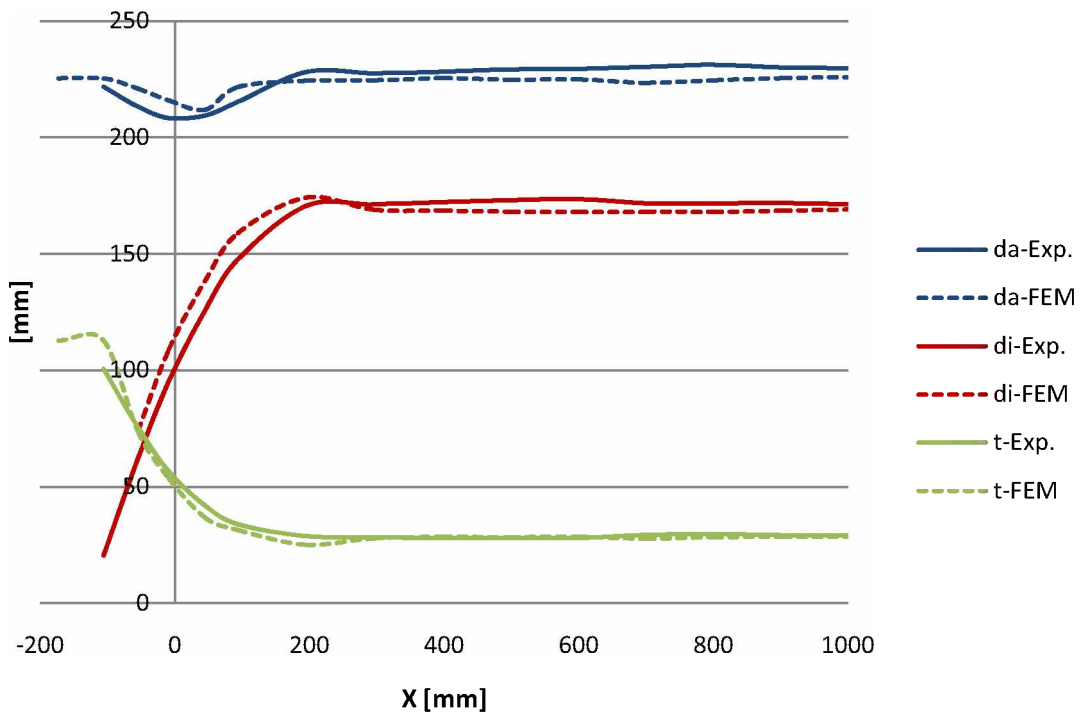


Figure A 8: Comparison of the geometry behavior between the FEM and experiment for 2nd series, No.2-4.

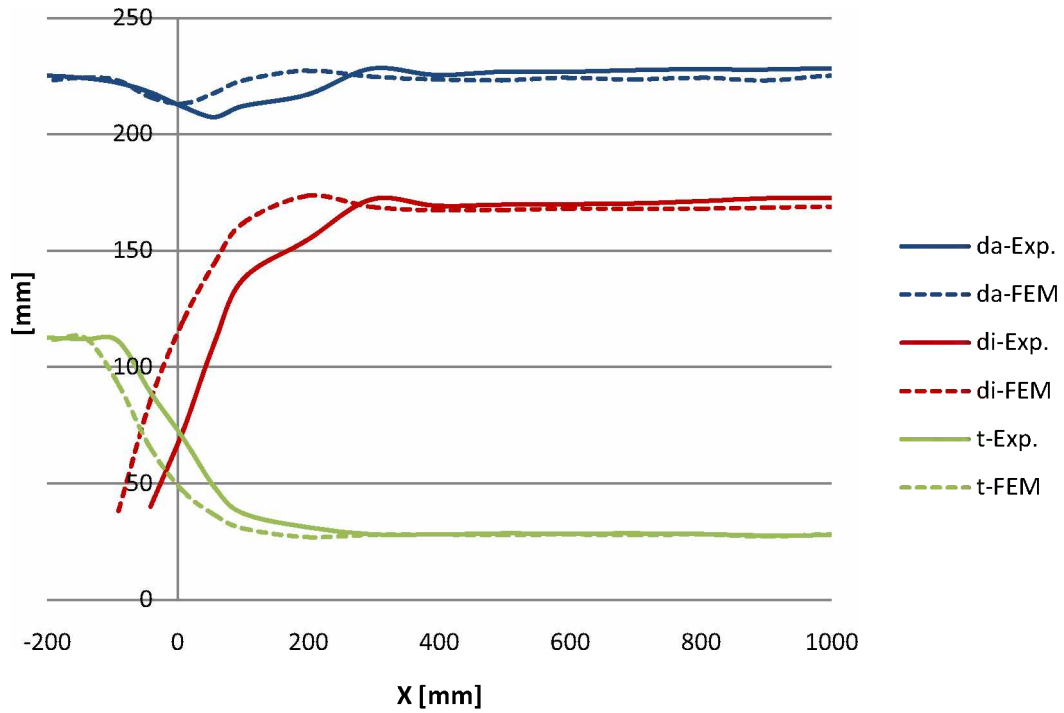


Figure A 9: Comparison of the geometry behavior between the FEM and experiment for 2nd series, No.2-5.

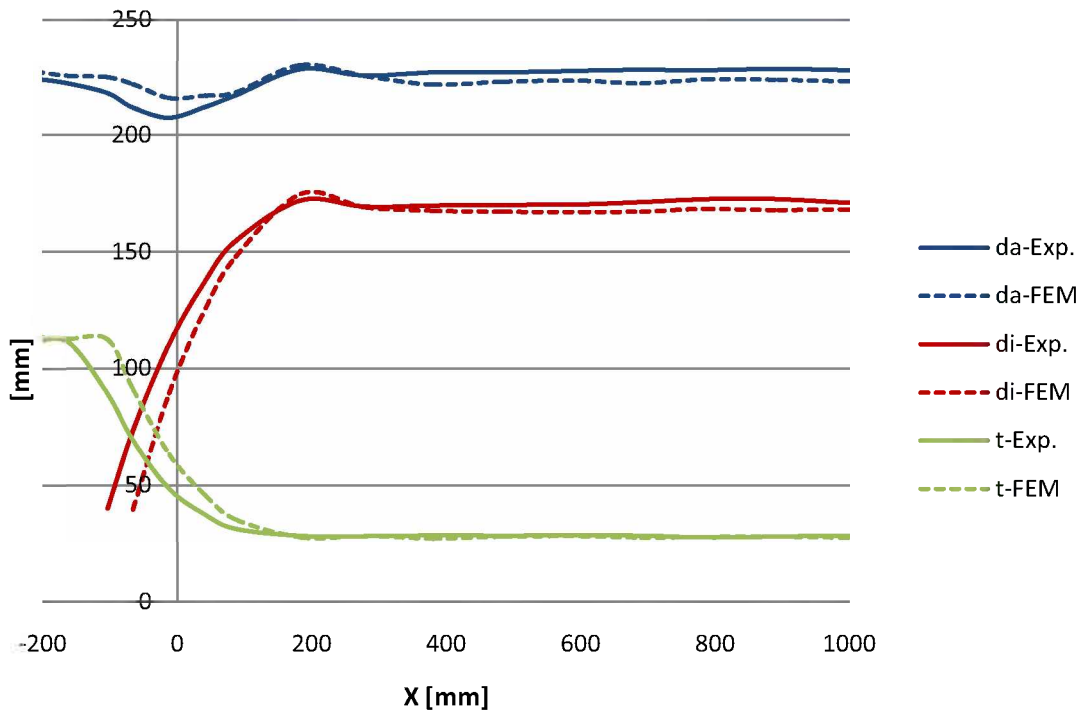


Figure A 10: Comparison of the geometry behavior between the FEM and experiment for 2nd series, No.2-6.

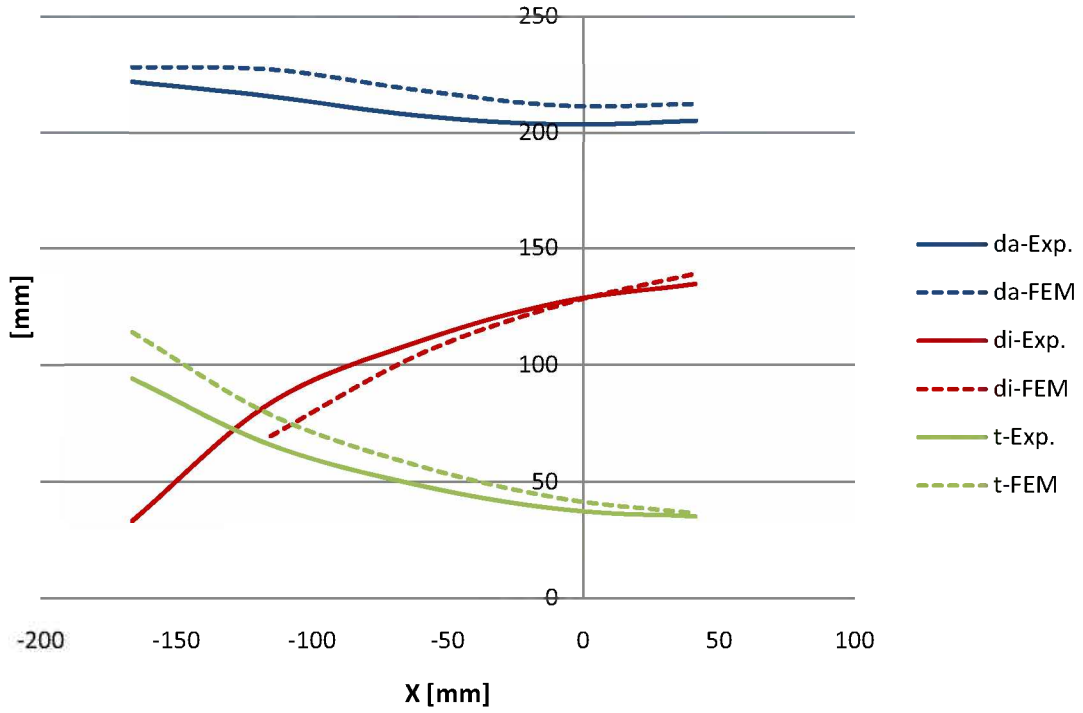


Figure A 11: Comparison of the geometry behavior between the FEM and experiment for 3rd series, No.3-1.

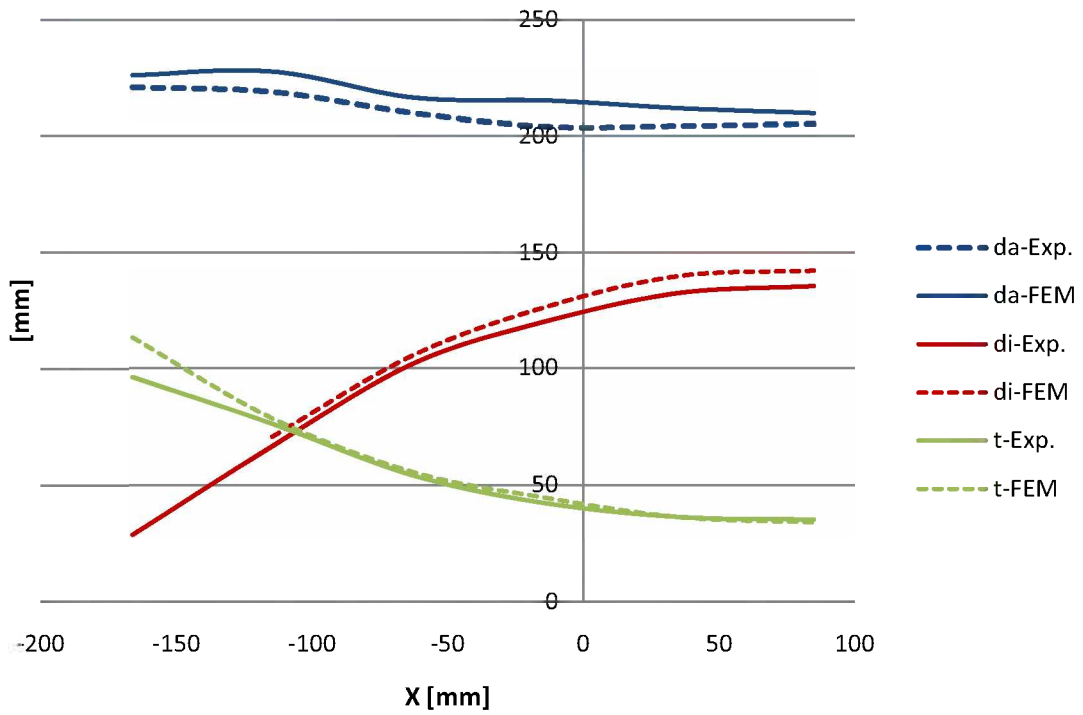


Figure A 12: Comparison of the geometry behavior between the FEM and experiment for 3rd series, No.3-2.

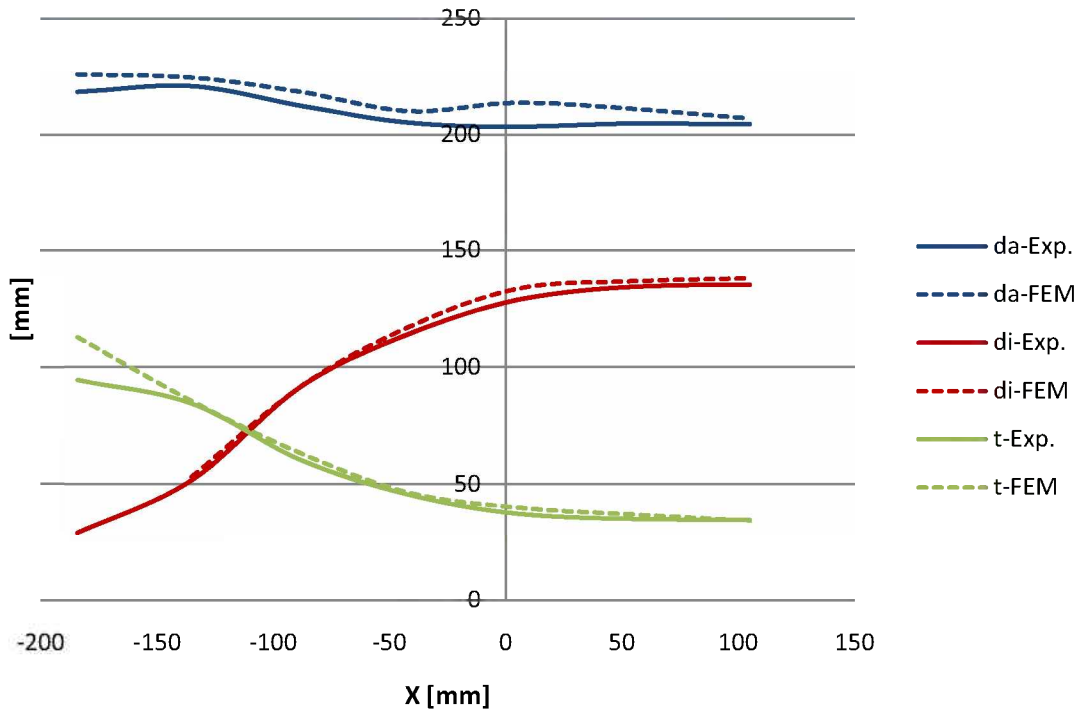


Figure A 13: Comparison of the geometry behavior between the FEM and experiment for 3rd series, No.3-1.

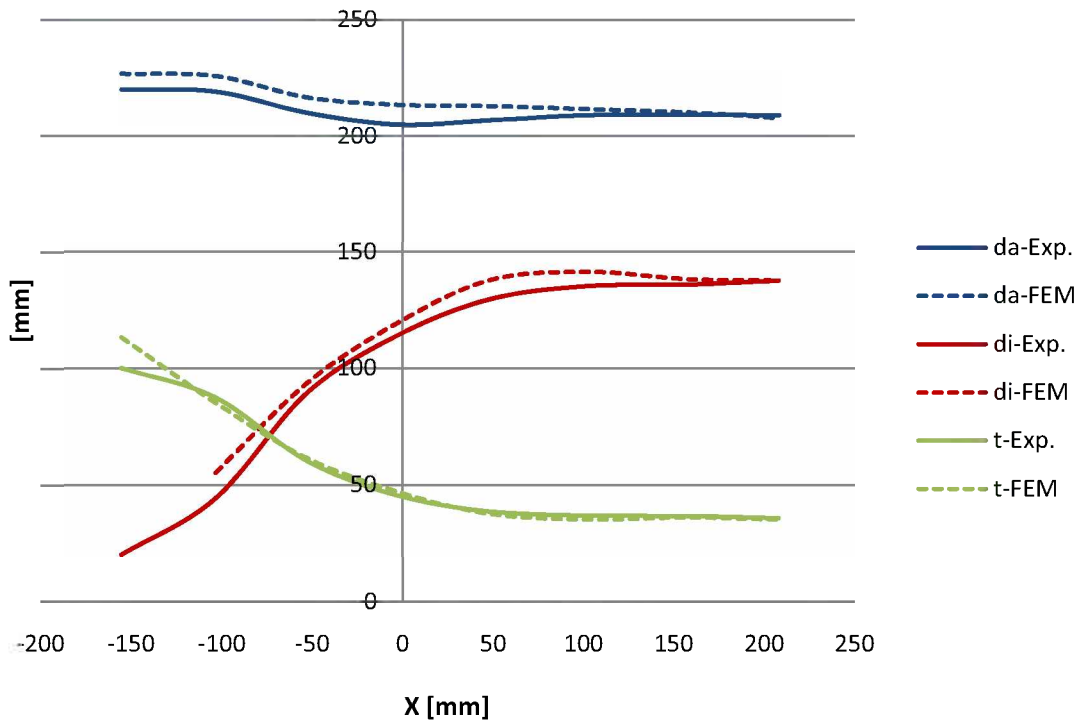


Figure A 14: Comparison of the geometry behavior between the FEM and experiment for 3rd series, No.3-4.

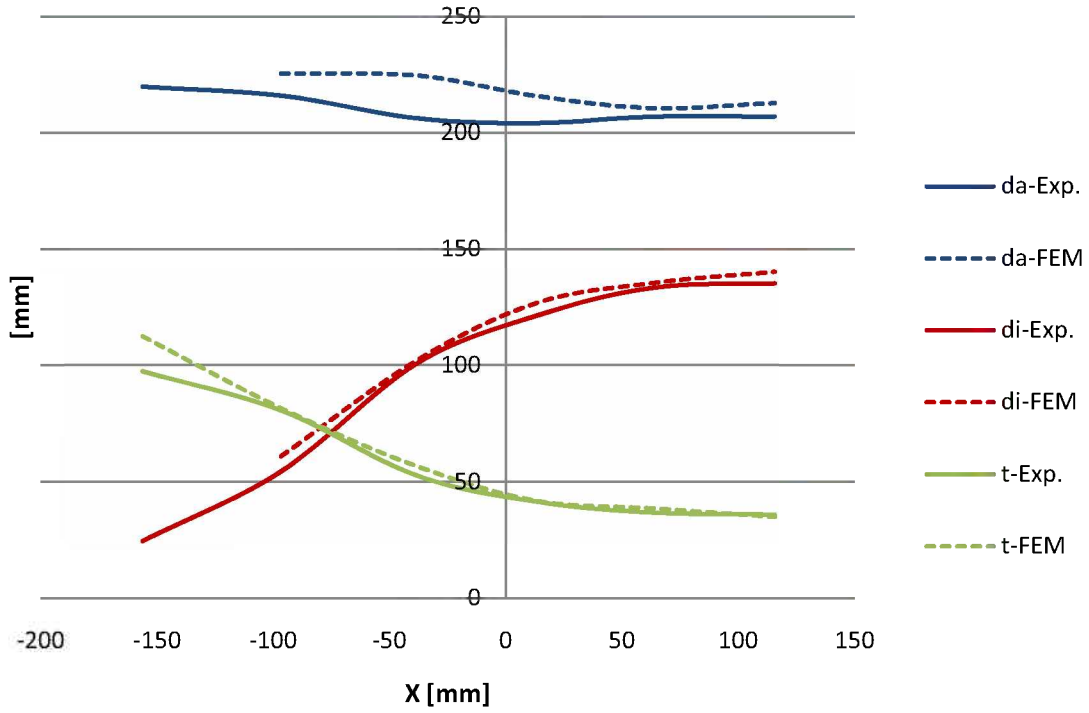


Figure A 15: Comparison of the geometry behavior between the FEM and experiment for 3rd series, No.3-5.

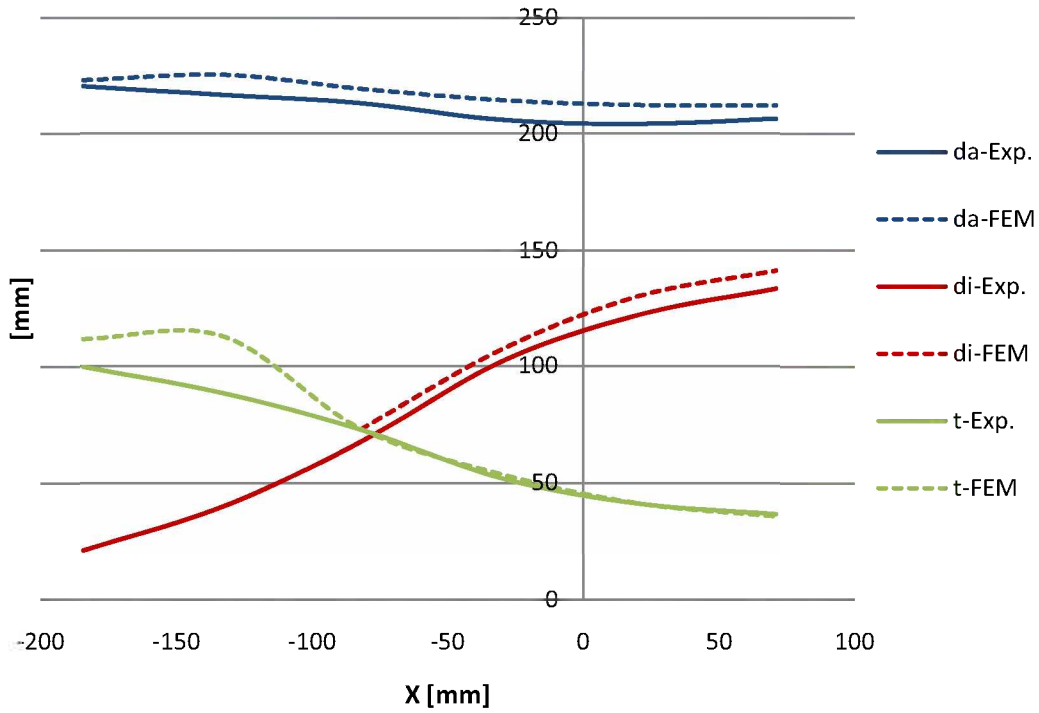


Figure A 16: Comparison of the geometry behavior between the FEM and experiment for 3rd series, No.3-6.

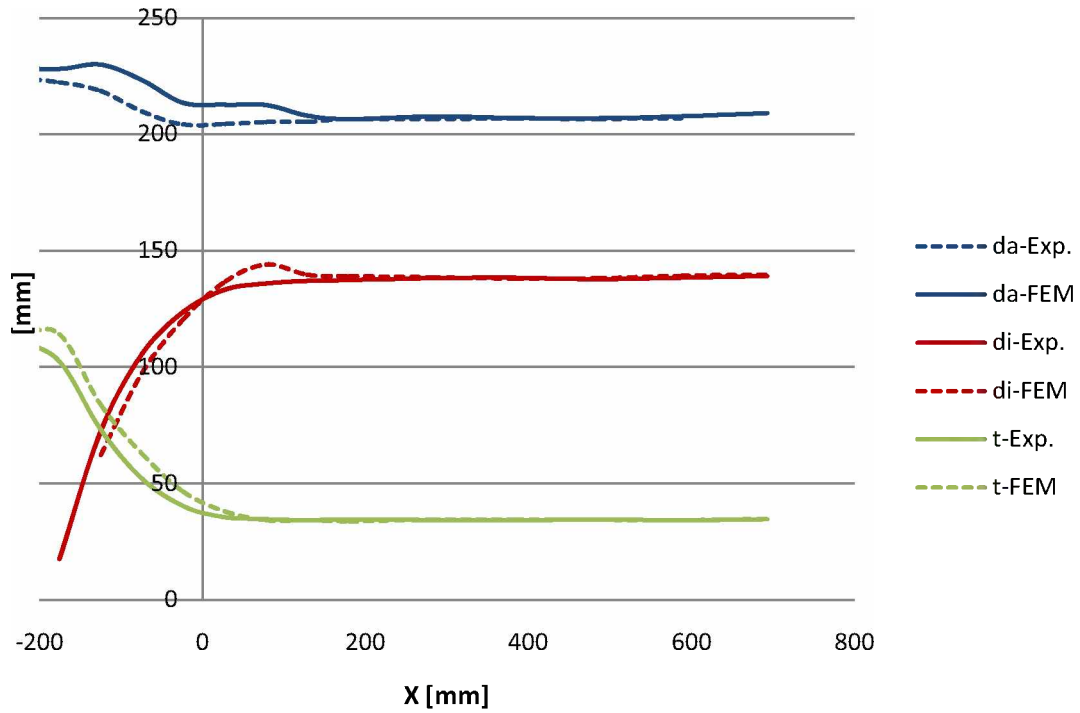


Figure A 17: Comparison of the geometry behavior between the FEM and experiment for 4th series, No.4-1.

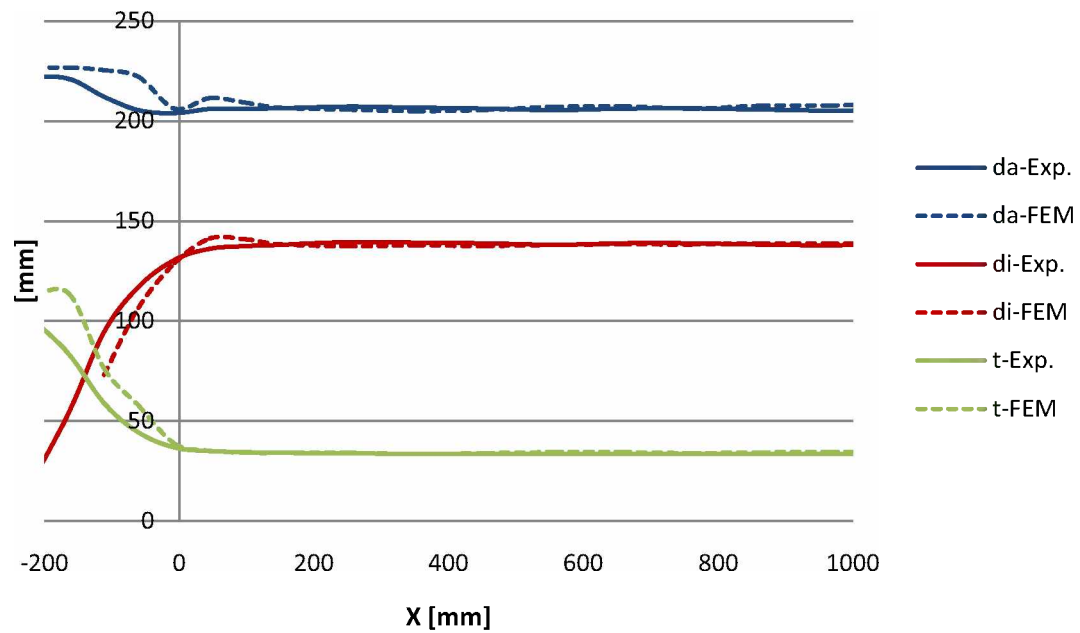


Figure A 18: Comparison of the geometry behavior between the FEM and experiment for 4th series, No.4-2.

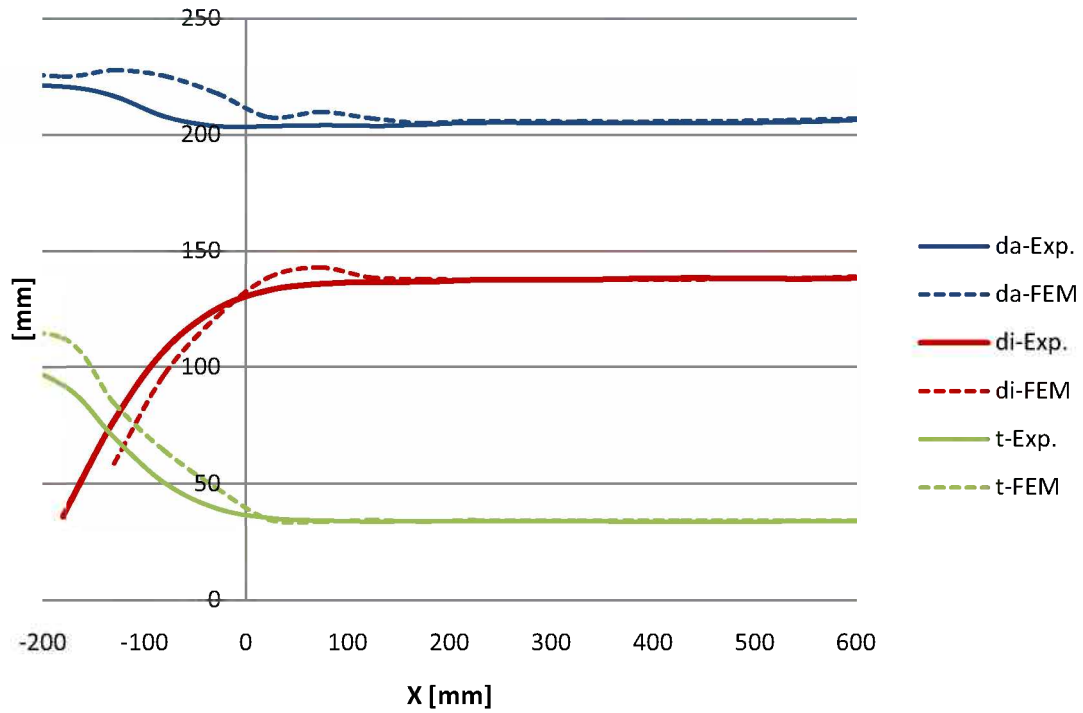


Figure A 19: Comparison of the geometry behavior between the FEM and experiment for 4th series, No.4-3.

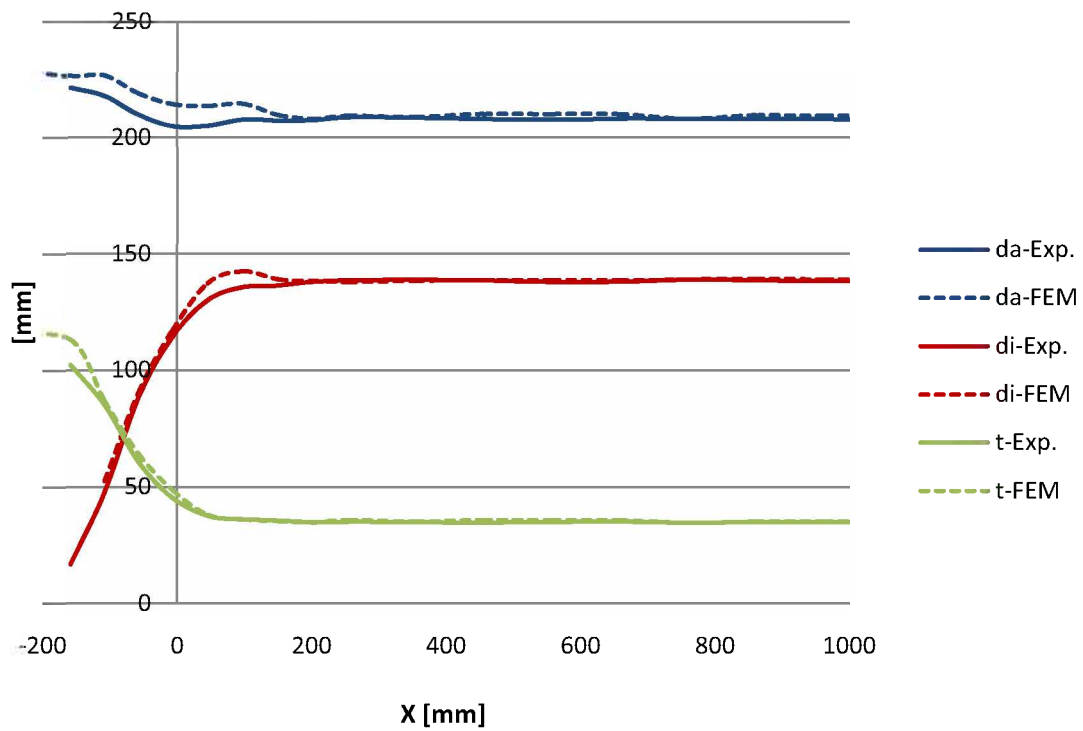


Figure A 20: Comparison of the geometry behavior between the FEM and experiment for 4th series, No.4-4.

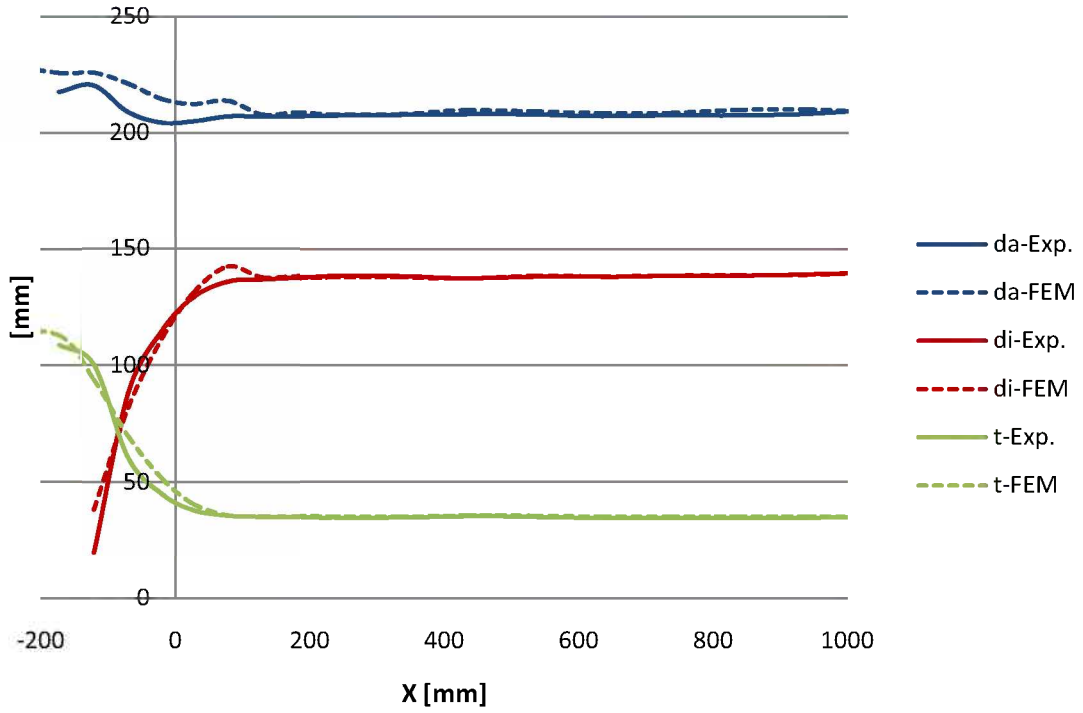


Figure A 21: Comparison of the geometry behavior between the FEM and experiment for 4th series, No.4-5.

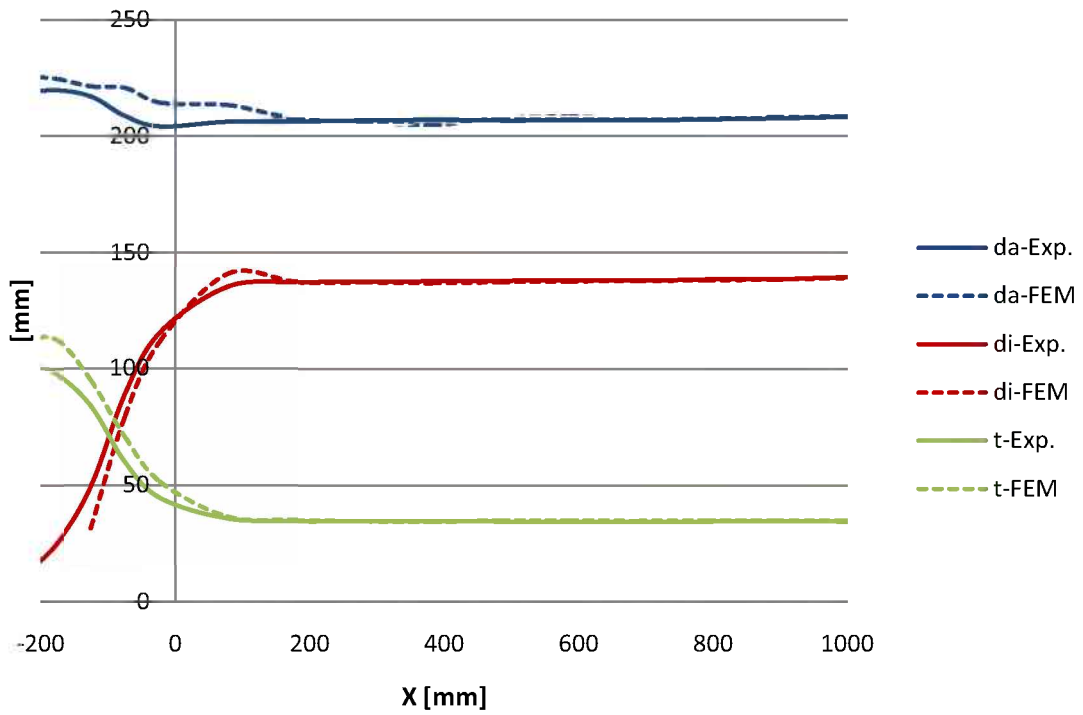


Figure A 22: Comparison of the geometry behavior between the FEM and experiment for 4th series, No.4-6.

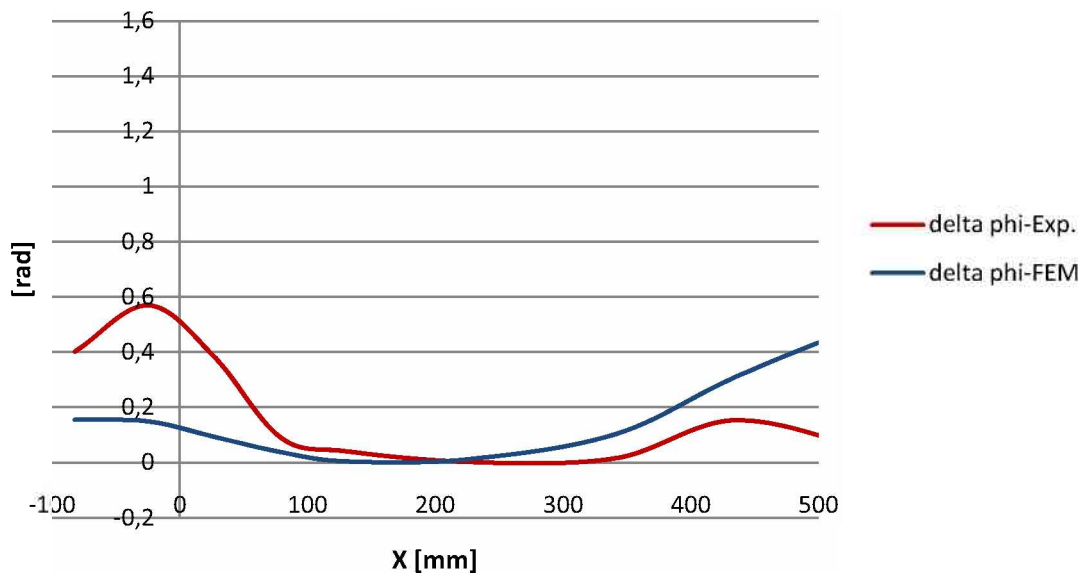


Figure A 23: Comparison of delta phi between the FEM and experiment for 1st series, No.1-1.

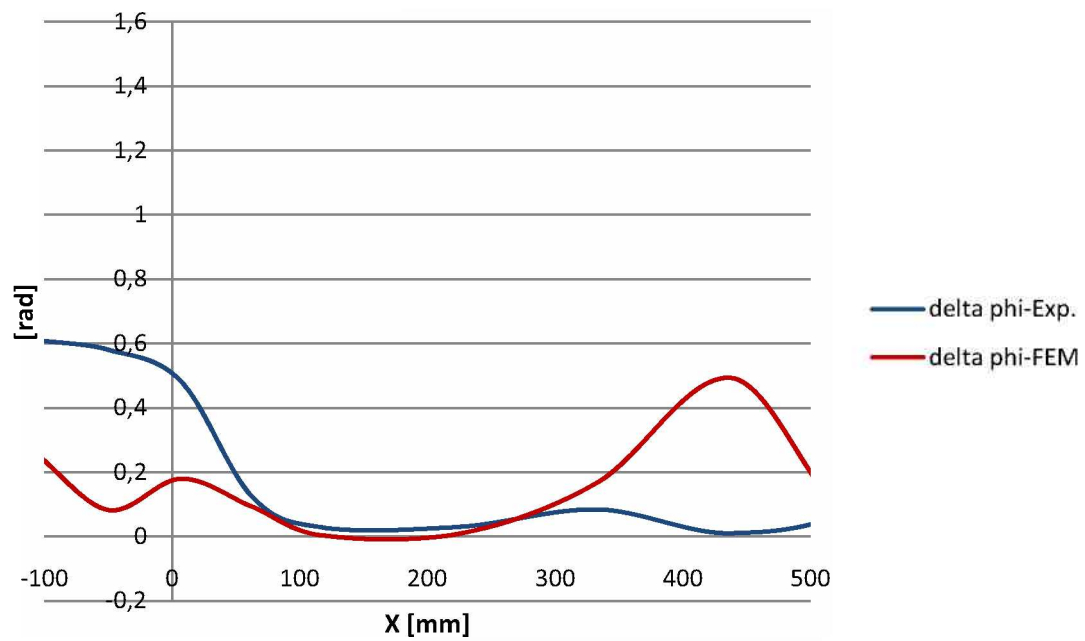


Figure A 24: Comparison of delta phi between the FEM and experiment for 1st series, No.1-3.

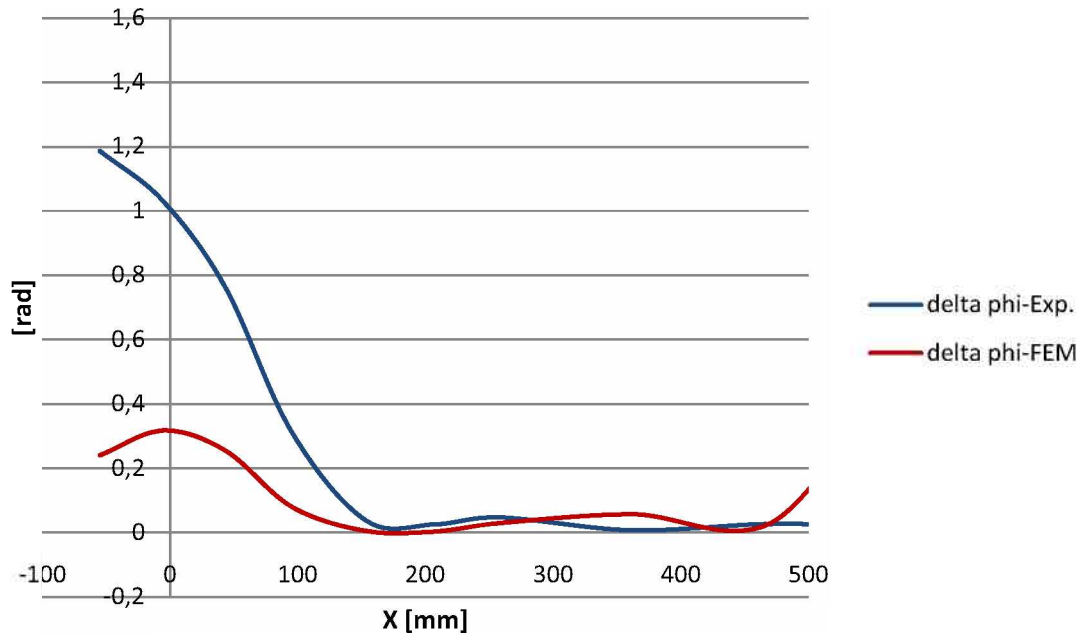


Figure A 25: Comparison of delta phi between the FEM and experiment for 1st series, No.1-4.

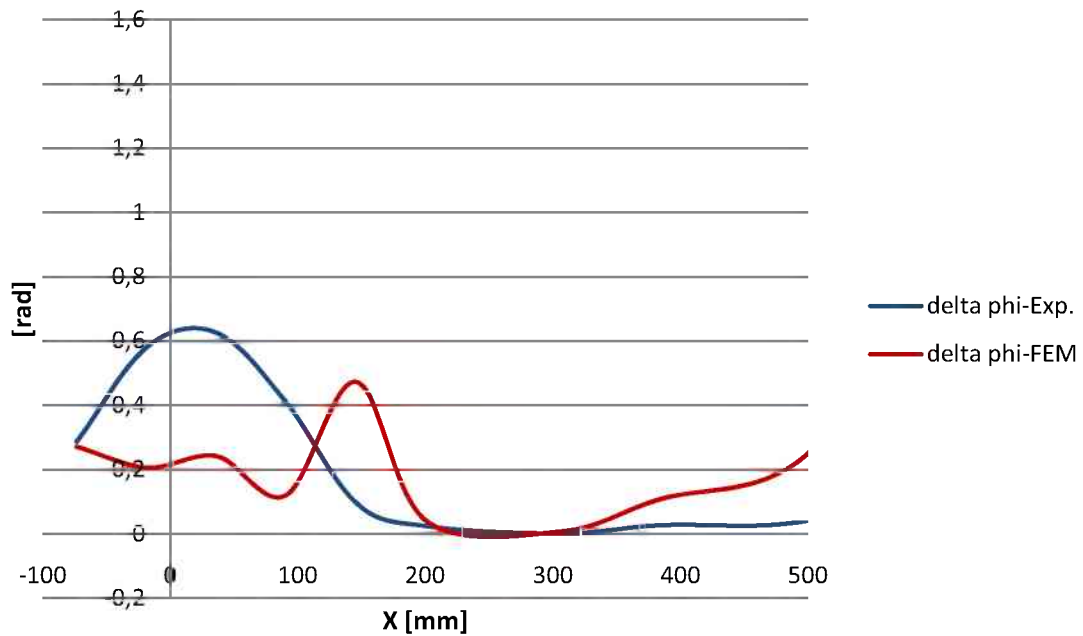


Figure A 26: Comparison of delta phi between the FEM and experiment for 1st series, No.1-5.

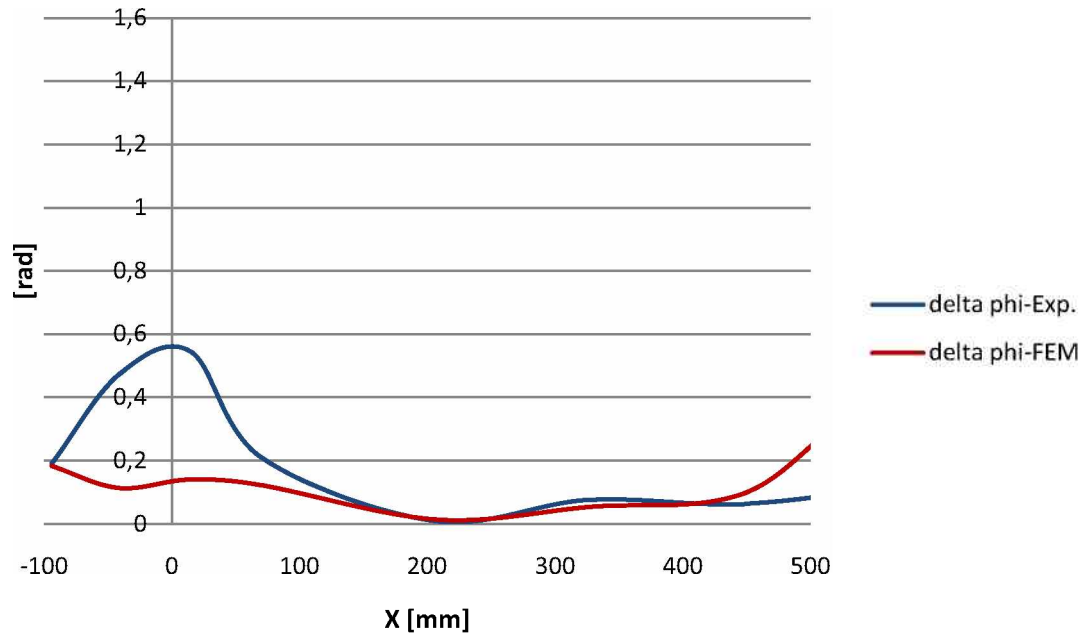


Figure A 27: Comparison of delta phi between the FEM and experiment for 1st series, No.1-6.

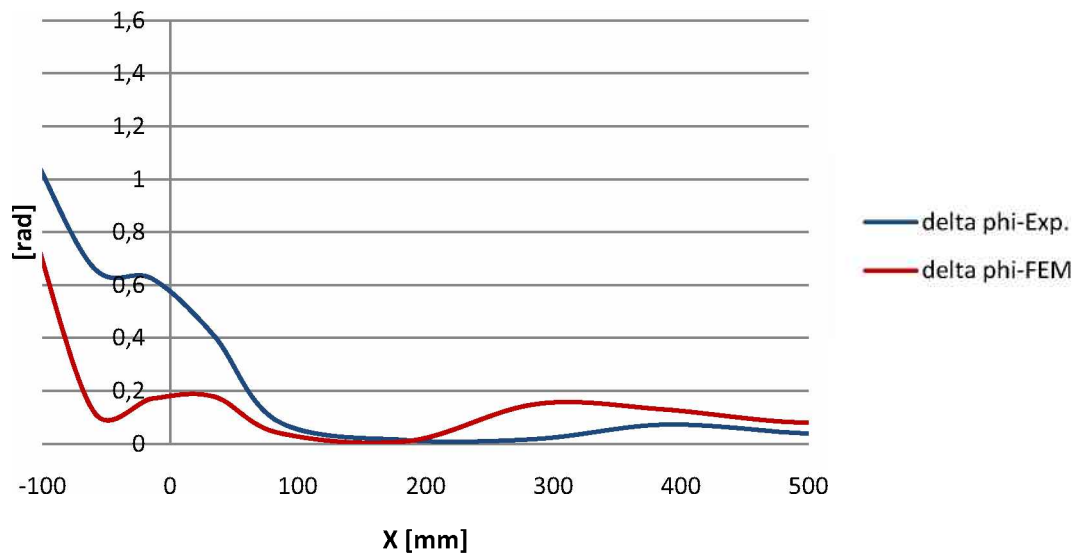


Figure A 28: Comparison of delta phi between the FEM and experiment for 2nd series, No.2-1.

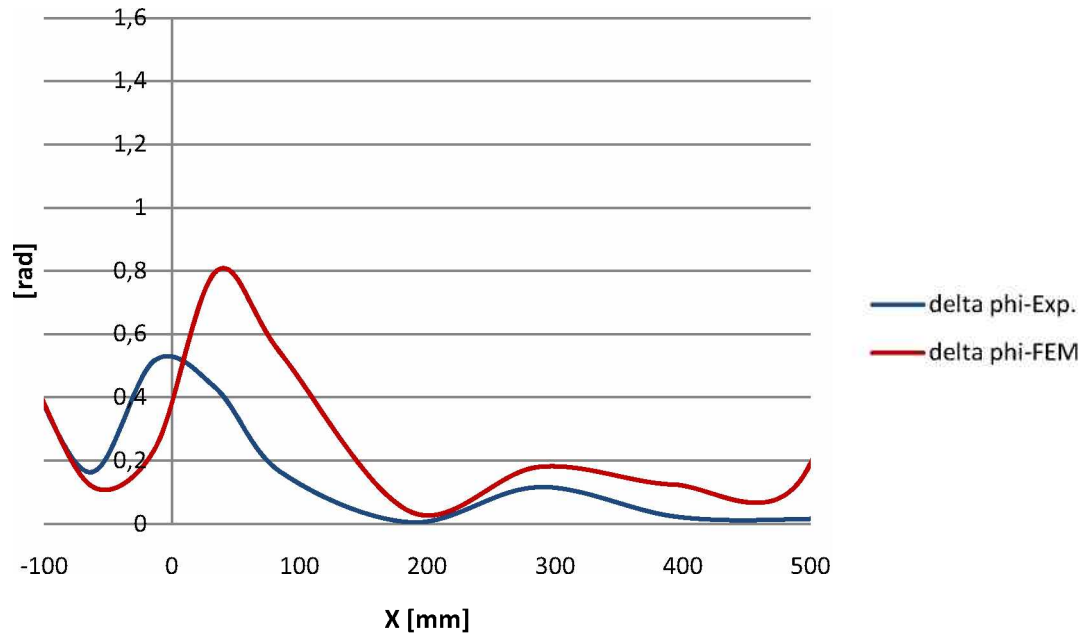


Figure A 29: Comparison of delta phi between the FEM and experiment for 2nd series, No.2-3.

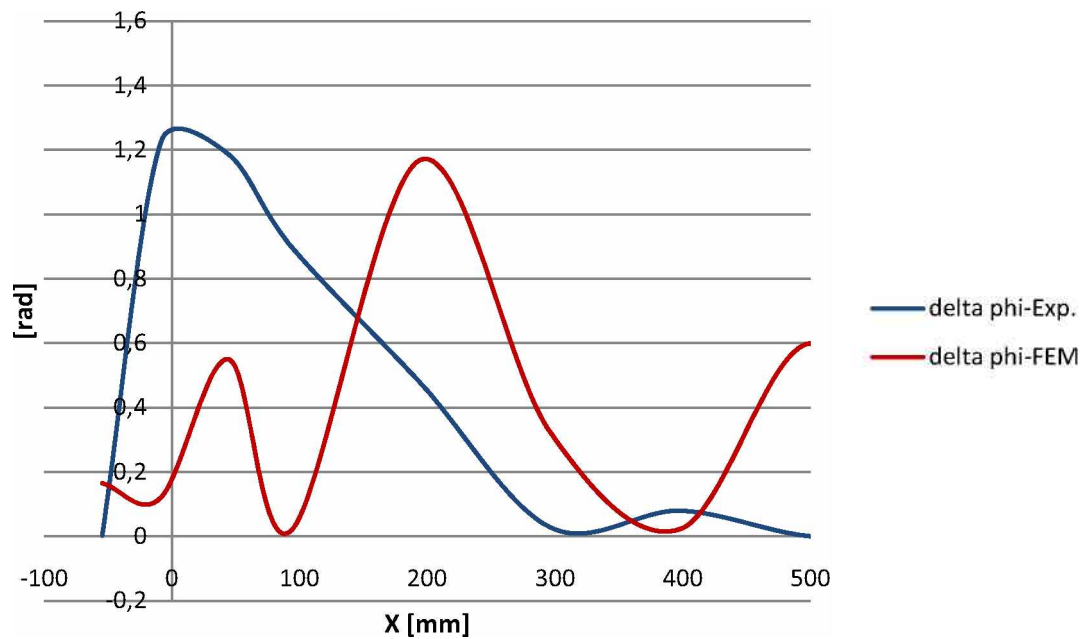


Figure A 30: Comparison of delta phi between the FEM and experiment for 2nd series, No.2-4.

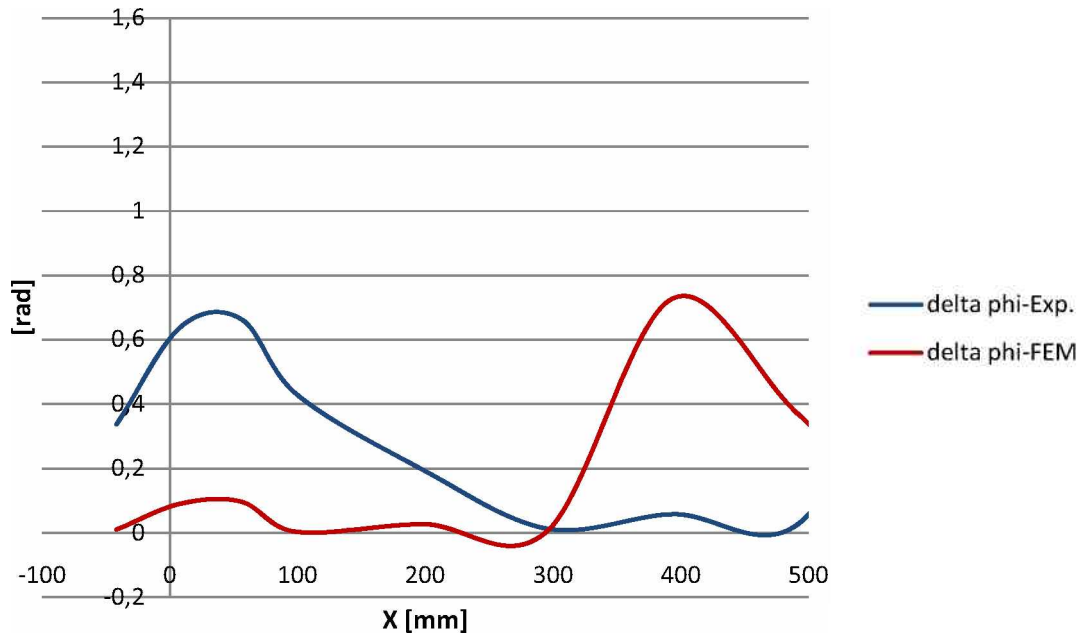


Figure A 31: Comparison of delta phi between the FEM and experiment for 2nd series, No.2-5.

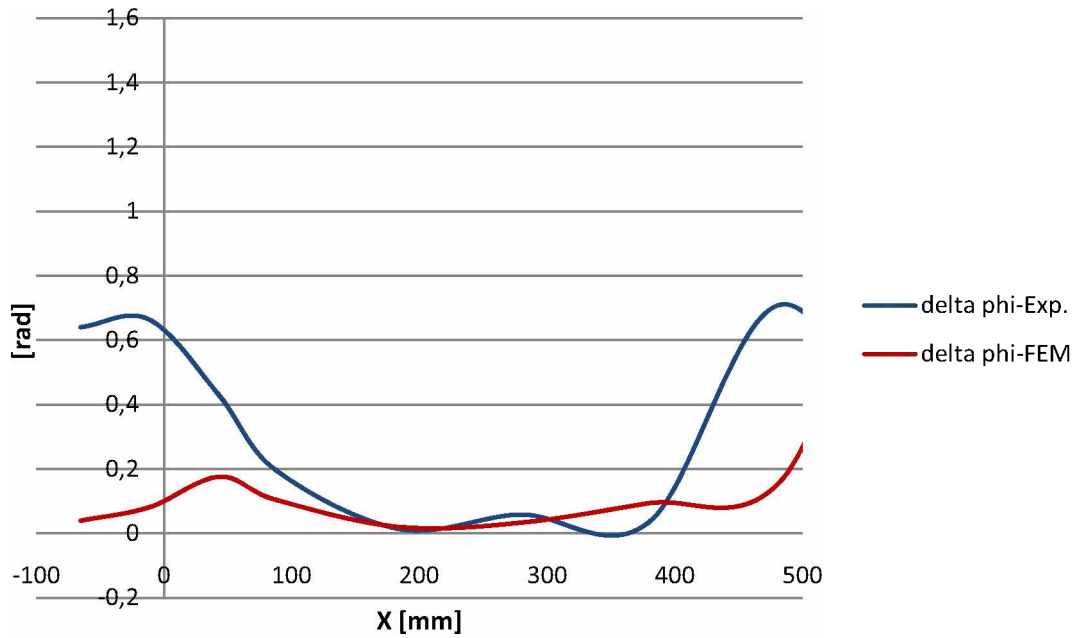


Figure A 32: Comparison of delta phi between the FEM and experiment for 2nd series, No.2-6.

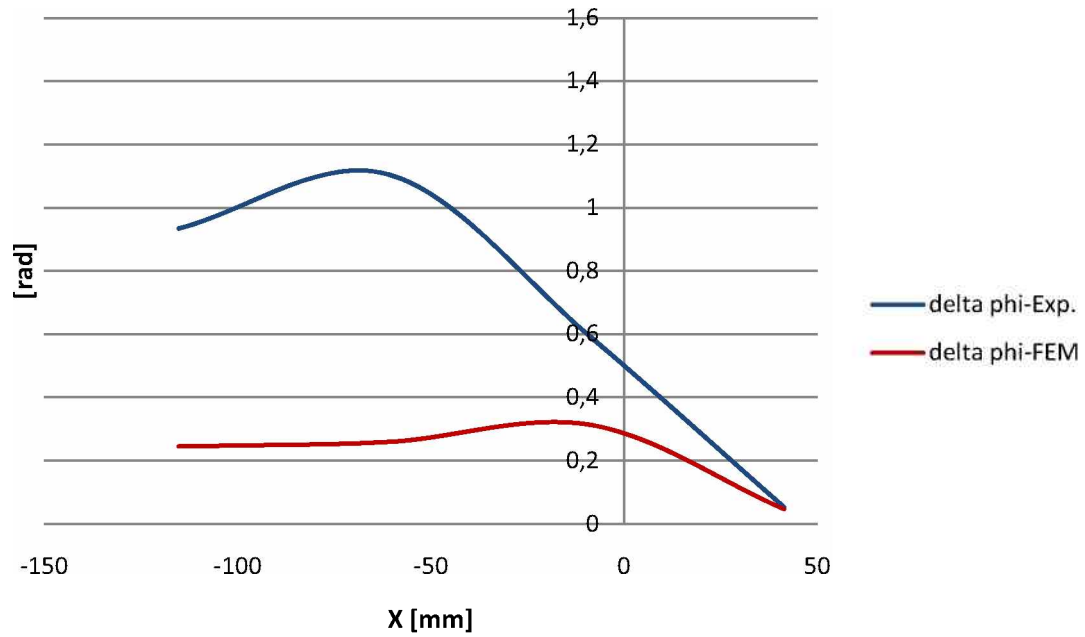


Figure A 33: Comparison of delta phi between the FEM and experiment for 3rd series, No.3-1.

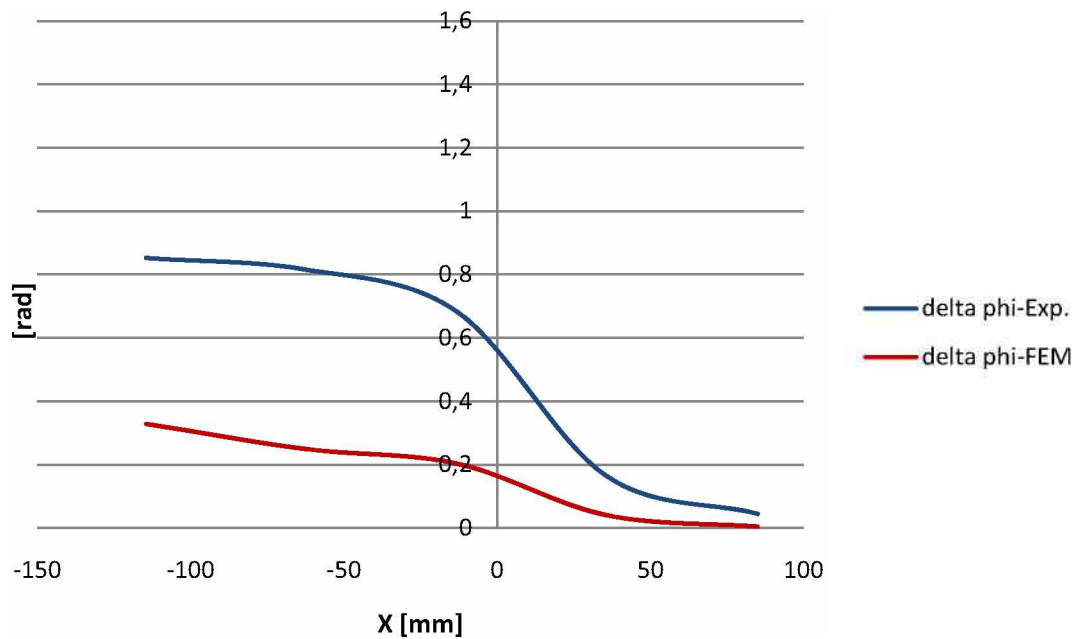


Figure A 34: : Comparison of delta phi between the FEM and experiment for 3rd series, No.3-2.

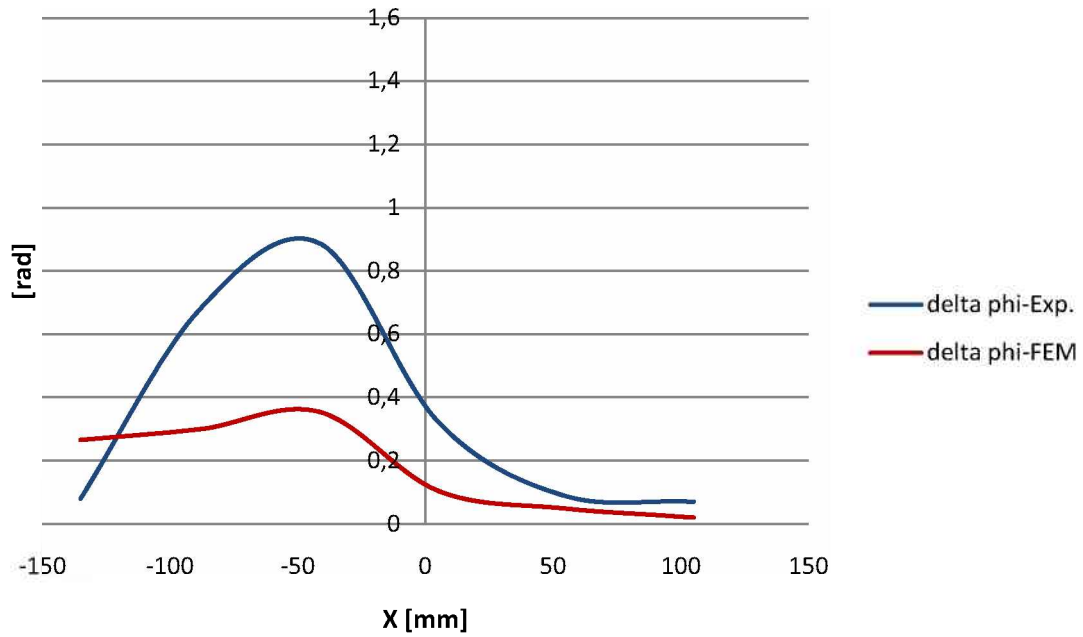


Figure A 35: : Comparison of delta phi between the FEM and experiment for 3rd series, No.3-3.

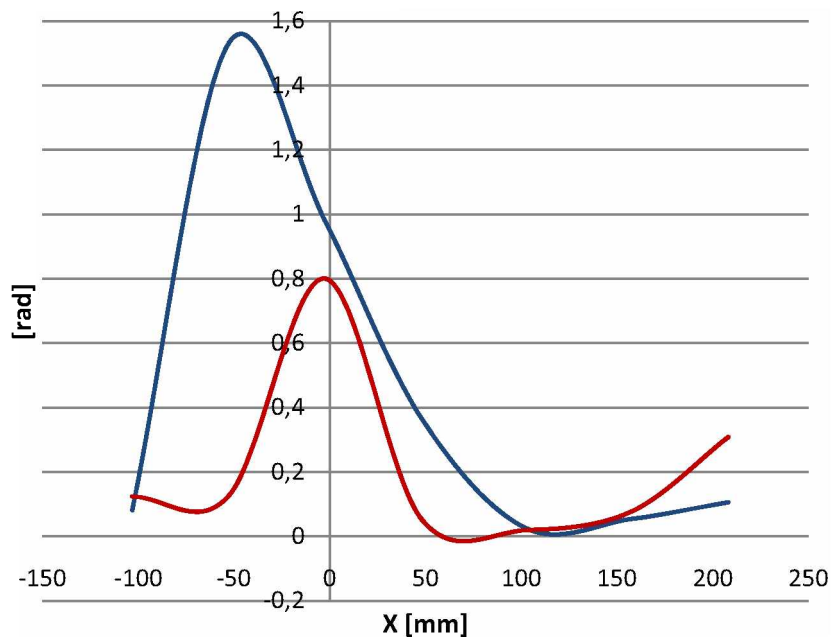


Figure A 36: : Comparison of delta phi between the FEM and experiment for 3rd series, No.3-4.

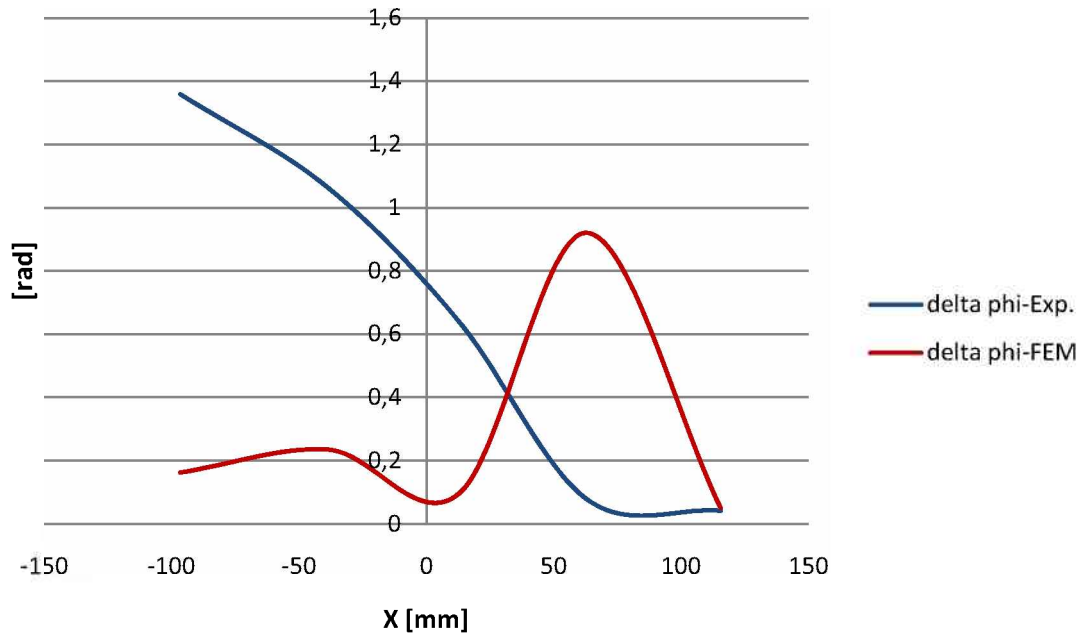


Figure A 37: : Comparison of delta phi between the FEM and experiment for 3rd series, No.3-5.

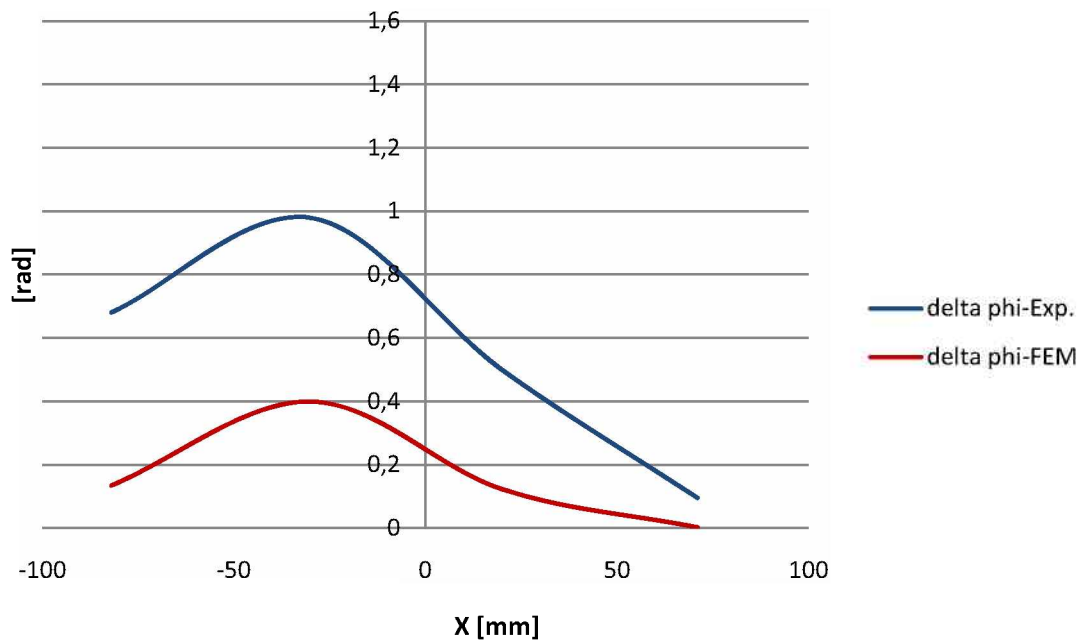


Figure A 38: : Comparison of delta phi between the FEM and experiment for 3rd series, No.3-6.

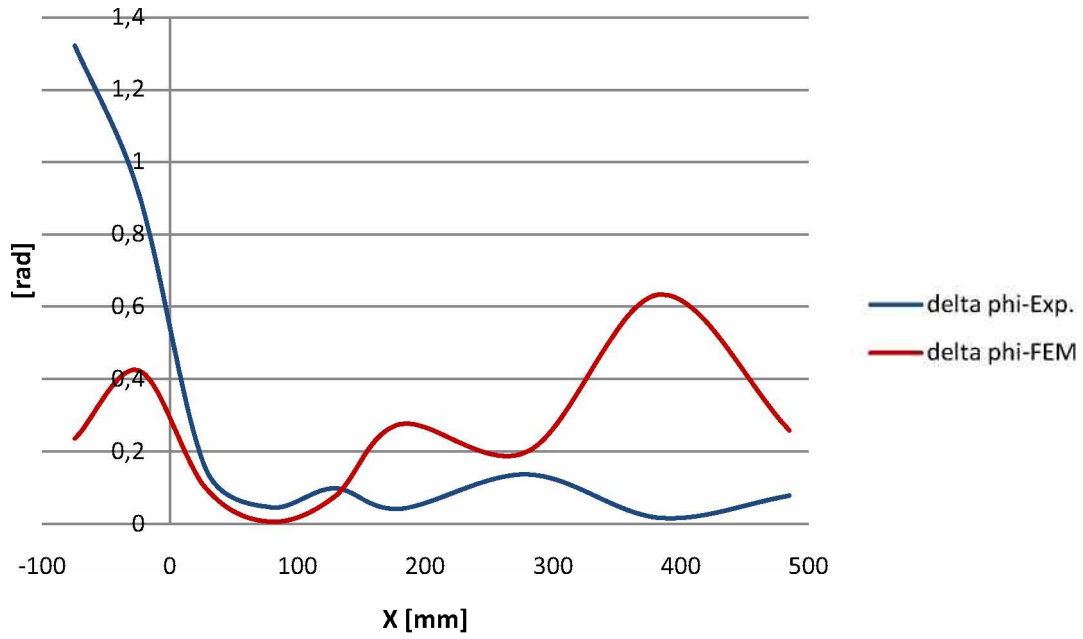


Figure A 39: : Comparison of delta phi between the FEM and experiment for 4th series, No.4-1.

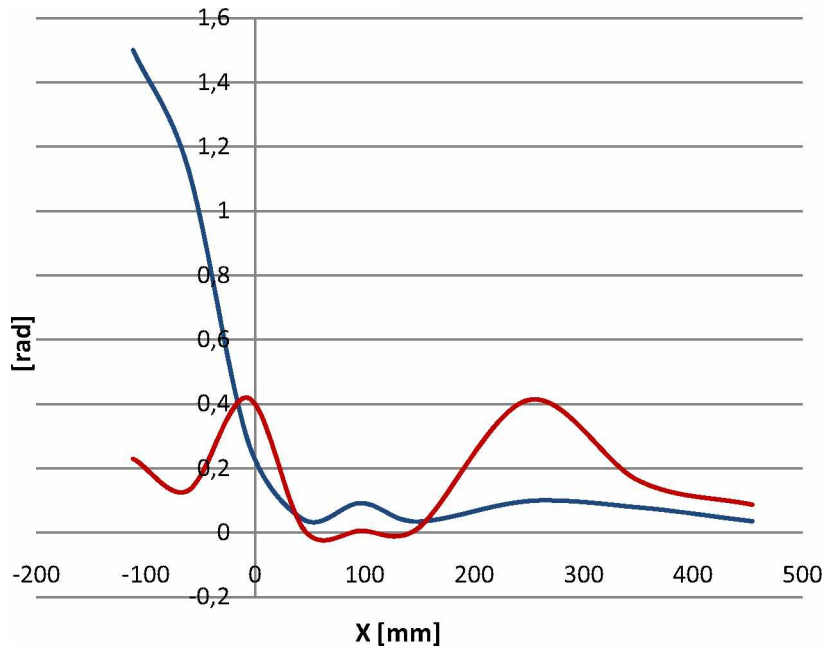


Figure A 40: : Comparison of delta phi between the FEM and experiment for 4th series, No.4-2.

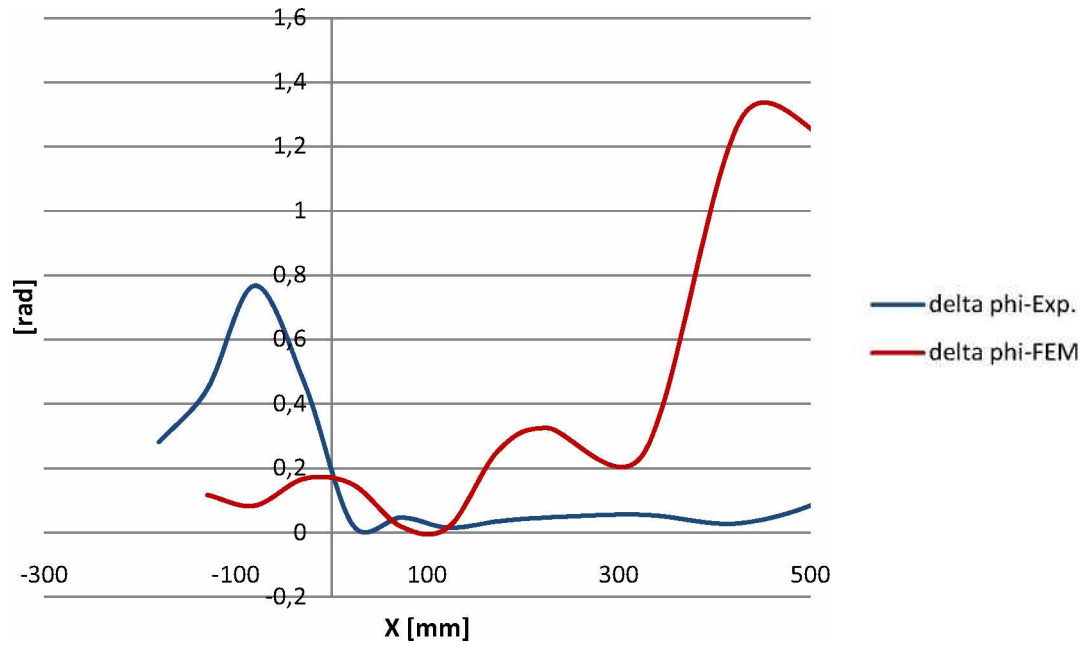


Figure A 41: Comparison of delta phi between the FEM and experiment for 4th series, No.4-3.

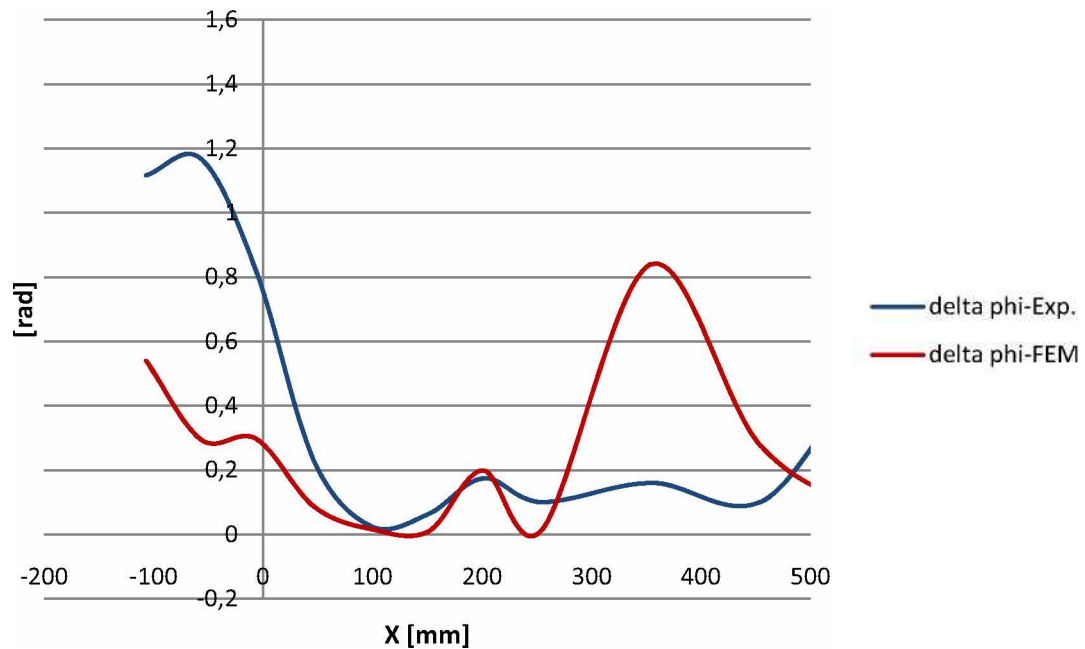


Figure A 42: Comparison of delta phi between the FEM and experiment for 4th series, No.4-4.

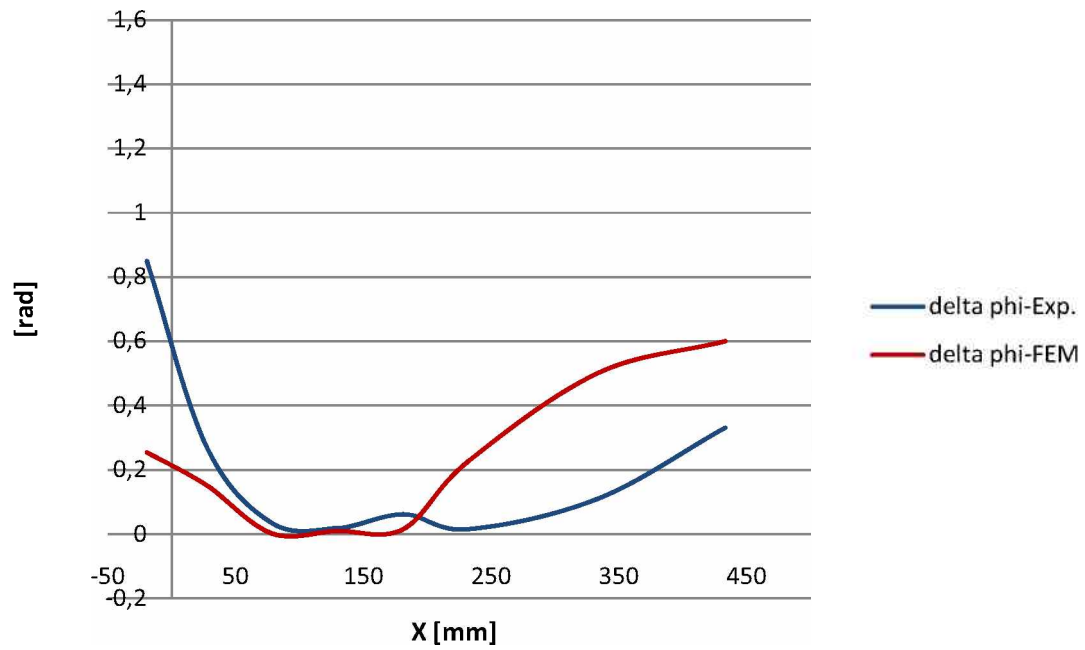


Figure A 43: Comparison of delta phi between the FEM and experiment for 4th series, No.4-5.

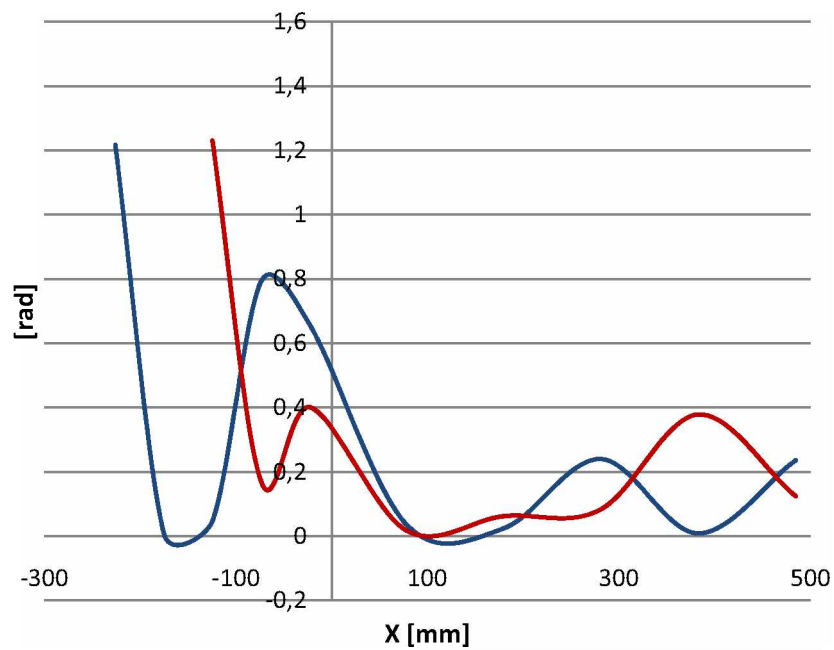


Figure A 44: Comparison of delta phi between the FEM and experiment for 4th series, No.4-6.

Table A 45: Experimental data according to the twisting for 1st series, No.1-1.

Groove's No.	I_n	w_n	Position	x	Twisting
0	0	0	-665	-692,5	0,00
1	55	45	-720	-830	0,20
2	275	35	-940	-1050	0,16
3	495	40	-1160	-1262,5	0,20
4	700	0	-1365	-1435	0,00
5	840	0	-1505	-1555	0,00
6	940	0	-1605	-802,5	0,00

Table A 46: Experimental data according to the twisting for 1st series, No.1-2.

Groove's No.	I_n	w_n	Position	x	Twisting
0	0	0	-785	-815	0,00
1	60	50	-845	-947,5	0,24
2	265	30	-1050	-1152,5	0,15
3	470	45	-1255	-1362,5	0,21
4	685	45	-1470	-1572,5	0,22
5	890	50	-1675	-1777,5	0,24
6	1095	55	-1880	-1987,5	0,26
7	1310	60	-2095	-2190	0,32
8	1500	0	-2285	-2350	0,00
9	1630	0	-2415	-1207,5	0,00

Table A 47: Experimental data according to the twisting for 1st series, No.1-3.

Groove's No.	I_n	w_n	Position	x	Twisting
0	0	0	-785	-815	0,00
1	60	50	-845	-945	0,25
2	260	40	-1045	-1155	0,18
3	480	40	-1265	-1372,5	0,19
4	695	40	-1480	-1593	0,18
5	921	50	-1706	-1805,5	0,25
6	1120	20	-1905	-1977,5	0,14
7	1265	0	-2050	-2102,5	0,00
8	1370	0	-2155	-1077,5	0,00

Table A 48: Experimental data according to the twisting for 1st series, No.1-4.

Groove's No.	I_n	w_n	Position	x	Twisting
0	0	0	-785	-810	0,00
1	50	40	-835	-930	0,21
2	240	20	-1025	-1130	0,10
3	450	30	-1235	-1335	0,15
4	650	35	-1435	-1535	0,18
5	850	25	-1635	-1740	0,12
6	1060	15	-1845	-1945	0,08
7	1260	45	-2045	-2145	0,23
8	1460	20	-2245	-2330	0,12
9	1630	0	-2415	-2465	0,00
10	1730	0	-2515	-1257,5	0,00

Table A 49: Experimental data according to the twisting for 2nd series, No.2-1.

Groove's No.	I_n	w_n	Position	x	Twisting
0	0	0	-870	-895	0,00
1	50	0	-920	-1025	0,00
2	260	60	-1130	-1245	0,26
3	490	60	-1360	-1465	0,29
4	700	75	-1570	-1680	0,34
5	920	70	-1790	-1890	0,35
6	1120	80	-1990	-2065	0,53
7	1270	0	-2140	-2185	0,00
8	1360	0	-2230	-1115	0,00

Table A 50: Experimental data according to the twisting for 2nd series, No.2-2.

Groove's No.	I_n	w_n	Position	x	Twisting
0	0	0	-870	-890	0,00
1	40	0	-910	-950	0,00
2	120	30	-990	-1055	0,23
3	250	40	-1120	-1245	0,16
4	500	60	-1370	-1475	0,29
5	710	55	-1580	-1685	0,26
6	920	80	-1790	-1900	0,36
7	1140	70	-2010	-2100	0,39
8	1320	55	-2190	-2245	0,50
9	1430	0	-2300	-2347,5	0,00
10	1525	0	-2395	-1197,5	0,00

Table A 51: Experimental data according to the twisting for 2nd series, No.2-3.

Groove's No.	I_n	w_n	Position	x	Twisting
0	0	0	-870	-910	0,00
1	80	0	-950	-1030	0,00
2	240	50	-1110	-1220	0,23
3	460	20	-1330	-1435	0,10
4	670	40	-1540	-1640	0,20
5	870	50	-1740	-1845	0,24
6	1080	50	-1950	-2050	0,25
7	1280	50	-2150	-2250	0,25
8	1480	40	-2350	-2450	0,20
9	1680	50	-2550	-2620	0,36
10	1820	20	-2690	-2735	0,22
11	1910	0	-2780	-2825	0,00
12	2000	0	-2870	-1435	0,00

Table A 52: Experimental data according to the twisting for 2nd series, No.2-4.

Groove's No.	I_n	w_n	Position	x	Twisting
0	0	0	-870	-900	0,00
1	60	0	-930	-1025	0,00
2	250	60	-1120	-1230	0,27
3	470	30	-1340	-1445	0,14
4	680	40	-1550	-1650	0,20
5	880	30	-1750	-1865	0,13
6	1110	40	-1980	-2075	0,21
7	1300	35	-2170	-2270	0,18
8	1500	40	-2370	-2470	0,20
9	1700	55	-2570	-2645	0,37
10	1850	20	-2720	-2775	0,18
11	1960	0	-2830	-2875	0,00
12	2050	0	-2920	-1460	0,00

Table A 53: Experimental data according to the twisting for 2nd series, No.2-5.

Groove's No.	I_n	w_n	Position	x	Twisting
0	0	0	-870	-895	0,00
1	50	0	-920	-1025	0,00
2	260	40	-1130	-1245	0,17
3	490	25	-1360	-1460	0,13
4	690	40	-1560	-1665	0,19
5	900	30	-1770	-1875	0,14
6	1110	30	-1980	-2085	0,14
7	1320	30	-2190	-2300	0,14
8	1540	45	-2410	-2500	0,25
9	1720	30	-2590	-2645	0,27
10	1830	0	-2700	-2755	0,00
11	1940	0	-2810	-1405	0,00

Table A 54: Experimental data according to the twisting for 3rd series, No.3-1.

Groove's No.	I_n	w_n	Position	x	Twisting
0	0	0	-810	-835	0,00
1	50	0	-860	-955	0,00
2	240	70	-1050	-1150	0,35
3	440	70	-1250	-1350	0,35
4	640	80	-1450	-1560	0,36
5	860	90	-1670	-1765	0,47
6	1050	90	-1860	-1940	0,56
7	1210	70	-2020	-2065	0,00
8	1300	0	-2110	-1055	0,00

Table A 55: Experimental data according to the twisting for 3rd series, No.3-2.

Groove's No.	I_n	w_n	Position	x	Twisting
0	0	0	-810	-835	0,00
1	50	0	-860	-955	0,00
2	240	80	-1050	-1155	0,38
3	450	90	-1260	-1355	0,47
4	640	80	-1450	-1550	0,40
5	840	70	-1650	-1747,5	0,36
6	1035	85	-1845	-1922,5	0,55
7	1190	90	-2000	-2060	0,00
8	1310	0	-2120	-1060	0,00

Table A 56: Experimental data according to the twisting for 3rd series, No.3-3.

Groove's No.	I_n	w_n	Position	x	Twisting
0	0	0	-810	-840	0,00
1	60	0	-870	-965	0,00
2	250	80	-1060	-1170	0,36
3	470	90	-1280	-1380	0,45
4	670	100	-1480	-1575	0,53
5	860	80	-1670	-1770	0,40
6	1060	90	-1870	-1960	0,50
7	1240	80	-2050	-2155	0,38
8	1450	90	-2260	-2345	0,53
9	1620	100	-2430	-2475	0,00
10	1710	0	-2520	-1260	0,00

Table A 57: Experimental data according to the twisting for 3rd series, No.3-4.

Groove's No.	I_n	w_n	Position	x	Twisting
0	0	0	-810	-837,5	0,00
1	55	0	-865	-957,5	0,00
2	240	50	-1050	-1145	0,26
3	430	70	-1240	-1332,5	0,38
4	615	60	-1425	-1527,5	0,29
5	820	75	-1630	-1720	0,42
6	1000	80	-1810	-1907,5	0,41
7	1195	80	-2005	-2082,5	0,52
8	1350	70	-2160	-2250	0,39
9	1530	80	-2340	-2400	0,67
10	1650	30	-2460	-2505	0,00
11	1740	0	-2550	-1275	0,00

Table A 58: Experimental data according to the twisting for 3rd series, No.3-5.

Groove's No.	I_n	w_n	Position	x	Twisting
0	0	0	-810	-835	0,00
1	50	0	-860	-955	0,00
2	240	70	-1050	-1140	0,39
3	420	80	-1230	-1330	0,40
4	620	90	-1430	-1530	0,45
5	820	90	-1630	-1725	0,47
6	1010	70	-1820	-1877,5	0,61
7	1125	0	-1935	-2027,5	0,00
8	1310	0	-2120	-2165	0,00
9	1400	0	-2210	-1105	0,00

Table A 59: Experimental data according to the twisting for 3rd series, No.3-6.

Groove's No.	I_n	w_n	Position	x	Twisting
0	0	0	-810	-835	0,00
1	50	0	-860	-955	0,00
2	240	80	-1050	-1145	0,42
3	430	80	-1240	-1345	0,38
4	640	70	-1450	-1550	0,35
5	840	100	-1650	-1740	0,56
6	1020	80	-1830	-1910	0,50
7	1180	30	-1990	-2020	0,00
8	1240	0	-2050	-1025	0,00

Table A 60: Experimental data according to the twisting for 4th series, No.4-1.

Groove's No.	I_n	w_n	Position	x	Twisting
0	0	0	-775	-802,5	0,00
1	55	0	-830	-922,5	0,00
2	240	50	-1015	-1115	0,25
3	440	70	-1215	-1315	0,35
4	640	70	-1415	-1510	0,37
5	830	90	-1605	-1680	0,60
6	980	0	-1755	-1805	0,00
7	1080	0	-1855	-927,5	0,00

Table A 61: Experimental data according to the twisting for 4th series, No.4-2.

Groove's No.	I_n	w_n	Position	x	Twisting
0	0	0	-775	-800	0,00
1	50	0	-825	-920	0,00
2	240	40	-1015	-1120	0,19
3	450	70	-1225	-1325	0,35
4	650	90	-1425	-1520	0,47
5	840	70	-1615	-1715	0,35
6	1040	60	-1815	-1925	0,27
7	1260	100	-2035	-2140	0,48
8	1470	80	-2245	-2320	0,53
9	1620	0	-2395	-2410	0,00
10	1650	0	-2425	-1212,5	0,00

Table A 62: Experimental data according to the twisting for 4th series, No.4-3.

Groove's No.	I_n	w_n	Position	x	Twisting
0	0	0	-775	-800	0,00
1	50	0	-825	-922,5	0,00
2	245	50	-1020	-1127,5	0,23
3	460	75	-1235	-1340	0,36
4	670	95	-1445	-1530	0,56
5	840	70	-1615	-1680	0,54
6	970	0	-1745	-1790	0,00
7	1060	0	-1835	-917,5	0,00

Table A 63: Experimental data according to the twisting for 4th series, No.4-4.

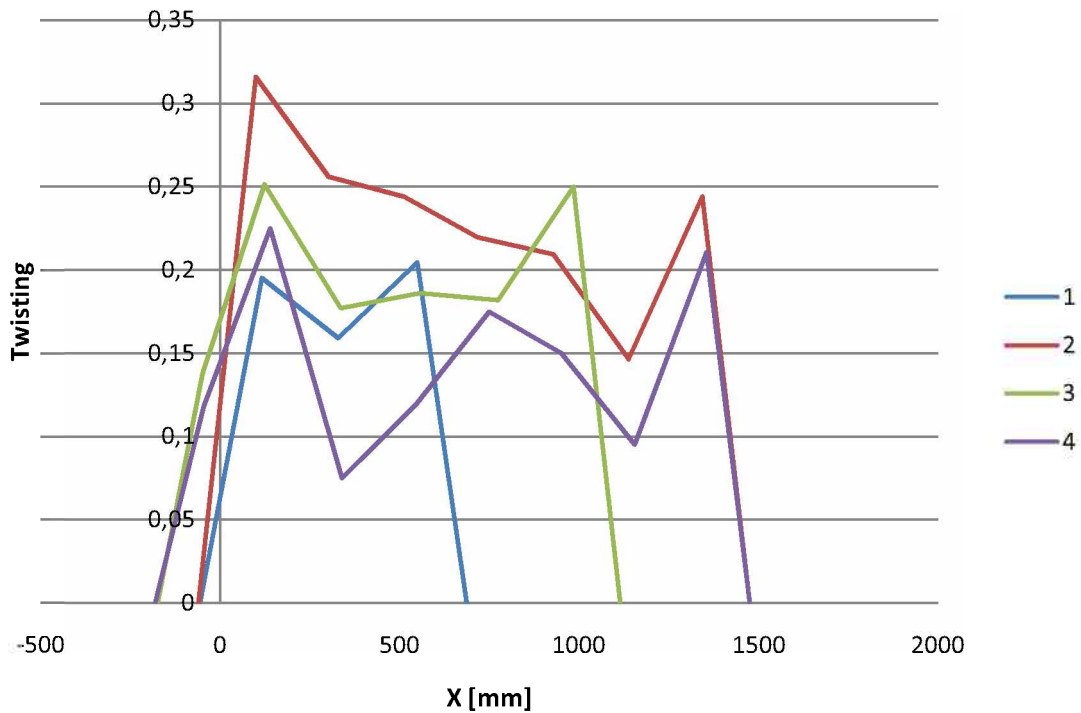
Groove's No.	I_n	w_n	Position	x	Twisting
0	0	0	-775	-800	0,00
1	50	0	-825	-920	0,00
2	240	50	-1015	-1110	0,26
3	430	50	-1205	-1300	0,26
4	620	80	-1395	-1490	0,42
5	810	70	-1585	-1680	0,37
6	1000	80	-1775	-1875	0,40
7	1200	70	-1975	-2070	0,37
8	1390	80	-2165	-2235	0,57
9	1530	0	-2305	-2325	0,00
10	1570	0	-2345	-1172,5	0,00

Table A 64: Experimental data according to the twisting for 4th series, No.4-5.

Groove's No.	I_n	w_n	Position	x	Twisting
0	0	0	-775	-800	0,00
1	50	0	-825	-915	0,00
2	230	50	-1005	-1100	0,26
3	420	70	-1195	-1297,5	0,34
4	625	60	-1400	-1497,5	0,31
5	820	80	-1595	-1695	0,40
6	1020	70	-1795	-1885	0,39
7	1200	75	-1975	-2045	0,54
8	1340	0	-2115	-2160	0,00
9	1430	0	-2205	-1102,5	0,00

Table A 65: Experimental data according to the twisting for 4th series, No.4-6.

Groove's No.	I_n	w_n	Position	x	Twisting
0	0	0	-775	-800	0,00
1	50	0	-825	-925	0,00
2	250	70	-1025	-1125	0,35
3	450	60	-1225	-1320	0,32
4	640	80	-1415	-1515	0,40
5	840	80	-1615	-1710	0,42
6	1030	80	-1805	-1895	0,44
7	1210	70	-1985	-2045	0,58
8	1330	0	-2105	-2150	0,00
9	1420	0	-2195	-1097,5	0,00

Figure A 45: Twisting along the rolling direction based on the experiment for 1st series.

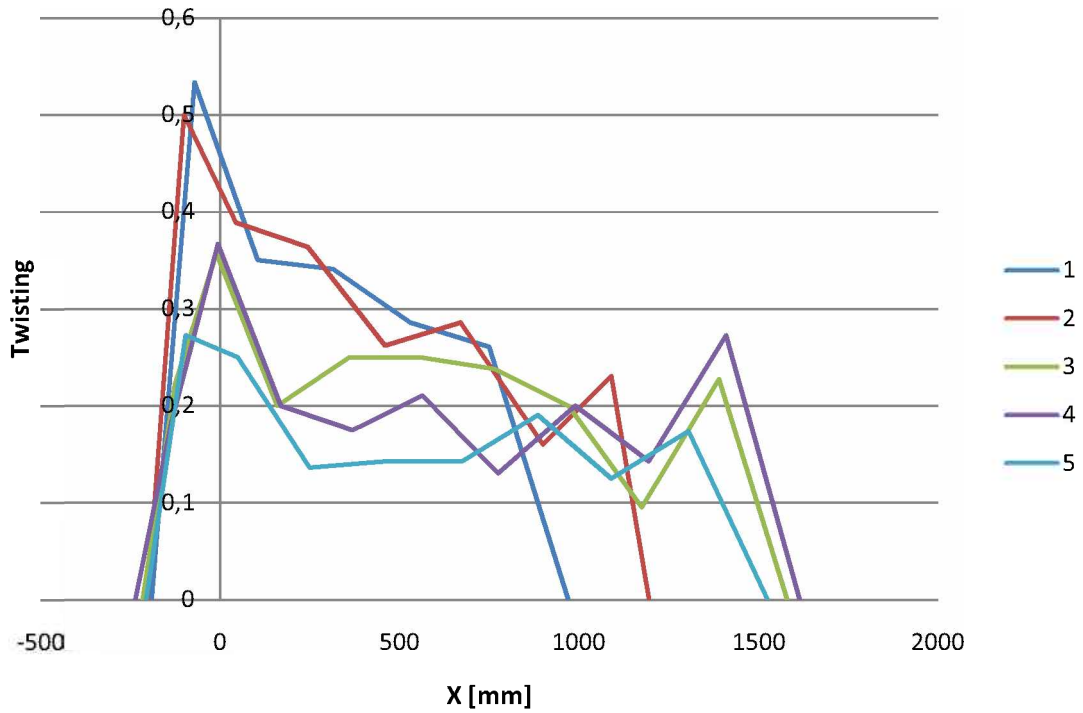


Figure A 46: Twisting along the rolling direction based on the experiment for 2nd series.

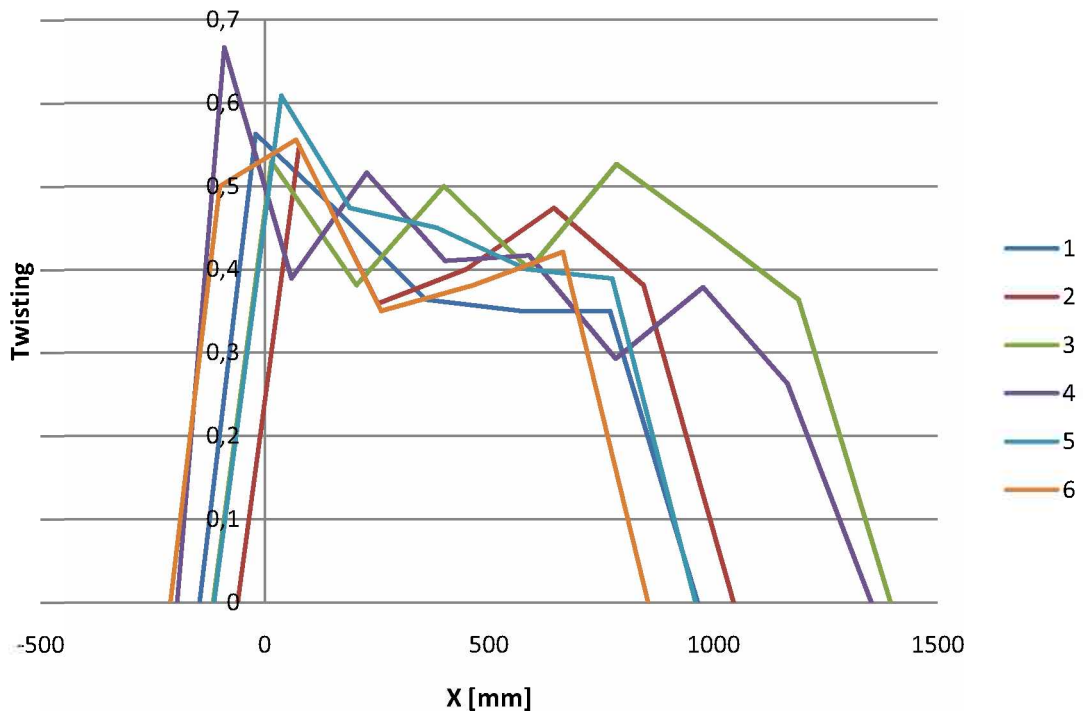


Figure A 47: Twisting along the rolling direction based on the experiment for 3rd series.

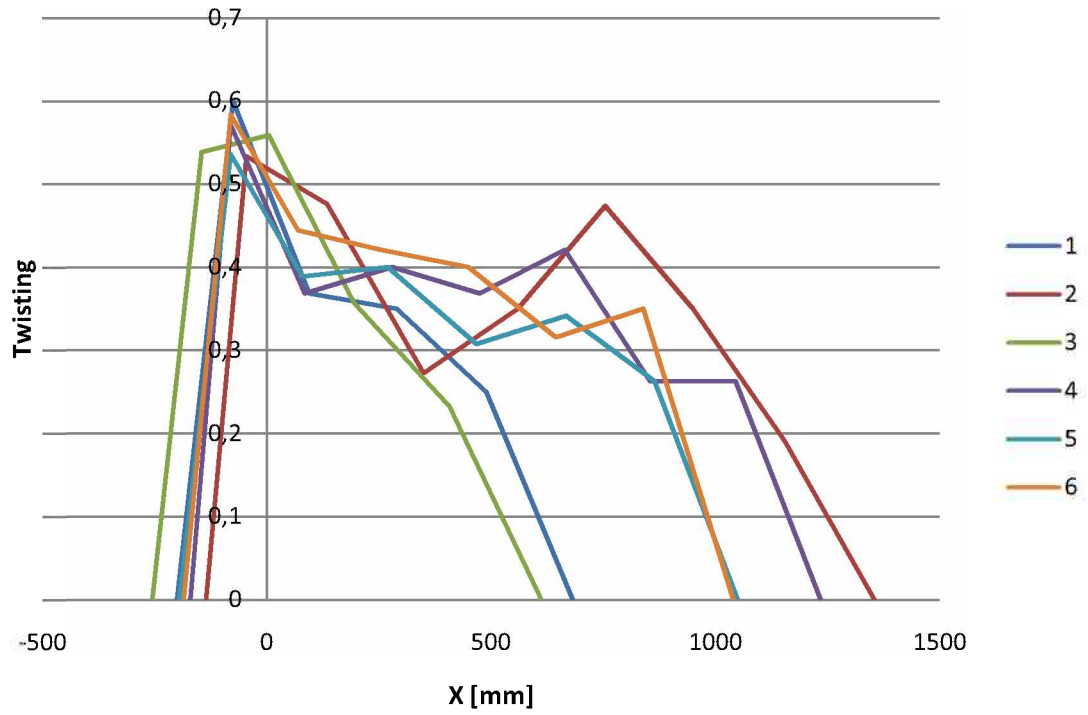


Figure A 48: Twisting along the rolling direction based on the experiment for 4th series.